UTRECHT UNIVERSITY

MASTER THESIS

Testing general relativity with gravitational wave parameter estimation using machine learning

Image generated by DALL-E3

Author:
Jurriaan Langendorff[1]

Supervisors:
Prof. Dr. Chris Van Den Broeck[1,3]
Dr. Justin Janquart[1,3], Mr. Alex Kolmus[2]

A thesis submitted in fulfillment of the requirements for the degree of Experimental Physics

in the

Institute for Gravitational and Subatomic Physics (GRASP)
Graduate School of Natural Sciences (GSNS)

June 28, 2024

1. *Department of Physics, Institute for Gravitational and Subatomic Physics (GRASP), Utrecht University, Princetonplein 1, NL-3584 CC Utrecht, The Netherlands*

2. *Institute for Computing and Information Sciences, Radboud University Nijmegen*

3. *Nikhef - National Institute for Subatomic Physics, Science Park, NL-1098 XG Amsterdam, The Netherlands*

Universiteit Utrecht

In the beginning:
there was no up
there was no down
there was no side to side

there was no light
there was no dark
nor shape of any kind

there were no stars or planet Mars or protons to collide
there was no up
there was no down
there was no side to side

and furthermore to underscore this total lacking state
there was no here
there was no there
because there was no space

and in this endless void which can't be thought of as a place
there was no time
and so no passing minutes, hours, days

of all the paradoxes that belabor common sense
I think this one's the greatest
this time before events

because how did we go from nothing
to infinitely dense?
from immeasurably small
to inconceivably immense?

but before we get unmoored from the question at the start
let's take a breath and marvel
at when math becomes an art

because against this cosmic canvas
one hears the dance of gravitational waves
testing our understanding
with ripples traversing through this space

and with that final statement, it's time for me to write
because also every thesis starts with
no up
no down
nor side to side

- Hank Green, Reina del Cid, Jurriaan Langendorff

UTRECHT UNIVERSITY

Abstract

Experimental Physics
Graduate School of Natural Sciences (GSNS)

Experimental Physics

Testing general relativity with gravitational wave parameter estimation using machine learning

by Jurriaan Langendorff[1]

The ability to detect gravitational waves from coalescing binary black holes has opened up the possibility of testing general relativity in its most extreme regime of highly dynamical, strong spacetime curvature. Model-independent methods to do this exist, which allow for deviations from the predictions of general relativity by introducing testing parameters at selected places in the mathematical expression for the waveform, and these are routinely applied to signals from binary black holes. However, their computational requirements do not scale well with the increased number of detections expected when considering the upgrades of the LIGO and Virgo interferometers. Furthermore, the addition of these testing parameters will increase the parameter space needed to explore, thus asking for more computational resources. Therefore, a faster but equally robust method is urgently needed.

In this research, we present a simulation-based technique to speed up these measurements. To begin with, we consider individual binary black hole signals and apply a normalizing flow neural network for fast measurements of all parameters. The testing parameters studied in the thesis relate to the modified dispersion relation in the propagation of gravitational waves. We show that our presented model is a reliable method to infer the probability distributions for the testing parameters.

Acknowledgements

The journey I embarked on while working on this research project over the past year was truly special. The experiences I had have been invaluable, providing me not only with extensive knowledge about machine learning and gravitational waves, but also with the skills to conduct research, including reading, discussing, and writing. Despite my dyslexia posing a challenge for me, the generous assistance I received has significantly improved my proficiency in the language of research.

Foremost, I would like to express my gratitude to Chris Van Den Broeck for allowing me to not only do my bachelor's thesis here but also for providing me with the opportunity to work on this project. Our group meetings were truly enjoyable and provided insightful advice and knowledge. I am also grateful for the inclusion in other scientific discussions and the opportunity to present at the Dutch Machine Learning for Gravitational Waves Meeting.

Next, I would like to extend special thanks to Justin Janquart and Alex Kolmus. Your guidance throughout this thesis has been outstanding. The knowledge I have gained from you is invaluable, making you truly remarkable supervisors.

A big shout-out to Wouter van Straalen is also in order. Having someone to brainstorm with over the challenges we faced during this master thesis was incredibly helpful. Working together on building these frameworks was truly the best experience I had this year, and I'm going to miss every moment of it when this master is over.

I would also like to thank all the amazing friends who helped to keep me sane over the last year. From all our lunch break conversations to the workout encouragements, I'm incredibly grateful to have had places to share this experience.

Finally, I would like to thank the LIGO-Virgo-KAGRA collaboration for providing the computational resources that were instrumental in this project. Your support has been invaluable.

Contents

List of Abbreviations

GW(s)	**G**ravitational **W**ave(s)	**CBC**	**C**ompact-**B**inary **C**oalescence
BBH	**B**inary **B**lack **H**ole	**BNS**	**B**inary **N**eutran **S**tar
GRB	**G**amma-**R**ay **B**urst		
PE	**P**arameter **E**stimation	**NR**	**N**umerical **R**elativity
PN	**P**ost **N**ewtonian	**BHP**	**B**lack **H**ole **P**ertubation
ASD	**A**mplitude **S**pectral **D**ensity	**PSD**	**P**ower **S**pectral **D**ensity
SNR	**S**ignal to **N**oise **R**atio		
GR	**G**eneral **R**elativity	**MDR**	**M**odified **D**ispersion **R**elation
FLRW	**F**riedmann **L**emaître **R**obertson **W**alker	**WKB**	**W**entzel **K**ramers **B**rillouin
SPA	**S**tationary **P**hase **A**pproximation	**LIV**	**L**orentz **I**nvariance **V**iolation
ML	**M**achine **L**earning	**NN**	**N**eural **N**etwork
NF	**N**ormalizing **F**low	**ResNet**	**R**esidual **N**etwork
SVD	**S**ingular **V**alue **D**ecomposition	**NPE**	**N**eural **P**osterior **E**stimation

Physical Constants and Units

Gravitational constant	$G = 6.6743 \times 10^{-11}\,\mathrm{m}^3/\mathrm{kg}/\mathrm{s}$
Speed of Light	$c = 2.997\,924\,58 \times 10^{8}\,\mathrm{m\,s}^{-1}$
Planck constant	$h = 6.626\,070\,15 \times 10^{-34}\,\mathrm{J\,s}$ ($\approx 4.135667696 \times 10^{-3}$ peV)
Electronvolt	$eV = 1.602 \times 10^{-19}\,\mathrm{J}$
Light-year	$ly = 9.46 \times 10^{15}\,\mathrm{m}$
Parsec	$Pc = 3.085\,677\,58 \times 10^{16}\,\mathrm{m}$ ($\approx 3.261631 ly$)
Astronomical unit	$AU = 14.96 \times 10^{10}\,\mathrm{m}$ ($\approx 15.86 \times 10^{-6} ly$)
Solar mass	$M_\odot = 1.988\,409\,870\,698\,050\,7 \times 10^{30}\,\mathrm{kg}$

Important note: *In the theoretical derivations, it is conventional to use Planck units, e.i., $G = 1$, $c = 1$, $\hbar = \frac{h}{2\pi} = 1$ (and $k_B = 1$). This is often done in the literature. In this thesis, we will try to avoid this notation where possible.*

length	$\sqrt{\hbar G/c^3} = 1.616 \times 10^{-35}\,\mathrm{m}$
mass	$\sqrt{\hbar c/G} = 2.176 \times 10^{-8}\,\mathrm{kg}$
time	$\sqrt{\hbar G/c^5} = 5.391 \times 10^{-44}\,\mathrm{s}$
energy	$\sqrt{\hbar c^5/G{k_B}^2} = 1.417 \times 10^{32}\,\mathrm{K}$

Note on scale: *In this thesis, we study physics on cosmological scales. Therefore the relevant units convenient for use are length in Megaparsec(Mpc), Mass in solar mass($M_\odot$), time in seconds(s), and energy in pico-electronVolt(peV).*

Introduction

After more than 100 years of rigorous testing, Einstein's theory of General Relativity (GR) [1] still stands as one of our best descriptions of gravitational phenomena on a large range of scales. Over the past century, there have been countless tests looking for deviations in GR, which it passed with flying colors. Two phenomena that helped solidify the theory were the precession of the perihelion of Mercury [2] and the gravitational deflection of light [3]. Where Newton's theory of gravity failed to explain these experimentally observed phenomena, GR was able to make accurate predictions.

Nowadays, many other probes test GR in different regimes [3]. The vast majority, however, probes the non-radiative, weak field dynamics of gravity. While Gravitational Waves (GWs) test GR in its most extreme regime of highly dynamical, strong spacetime curvature. As early as 1916, Einstein calculated the first description of GWs [4]. The first indirect measurement came by Hulse-Taylor, who observed variations in the orbital period of a binary pulsar. Due to the incredibly strong gravitational fields in these types of binary systems, orbital energy was radiating away in the form of GWs [5].

It took almost a century before technology improved enough to make direct detection. On the 14th of September 2015, the first GW was detected (GW150914) [6], a major breakthrough in the field. The source, two black holes spiraling towards each other before merging, radiated about three suns worth of energy in less than a second. Since then, more than a hundred of these events have been detected [7].

These events are called Compact Binary Coalescence (CBC) and can also happen with neutron stars. The first of which, GW170817 [8], started a new era of multi-messenger astronomy because the GW was accompanied by the electromagnetic emission of the merger [9]. With this observation, we can put constraints on the difference in the propagation speed of GWs and that of light, limiting their relative difference to the order of only 10^{-15}, putting strong constraints on alternative theories of gravity.

Methods to test for deviations from the predictions of GR with GWs exist. Some of them introduce testing parameters at selected places in the mathematical expression for the waveform [10]. However, their computational requirements do not scale well with the increasing number of GW detections that can be expected because of significant instrumental upgrades. Therefore, a faster but equally robust method is needed.

To enhance efficiency in these tests, we explore the fast-growing area of research of Machine Learning (ML) [11, 12]. ML promises a desired speedup over current methods, whilst maintaining similar precision. In this research, we present a simulation-based technique to speed up these measurements. We study individual binary black hole signals and apply a normalizing flow neural network [13] for measurements of all parameters, including testing parameters. The test considered in this research studies the propagation of GW with a Modified Dispersion Relation (MDR) [14]. We show that our ML approach is a promising avenue to explore for the inference of these testing parameters.

Part I

Gravitational Waves

Chapter 1

General Relativity for Gravitational Waves

1.1 Essential elements of General Relativity

To start understanding GWs on a fundamental level, one needs to familiarize oneself with our best theoretical description of gravity, GR. First, let us ask the question, what is wrong with Newtonian gravity? Consider a gravitational potential $\Phi(\vec{x},t)$, generated by mass density $\rho(\vec{x},t)$. A particle in this potential needs to satisfy the Poisson equation (which is solved via Green's function)

$$\nabla^2\Phi = 4\pi G\rho \qquad \Rightarrow \qquad \Phi(\vec{x},t) = -G\int dV' \frac{\rho(\vec{x}',t)}{|\vec{x}-\vec{x}'|}, \tag{1.1}$$

where the integral is over spatial volume V span by mass density ρ in coordinate system $\vec{x}'$. The problem that arises is that a change in $\rho(\vec{x},t)$ instantaneously changes $\Phi(\vec{x},t)$ throughout all space. The instantaneous action of gravity gives rise to an action at a distance. Newton knew this was wrong and called it "*so great an absurdity that I believe no man who has in philosophical matters a competent faculty of thinking can ever fall into it*" [15]. Still, he was unable to solve this problem.

An analogous problem arises in electrostatic. Consider a charged particle in an electric potential $\Phi(\vec{x},t)$, generated by charge density $\rho(\vec{x},t)$. Analogously, the equations linking potential and density are

$$\nabla^2\Phi = -\frac{\rho}{\epsilon_0} \qquad \Rightarrow \qquad \Phi(\vec{x},t) = \frac{1}{4\pi\epsilon_0}\int dV' \frac{\rho(\vec{x}',t)}{|\vec{x}-\vec{x}'|}, \tag{1.2}$$

which gave the same problem, instantaneous action at a distance. The solution to this problem were Maxwell's equations

$$\partial_\nu F^{\mu\nu} = J^\mu \qquad \text{with} \qquad F_{\mu\nu} = \partial_\mu A_\nu - \partial_\nu A_\mu. \tag{1.3}$$

By combining electro and magnetic potentials $A^\mu = (\Phi, \vec{A})$ and charge dynamics $J^\mu = (\rho, \vec{J})$ into one formalism, one could describe the dynamical nature of electromagnetism. With this, the change in action now propagates at the speed of light. Einstein's challenge was to find the equivalency of Maxwell's equations for gravity.

Einstein solved this problem by stating his *equivalence principle* which builds on the following three principles:

1. Gravity is universal: inertial mass equals gravitational mass and thus local acceleration is equivalent to local gravitational acceleration.

2. A uniform gravitational field is indistinguishable from uniform acceleration.

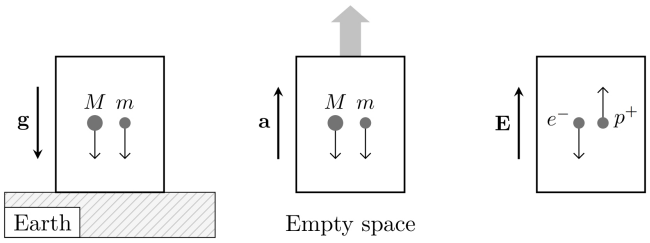

FIGURE 1.1: Illustration showing the likeness of uniform gravitational field (left), uniform acceleration (middle), and an electric field (right). Image from [16].

3. In a small region of spacetime, the laws of physics are reduced to those of special relativity.

For an illustration of the equivalence principle, see figure 1.1. Note that (gravitational) acceleration acts differently than an electric field, in which direction is dictated by opposite charges.

In this chapter, we will use these principles to define the necessary equations from GR needed for understanding derivations made in this thesis.

1.1.1 Gravity as Curved Spacetime

In GR, space and time are linked, i.e. they are described as a 4-dimensional manifold[1], called spacetime. As we know from special relativity, spacetime geometry is defined by an invariant length element

$$ds^2 = -(cdt)^2 + dx^i dx^i = \eta_{\mu\nu} dx^\mu dx^\nu, \tag{1.4}$$

where we use Einstein's summation convention. This is the so-called Minkowski metric of flat spacetime, described by the metric tensor $\eta_{\mu\nu}$. In GR we generalize the notion of a metric as g, describing the line element

$$ds^2 = g_{\mu\nu} dx^\mu dx^\nu. \tag{1.5}$$

The metric tensor $g_{\mu\nu}$ encodes the connection between different spacetime coordinates, for example, it defines fundamental notions like distance, angles, and the arrow of time. In this way, the metric tensor tells how spacetime geometry is curved.

1.1.2 Spacetime Curvature and Geodesics

Before we can answer how spacetime is curved by gravity, we have to learn how to take the derivative of a vector on a curved manifold. The problem with taking the partial derivative of a vector like $\partial_\alpha T^\mu$ is that it does not transform the same under coordinate transformations. The solution is to define the *covariant derivative*,

$$\nabla_\alpha T^\mu = \partial_\alpha T^\mu + \Gamma^\mu_{\alpha\beta} T^\alpha, \tag{1.6}$$

where $\Gamma^\mu_{\alpha\beta}$ are the *Christoffel symbols*

$$\Gamma^\mu_{\alpha\beta} \equiv \frac{1}{2} g^{\mu\rho} (\partial_\alpha g_{\beta\rho} + \partial_\beta g_{\alpha\rho} - \partial_\rho g_{\alpha\beta}). \tag{1.7}$$

[1] A manifold is a space for which every point can be mapped Euclidean space. I recommend [17] and [16] as a guide through the mathematical details.

This covariant derivative conserves the transformation rules[2].

A geodesic is the path taken by an observer in freefall. This is obtained by finding the curve for which the action, $S = -m \int d\tau$, is an extremum, i.e. solving the Euler-Lagrange equation resulting in

$$\frac{d^2x^\mu}{d\tau^2} + \Gamma^\mu_{\alpha\beta}\frac{dx^\alpha}{d\tau}\frac{dx^\beta}{d\tau} = 0, \tag{1.8}$$

the *geodesic equation*, where τ defines *proper time* ($d\tau^2 = -ds^2 = -g^{\mu\nu}dx_\mu dx_\nu$). Observe that the geodesic equation looks similar to the covariant derivative. The link between the two is the concept of parallel transport.

Parallel transport involves moving a vector V^μ along a curve $x^\mu(\lambda)$ while keeping its orientation the same with respect to the tangent vector of a curve

$$\frac{dx^\nu}{d\lambda}\nabla_\nu V^\mu = 0. \tag{1.9}$$

Using parallel transport, we can give an alternative definition of a geodesic as the curve along which the tangent vector $dx^\mu/d\lambda$ itself is parallel transported, such that

$$\frac{dx^\nu}{d\lambda}\nabla_\nu\frac{dx^\mu}{d\lambda} = 0 \qquad \Rightarrow \qquad \frac{d^2x^\mu}{d\lambda^2} + \Gamma^\mu_{\alpha\beta}\frac{dx^\alpha}{d\lambda}\frac{dx^\beta}{d\lambda} = 0. \tag{1.10}$$

An important effect of parallel transporting a vector on a curved geometry is that the direction of the transported vector is dependent on the path. One way of seeing this is that the covariant derivative does not commute:

$$[\nabla_\mu, \nabla_\nu]V^\sigma = R^\sigma_{\rho\mu\nu}V^\rho, \tag{1.11}$$

where $R^\sigma_{\rho\mu\nu}$ is the Riemann tensor and measures the discrepancy of the second covariant derivatives to commute. Equation 1.11 is called the Ricci identity, where it is useful to define the contraction of the Riemann tensor

$$R^\rho_{\mu\rho\nu} \equiv R_{\mu\nu} = \partial_\rho\Gamma^\rho_{\mu\nu} - \partial_\nu\Gamma^\rho_{\mu\rho} + \Gamma^\sigma_{\sigma\rho}\Gamma^\rho_{\mu\nu} - \Gamma^\rho_{\mu\sigma}\Gamma^\sigma_{\nu\rho}, \tag{1.12}$$

where $R_{\mu\nu}$ is the Ricci tensor. The trace of the Ricci tensor is the Ricci scalar

$$R \equiv R^\mu{}_\mu = g^{\mu\nu}R_{\mu\nu}, \tag{1.13}$$

which is an important measure of the local curvature of spacetime. To each point on a manifold, the Ricci scalar assigns a single real number determined by the geometry of the metric near that point.

1.1.3 Einstein's Field Equations

Recall the Poisson equation for a Newtonian gravitational potential (equation 1.1). Notice that $\nabla^2 = \partial^i\partial_i$ is the trace of a second derivative. This is similar to the second covariant derivative encapsulated by the Riemann tensor, and taking the trace results in the Ricci tensor. Thus, a valid guess for a relativistic version of the Poison equation is

$$R_{00} = \kappa\rho, \tag{1.14}$$

[2]To make this less abstract, remember the analog of electrodynamics where we defined derivative $D_\mu = \partial_\mu + iA_\mu$, where iA_μ serves a similar purpose as $\Gamma^\mu_{\alpha\beta}$ in GR.

where κ is a constant relating curvature to mass density. This is almost the right equation, or better yet, the set of equations if we extend the indices to include the spatial components. It turns out not to conserve energy, thus a different formulation is needed.

An alternative description of curvature is the *Einstein tensor*,

$$G_{\mu\nu} \equiv R_{\mu\nu} - \frac{1}{2} g_{\mu\nu} R. \tag{1.15}$$

This turns out to be the tensor describing the link between matter and spacetime curvature, resulting in the *Einstein field equations*:

$$G_{\mu\nu} = \frac{8\pi G}{c^4} T_{\mu\nu}, \tag{1.16}$$

where $T_{\mu\nu}$ is *the energy-momentum tensor*, which encodes the source of the gravitational field:

$$T_{\mu\nu} = \left(\begin{array}{c|c} T_{00} & T_{0j} \\ \hline T_{i0} & T_{ij} \end{array}\right) = \left(\begin{array}{c|c} \text{density of energy } (\rho c^2) & \text{density of momentum} \\ \hline \text{flow of energy (flux)} & \text{flow of momentum (stress)} \end{array}\right). \tag{1.17}$$

This is how GR describes gravity, or to quote John Wheeler; "*Spacetime tells matter how to move; matter tells spacetime how to curve*".

There is one other term that could be added to the left-hand side of equation 1.16, which is consistent with the local conservation of $T_{\mu\nu}$, namely a term of the form $\Lambda g_{\mu\nu}$, resulting in

$$G_{\mu\nu} + \Lambda g_{\mu\nu} = \frac{8\pi G}{c^4} T_{\mu\nu}, \tag{1.18}$$

where Λ is the *cosmological constant*, which describes the accelerated expansion of the universe. For the purpose of GWs, we will first consider a static universe as described by equation 1.16.

1.2 Analytical derivations of Gravitational Waves

Remember from electromagnetism that the Maxwell equations (1.3) allow for electromagnetic wave solutions. Similarly, the Einstein equations (1.16) admit for propagating waves, i.e. GWs. In this section, we derive an analytical formalism for the description of GWs.

1.2.1 Linearized General Relativity

Even if there seem to be numerous stars in the night sky, space is mostly empty [18], thus spacetime can be considered flat. GWs are small ripples in this spacetime, as we will see. Therefore, we can describe them by a small perturbation around Minkowski space:

$$g_{\mu\nu} = \eta_{\mu\nu} + h_{\mu\nu} \qquad \text{with} \qquad |h_{\mu\nu}| \ll 1. \tag{1.19}$$

This is called the *weak-field approximation*. The perturbation $h_{\mu\nu}$ is considered to be small, thus we will only look at leading order terms. Doing the math gives us the linearized Einstein tensor

$$G_{\mu\nu} = \frac{1}{2}\left[\partial^\rho \partial_\mu h_{\nu\rho} + \partial^\rho \partial_\nu h_{\mu\rho} - \Box h_{\mu\nu} - \partial_\mu \partial_\nu h - (\partial^\rho \partial^\sigma h_{\rho\sigma} - \Box h)\eta_{\mu\nu}\right], \tag{1.20}$$

where we use the d'Alembertian operator $\Box = \partial^\mu \partial_\mu$ and $h \equiv h^\mu{}_\mu$. This expression of the Einstein tensor can be further simplified by considering the following analogy.

In electromagnetism, it is useful to use the so-called *Lorenz gauge*, $\partial^\mu A_\mu = 0$, to reduce the Maxwell equations 1.3 to a wave equation:

$$\Box A_\mu = J_\mu. \tag{1.21}$$

We are looking for an analog in linearized gravity. One such condition is $\Gamma^\rho_{\mu\nu} g^{\mu\nu} = 0$, the *de Donder gauge* [17]. Using this gauge, the Einstein tensor greatly simplifies, reducing the Einstein field equations 1.16 to

$$\Box h_{\mu\nu} - \frac{1}{2}\Box h \eta_{\mu\nu} = -\frac{16\pi G}{c^4} T_{\mu\nu}. \tag{1.22}$$

This can be reduced further by defining the *trace-reversed* perturbation $\bar{h}_{\mu\nu} = h_{\mu\nu} - \frac{1}{2}\eta_{\mu\nu} h$, giving

$$\Box \bar{h}_{\mu\nu} = -\frac{16\pi G}{c^4} T_{\mu\nu}, \tag{1.23}$$

the *linearized Einstein field equations*. Observe that equation 1.23 has just become a set of wave equations.

1.2.2 Gravitational Waves through Vacuum and their Effect on Matter

If we now look at equation 1.23 in a vacuum, meaning that there is no source of energy or momentum, we get:

$$\Box \bar{h}_{\mu\nu} = 0 \qquad \Leftrightarrow \qquad \frac{\partial^2}{c^2 \partial t^2} \bar{h}_{\mu\nu} = \nabla^2 \bar{h}_{\mu\nu}, \tag{1.24}$$

which represents a typical wave equation. Solutions for equation 1.24 take the form

$$\Re(H_{\mu\nu} \exp(i k_\lambda x^\lambda)) \qquad \Leftrightarrow \qquad H_{\mu\nu} \cos(\vec{k} \cdot \vec{r} - \omega t), \tag{1.25}$$

where $H_{\mu\nu}$ is the polarization tensor and $k_\lambda = (\omega, \vec{k})$ is the wavevector[3].

Naively, the polarization matrix $H_{\mu\nu}$ has 10 components. However, we will show that only 2 are independent. Similar to hot the Lorenz gauge and other gauge symmetries in electromagnetism reduce the number of polarizations from 4 to 2, the de Donder gauge allows us to impose the *Transverse Traceless* (TT) gauge ($\bar{h}_{0\alpha} = 0$ and $\bar{h}^\alpha_\alpha = 0$) [16, 17], where

$$\begin{aligned} \partial^\mu \bar{h}_{\mu\nu} = 0 \qquad &\Rightarrow \qquad k^\mu H_{\mu\nu} = 0, \\ H_{0\nu} = 0, \qquad &\qquad H^\nu{}_\nu = 0. \end{aligned} \tag{1.26}$$

Observe that in the TT gauge, $\bar{h}_{\mu\nu}$ reduces to $h_{\mu\nu}$. Without loss of generality, we consider the direction of propagation in the z-axis, i.e. $k_\mu = (\omega, 0, 0, \omega/c)$. Equation 1.26 reduces to only 2 independent polarizations, with the general solution

$$h^{TT}_{\mu\nu} = \begin{pmatrix} 0 & 0 & 0 & 0 \\ 0 & H_+ & H_\times & 0 \\ 0 & H_\times & -H_+ & 0 \\ 0 & 0 & 0 & 0 \end{pmatrix} \cos(\omega(t - z/c)), \tag{1.27}$$

[3] It is common to drop the real part on the right-hand side, but it should be kept in mind so that the final solution is real.

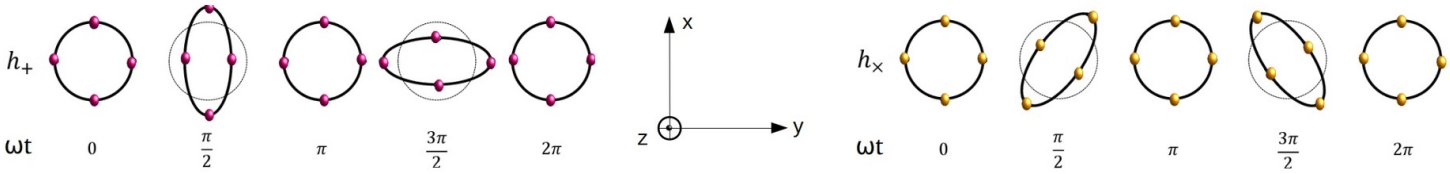

FIGURE 1.2: Visualization of the *plus* and *cross* polarisations, adapted from [19].

where H_+ and $H_\times$ are the *plus* and *cross* polarisations respectively. These polarisations are named after the oscillation pattern they make in the plane perpendicular to the direction of propagation (x-y plane), defining

$$\begin{aligned} h_+(t,z) &= H_+ \cos(\omega(t - z/c)), \\ h_\times(t,z) &= H_\times \cos(\omega(t - z/c)). \end{aligned} \tag{1.28}$$

One can show what they look like by studying the spacetime interval

$$ds^2 = -c^2dt^2 + (1 + h_+(t,z))\,dx^2 + (1 - h_+(t,z))\,dy^2 + 2h_\times(t,z)dxdy + dz^2. \tag{1.29}$$

Consider a ring of particles in the x-y plane, figure 1.2 illustrates the pattern imposed if a GW passes through. On the left, we see the change in particle position when the GW has only plus-polarization ($h_\times = 0$). On the right, we see when the GW has only cross-polarization ($h_+ = 0$).

1.3 Gravitational Wave Generation

To understand the production of GWs, one has to study the inclusion of matter in the wave equation. In this case equation 1.23 becomes

$$\Box h^{TT}_{\mu\nu} = -\frac{16\pi G}{c^4} T^{TT}_{\mu\nu}, \tag{1.30}$$

where $T^{TT}_{\mu\nu}$ is the energy-momentum tensor in the TT gauge. Notice that, in the TT gauge, $h^{TT}_{0\alpha} = 0$ and thus allows us to focus solely on the spatial part. One solves equation 1.30 by integration and using a retarded Greens function[4], giving

$$h^{TT}_{ij}(t,\vec{x}) = \frac{4G}{c^4}\Lambda_{ij;kl}\int dV' \frac{T^{kl}(t - |\vec{x} - \vec{x'}|/c, \vec{x'})}{|\vec{x} - \vec{x'}|}, \tag{1.31}$$

where V is the volume span by $T^{\mu\nu}$ expressed in the coordinate system $\vec{x}'$. $\Lambda_{ij;kl}$ is the transformation tensor

$$\Lambda_{ij;kl} \equiv P_{ik}P_{jl} - \frac{1}{2}P_{ij}P_{kl} \qquad \text{with} \qquad P_{ij} = \delta_{ij} - n_i n_j, \tag{1.32}$$

used to project tensors to the TT gauge, i.e. $T^{TT}_{ij} = \Lambda_{ij;kl}T^{kl}$. n^i is the unit vector the vector along the direction of propagation.

[4]The detailed derivation can be found in [20, 21].

1.3.1 Multipole expansion

As in electrodynamics, when far away from a localized charge distribution, it looks like a point charge, and the potential is, to good approximation, $-(1/4\pi\epsilon_0)Q/r$, where Q is the total charge. For increasing accuracy, one expands this monopole by incorporating a dipole, then a quadrupole, etc. called the multipole expansion. One can do the same for gravitational potentials, see [22] for an in-depth derivation for gravitational radiation. Here we will assume the n^{th} pole has a moment $\int dV' T^{00}[x^{i_1}x^{i_2}\dots x^{i_n}]$.

We start by assuming that the observer of the GW is at a distance r, which is much larger than the size of the source $\vec{x}'$. Therefore $|\vec{x}-\vec{x}'| \simeq r$ is considered to be a constant. Furthermore, we can define the so-called retarded time $t_{ret} = t - r/c$, simplifying equation 1.31 to

$$h_{ij}^{TT}(t,\vec{x}) = \frac{4G}{c^4 r}\Lambda_{ij;kl}\int dV' T^{kl}(t_{ret},\vec{x}'). \tag{1.33}$$

To start the expansion, first observe that the monopole is zero. This is because in the TT gauge, $h_{00}^{TT} = 0 \rightarrow \int dV' T_{00}^{TT} = 0$. This is also the case for the dipole moment, where if we expand $\partial^a(T_{aj}^{TT}x_i)$ and use the conservation of energy-momentum, i.e. $\nabla_\nu T^{\mu\nu} = 0$ to get:

$$\int dV' T_{ij}^{TT} = \int dV'\big(\partial^a(T_{aj}^{TT}x_i') - (\partial^a(T_{aj}^{TT})x_i'\big) = \int dV'(\partial^0(T_{0j}^{TT})x_i' = 0, \tag{1.34}$$

where the first integral is zero because all terms $\partial^a(...)$ will evaluate $T_{\mu\nu}$ at the boundary, where no energy or momentum is present if V fully encapsulates the localized source. The second integral is zero due to the traceless nature of the TT gauge $h_{0\nu}^{TT} = 0$. This might be surprising due to the importance of the dipole in electrodynamics, but remember, in gravity there are no negative gravitational charges, so in the center-of-mass frame, the dipole moment can always be set to zero.

This means that the leading order term is the *mass quadrupole moment*, defined by

$$M^{ij}(t_{ret}) \equiv \int dV' \frac{T^{00}}{c^2}(t_{ret},\vec{x}')x'^i x'^j = \int dV' \rho(t_{ret},\vec{x}')x'^i x'^j, \tag{1.35}$$

where the $1/c^2$ serves to convert energy T^{00} into mass. This term can be found in equation 1.33 by expanding $\partial_a\partial_b(T^{ab}x^i x^j)$:

$$\begin{aligned}\int dV' T^{ij} =& \frac{1}{2}\int dV'\big(\partial_a\partial_b(T^{ab}x^i x^j) + (\partial_0\partial_0 T^{00})x^i x^j\big)\\ =& \frac{1}{2}\ddot{M}^{ij},\end{aligned} \tag{1.36}$$

where again we assume boundary term $(\partial_a\partial_b(...))$ to be zero. Combining Equations 1.33 and 1.36 results into *the quadrupole formula*,

$$h_{ij}^{TT}(t_{ret}) = \frac{1}{r}\frac{2G}{c^4}\Lambda_{ij;kl}\ddot{M}^{kl}(t_{ret}), \tag{1.37}$$

where $\Lambda_{ij;kl}$ can be calculated in the TT gauge with the propagation direction in the z-axis ($\Lambda_{i3;kl} = \Lambda_{3j;kl} = 0$). We find expressions for polarizations h_+ and $h_\times$, defined

in equation 1.28:

$$\begin{aligned} h_+(t_{ret}) =& \frac{2}{r}\frac{G}{c^4}\left(\ddot{M}^{11}(t_{ret}) - \ddot{M}^{22}(t_{ret})\right), \\ h_\times(t_{ret}) =& \frac{2}{r}\frac{G}{c^4}\ddot{M}^{12}(t_{ret}). \end{aligned} \tag{1.38}$$

Note that this expansion depends on the existence of the TT gauge for a given source, which is true for the GWs considered in this thesis. We focus on Compact Binary Coalescence (CBC), where massive bodies like Black Holes (BH) or Neutron Stars (NS) spiral into each other.

Another note is that we only considered this expansion to leading order terms. In general, one can include Higher-Order Modes (HOM) for more accurate models. This is usually done by re-expression the $h(t)$ in terms of spin weighted spherical harmonics $Y_{l,m}$, where

$$h(t) = h_+(t) - ih_\times(t) = \sum_{l\geqslant 2,m} h_{m,l}(t)Y_{l,m} \tag{1.39}$$

with $-l \leq m \leq l$, and $l \geqslant 2$ because lower harmonics are zero (no mono/dipole), where $h_{2,\pm 2}$ corresponds to the quadrupole moment. See [23] for further reading.

1.3.2 Quasi-circular inspiral

To find the expressions for h_+ and $h_\times$, one needs to solve the quadrupole moment M^{ij} in equation 1.38. Here we will show the quasi-circular inspiral approximation, where two non-relativistic point masses are considered to be moving on a circular orbit, slowly shrinking in radius due to gravitational energy being radiated.

Consider the positions of two bodies with mass m_1 and m_2, which follow a circular orbit with radius R from the center of mass.

$$\vec{x}_1(t) = \frac{\mu}{m_1}R\hat{e}(t), \qquad \vec{x}_2(t) = -\frac{\mu}{m_2}R\hat{e}(t), \tag{1.40}$$

where $\mu = m_1m_2/(m_1+m_2)$ is the reduced mass and position defined with unit vector $\hat{e}(t) = (\cos(\omega_{orb}t), \cos(\iota)\sin(\omega_{orb}t), \sin(\iota)\sin(\omega_{orb}t))$, where ω_{orb} is the orbital frequency and ι the inclination angle, as shown in figure 1.3.

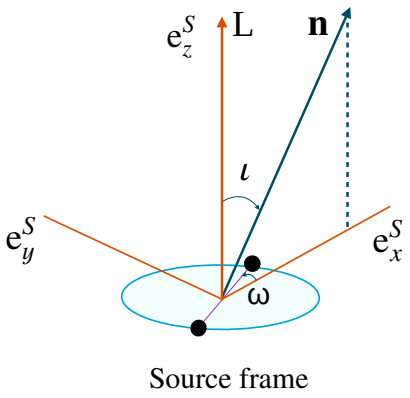

FIGURE 1.3: Representation of the source frame for two point-mass particles on a fixed circular orbit. With the normal vector $\hat{n}$ pointing in the direction from which the propagating GW is observed. Angle ι denotes the inclination angle between orbital momentum vector $\vec{L}$ and normal $\hat{n}$. Adapted from [24].

The expressions for M^{ij} are obtained by filling in the respective components of unit vector $\hat{e}(t)$ into th mass density $\rho(t,\vec{x}) = m_1\delta^3\left(\vec{x} - \frac{\mu}{m_1}R\hat{e}(t)\right) + m_2\delta^3\left(\vec{x} + \frac{\mu}{m_1}R\hat{e}(t)\right)$. Solving the integral in equation 1.35 yields

$$\begin{aligned}\ddot{M}^{11} &= -2\mu R^2\omega_{orb}^2\cos(2\omega_{orb}t),\\ \ddot{M}^{22} &= 2\mu R^2\omega_{orb}^2\cos(\iota)^2\cos(2\omega_{orb}t),\\ \ddot{M}^{12} &= -2\mu R^2\omega_{orb}^2\cos(\iota)\sin(2\omega_{orb}t).\end{aligned} \tag{1.41}$$

Using the quadrupole moment and Kepler's law to substitute $R^3 = G(m_1+m_2)/\omega_{orb}^2$, the resulting expressions for the polarisations take the form:

$$\begin{aligned}h_+(t_{ret}) &= -\frac{4}{r}\left(\frac{G\mathcal{M}_c}{c^2}\right)^{5/3}\left(\frac{\omega_{orb}}{c}\right)^{2/3}\frac{1+\cos^2(\iota)}{2}\cos(2\omega_{orb}t_{\text{ret}})\\ h_\times(t_{ret}) &= -\frac{4}{r}\left(\frac{G\mathcal{M}_c}{c^2}\right)^{5/3}\left(\frac{\omega_{orb}}{c}\right)^{2/3}\cos(\iota)2\sin(2\omega_{orb}t_{\text{ret}}).\end{aligned} \tag{1.42}$$

The parameter $\mathcal{M}_c$ is called the *chirp mass* and together with mass ratio q describe the masses of the binary system

$$\mathcal{M}_c \equiv \frac{(m_1m_2)^{3/5}}{(m_1+m_2)^{1/5}}, \qquad q = \frac{m_2}{m_1}. \tag{1.43}$$

Equation 1.42 describes GWs on fixed orbit. In reality, radiated GWs carry energy, thus orbiting bodies get closer to each other. The energy carried by gravitational waves per time unit through a spherical surface A with radius r is [21]

$$\frac{dE_{GW}}{dt} = \frac{c^3r^2}{16\pi G}\int dA\langle\dot{h}_+^2 + \dot{h}_\times^2\rangle. \tag{1.44}$$

Using equations 1.42 and 1.44 yields

$$\frac{dE_{GW}}{dt} = \frac{32}{5}\frac{c^5}{G}\left(\frac{G\mathcal{M}_c\omega_{orb}}{c^3}\right)^{10/3}, \tag{1.45}$$

the energy radiated per unit of time by GWs generated from circular orbits. This quantity is called the *luminosity* $\mathcal{L}$ of the source.

Using conservation of energy, the radiated energy has to reduce the orbital energy, i.e. $\frac{dE_{\text{orbit}}}{dt} = -\frac{dE_{GW}}{dt}$. If we assume classical adiabatic inspiral, meaning that the orbit and thus ω_{orb} change slowly (orbital radius stay constant over one orbit), orbital energy takes the form

$$E_{\text{orbit}} = -\frac{1}{2}(G^2\mathcal{M}_c^5\omega^2)^{1/3}. \tag{1.46}$$

Observe that taking the time derivative of the orbital energy yields a differential equation for ω_{orb}. It is convenient to define the *gravitational wave frequency* $f_{gw} = \omega_{orb}/\pi$, yielding differential equation

$$\dot{f_{gw}} = \frac{96}{5}\pi^{8/5}\left(\frac{G\mathcal{M}_c}{c^3}\right)^{5/3}f_{gw}^{11/3}, \tag{1.47}$$

with solution

$$f_{gw} = \frac{1}{\pi}\left(\frac{G\mathcal{M}_c}{c^3}\right)^{-5/8}\left(\frac{5}{256}\frac{1}{\tau}\right)^{3/8}, \tag{1.48}$$

where $\tau = t_c - t$. t_c is the coalescence time when the distance between the two masses approaches zero and the orbital frequency diverges. Defining the GW phase $\Phi_{gw}(t) = 2\omega_{orb}t$ yields:

$$\Phi_{gw}(t) = \int dt' 2\pi f_{gw}(t') = -2\left(\frac{5G\mathcal{M}_c}{c^3}\right)^{-5/8}(t_c - t)^{5/8} + \Phi_c, \tag{1.49}$$

where Φ_c is an integration constant and represents the phase at $t = t_c$. The resulting polarisations h_+ and $h_\times$ for a shrinking orbit take the form:

$$\begin{aligned} h_+(t_{ret}) &= -\frac{4}{r}\left(\frac{G\mathcal{M}_c}{c^2}\right)^{5/3}\left(\frac{\pi f_{gw}(t_{\rm ret})}{c}\right)^{2/3}\frac{1+\cos^2(\iota)}{2}\cos(\Phi_{gw}(t_{\rm ret})), \\ h_\times(t_{ret}) &= -\frac{4}{r}\left(\frac{G\mathcal{M}_c}{c^2}\right)^{5/3}\left(\frac{\pi f_{gw}(t_{\rm ret})}{c}\right)^{2/3}\cos^2(\iota)\cos(\Phi_{gw}(t_{\rm ret})), \end{aligned} \tag{1.50}$$

where these equations describe gravitational radiation due to the inspiral of two massive bodies. Observe that the amplitude scales as $1/r$, making the distance of the source one of the most important features describing how loud the signal is. Also, notice that the amplitude scales with the frequency. When the orbits get closer, not only the frequency increases but also the GWs' amplitude.

In reality, the above approximations break down before this time t_c, when orbits cease to remain circular. Therefore, we define the *Innermost Stable Circular Orbit* (ISCO), with radius $R_{ISCO} \simeq 6GM/c^2$, derived in [25]. After R_{ISCO} is reached, other waveform models will be needed to describe the gravitational radiation.

Chapter 2

Waveform Modeling

In chapter 1, we have considered flat spacetime with a small perturbation on top. However, the derivation made so far cannot describe the GW behavior further than the ISCO and even before has shortcomings, because of the strong gravitational interaction at these stages. Unfortunately, the entire set of Einstein equations (1.16) have no analytical solutions to the two-body problem. To model the complete GW waveform, one resorts to numerically solving Einstein equations 1.16, which is computationally expensive for the needed accuracy. Therefore, other approximate methods have been developed for certain regimes of the waveform, such as series expansions and perturbative methods.

In this chapter, we explain the methods used in CBC modeling for BBH events. Generally, the CBC waveform is split into three distinct phases: inspiral, merger, and ringdown; see figure 2.1 for a representation. The inspiral phase, which lasts roughly until the ISCO, is usually approximated with post-Newtonian (PN) techniques [26]. After this, the CBC enters the merger phase [27]. Due to the highly dynamic nature and strong curvatures when BHs merge, numerical relativity (NR) is needed. In the post-merger phase, only a single BH remains and undergoes ringdown [28], which Black Hole Perturbation (BHP) theory can approximate.

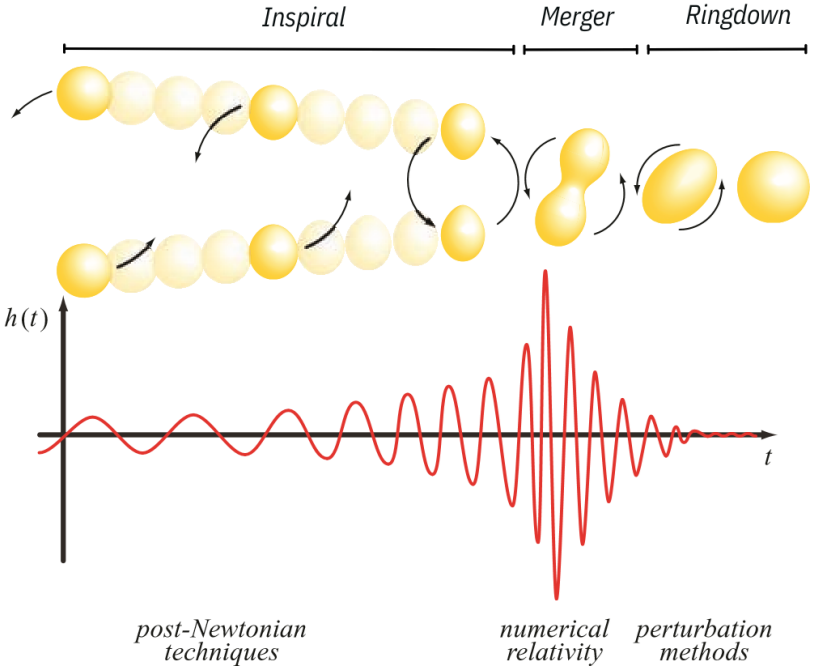

FIGURE 2.1: Representation of a GW signal coming from a binary coalescence with its decomposition in different phases. Adapted from [29].

2.1 Gravitational Wave Parameters

In chapter 1 we have only seen 7 independent parameters. To model a waveform from a BBH event as detected on earth, one can define 15 unique parameters, see table 2.1.

The only intrinsic parameters considered are the individual masses of the BHs m_1 and m_2, and their spin. From observations, we know that any astrophysical system will rotate [30]. As we consider GWs from binary systems, we consider BHs with stellar origin, meaning they also have spin. This spin is characterized by two vectors, $\vec{S}_1$ and $\vec{S}_2$, pointed along the rotation axis of the individual BHs. These spins define the total angular momentum vector $\vec{J} = \vec{S}_1 + \vec{S}_2 + \vec{L}$, where $\vec{L}$ is the angular momentum of the orbit. Each spin vector introduces three independent components for an additional six parameters.

For the extrinsic parameters, we consider the parameters describing the GW waveform as measured on earth, i.e. the detection frame with the distance r between the source and earth. We define the inclination angle ι and polarization angle ψ, characterizing the total angular momentum $\vec{J}$ in the radiation frame at the source, see figure 3.4. The GW arrives at the detector at time t_c with phase Φ_c. To parameterize from what direction of the sky the GW came to the detector we use angles θ and ϕ. The angles ψ, θ, and ϕ are further explained in section 3.1.1.

For modeling purposes and scientific convention, the GW parameters are often differently expressed. In the derivation of chapter 1 we saw it is convenient to cast the component masses m_1 and m_2 into chirp mass $\mathcal{M}_c$ and mass ratio q, see equation 1.43. Also, the sky position of the source is determined by the *declination angle* DEC and the *right ascension* RA instead of θ and ϕ. Because of the earth's rotation, angles relative to the earth's surface (θ and ϕ) will change constantly to point at an astronomical source. The celestial angles DEC and RA keep a constant skymap, see [31]. Similarly, The coalescence time t_c and phase Φ_c are measured in GPS reference time, i.e. when the wave passes Earth's center, which is why t_c is often referred to as *geocentric time*. The distance of the source r is on a cosmological scale. Therefore, we must account for cosmological effects (discussed in section 4.1.1). We replace r by the luminosity distance D_L as a measure of distance.

For modeling spins, coordinates are often expressed in angles between the angular momentum vectors, see figure 2.2. The spin vectors $\vec{S}_i$ are characterized with the dimensionless spin magnitudea_i and the tilt angle θ_i between $\vec{S}_i$ and $\vec{L}$. The difference between the azimuthal angles of the individual spin vectors ϕ_{12}, and the polar and azimuthal angles between total and orbital angular momentum θ_{JL} and ϕ_{JL}. Inclination angle ι is redefined to θ_{JN}.

Intrinsic parameters	m_1	Mass of first body
	m_2	Mass of second body
	$\vec{S}_1$	Spin of first body
	$\vec{S}_2$	Spin of second body
Extrinsic parameters	r	Distance
	ι	Inclination angle
	ψ	Polarization angle
	t_c	Arrival time
	Φ_c	Coalescence phase
	ϕ	azimuth angle earth
	θ	polar angle earth

TABLE 2.1: Intrinsic and extrinsic parameters describing binary coalescence.

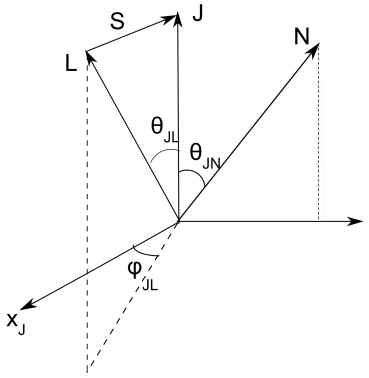

FIGURE 2.2: Coordinates describing total and orbital angular momentum $\vec{J}$ and $\vec{L}$, total spin $\vec{S}$ and propagation direction $\hat{N}$. Figure from [32].

2.2 Model Families

For the analysis of GW data, one has to simulate a waveform. Due to the high computational cost of NR simulation, a collection of approximate numerical models has been established. Current waveform models for data analysis are implemented in the LSC Algorithm Library (LAL) Simulation [33]. Here we outline three main model families within LALSIMULATION: TAYLOR, EOB, and IMRPHENOM. The meaning of their respective pre- and suffixes is summarized in table 2.2, see [26, 34] for a complete overview.

The TAYLOR waveform uses a plethora of different PN approximation schemes to get a time-domain waveform of the inspiral phase [35]. These waveforms are then transformed using the stationary phase approximation (discussed in section 4.1.3) to the frequency-domain models [36]. One can also incorporate spin into the PN formalism [30, 37, 38].

Although the inspiral is the largest part of the signal, one would like to model the complete inspiral-merger-ringdown (IMR) waveform, which approximants EOB [39, 40] and IMRPHENOM [41–47] aim to do.

EOB uses the Effective One-Body (EOB) approximation, where one considers the two rotating bodies into one body moving in an effective potential. How one formulates this in GR is beyond the scope of this thesis, and details can be found in [39, 40]. Here, one can also use the PN formalism for solving the present potential, which solution can be extended into the merger phase. Spin effects can also be incorporated by modification of the effective potential. With this, one can model the entire waveform, and calibrate it with NR. One downside of EOB is that it is slow to evaluate numerically.

The family used in this work is IMRPHENOM. The main goal of the waveform approximants in this family is to be faster than EOB waveforms while maintaining a comparable level of accuracy. The IMRPHENOM model is made by "stitching" together three parts: PN inspiral, merger-ringdown, and the intermediate part between the former two parts. Each component is parametrized in the frequency domain and calibrated using waveforms from NR simulations. This family includes non-spinning [41], aligned spin [42–44], and spin precession [45] models. The IMRPHENOMX subfamily is quite a new Phenom model, which improves upon its older counterparts, see [47]. In this work, we make use of the spin precession model IMRPHENOMPV2 [46].

Model Family	pre-/suffix	description
TAYLOR	-T	Time domain Taylor PN approximant
	-F	Frequency domain Taylor approximant
	SPIN-	Spinning case models
EOB	-	Effective one-body waveform
	-NR	Calibrated against numerical relativity
	S-	Accounting for spin
IMRPHENOM	-A	Models non-spinning binaries
	-B/C/D	Models spinning, but non-precessing binaries
	-P(-V2,-V3)	Models precessing binaries
	-X	Updated models for aligned or precessing binaries
	-HM	Include higher order modes

TABLE 2.2: Partial overview of waveform approximates and their pre- and suffixes withing LALSUITE [33, 34]

2.3 Modeling Techniques

Current waveform models use various methods to find a good balance between model accuracy and computational speed. This section seeks to sketch the concepts of the common methods and approximations used to describe the GW emission of CBC signals. We emphasize that the explanations given here are a qualitative overview, for an in-depth description of GW Modeling, we refer the reader to chapters 31-40 of [48].

Each modeling method is useful within a given regime. Figure 2.3 shows the different cases where methods are used in parameter space. The y-axis describes the masses of the system with the symmetric mass ratio

$$\eta = \frac{m_1 m_2}{(m_1 + m_2)^2}, \tag{2.1}$$

where the closer this value is to zero, the larger the difference in masses of the binary. The x-axis represents the orbital speed of the binary objects. Given Kepler's third law, orbital speed scales inversely with radius, such that the x-axis describes how close to each other the bodies are orbiting, represented by the compactness.

Observe that the PN formalism is a good description for the low-velocity regime, i.e. the inspiral phase. For the high-velocity regime corresponding to the merger and ringdown phases, this approximation breaks down. BHP theory is only valid for low symmetric mass ratios. This can be applied to the ringdown phase. For the rest of the parameter space, the only accurate method is using NR simulations.

A waveform model combines these different parts. One seeks to make fast-to-compute models that cannot rely directly on NR simulations. This section describes how combining the different approaches yields waveform model IMRPHENOMPV2 [46].

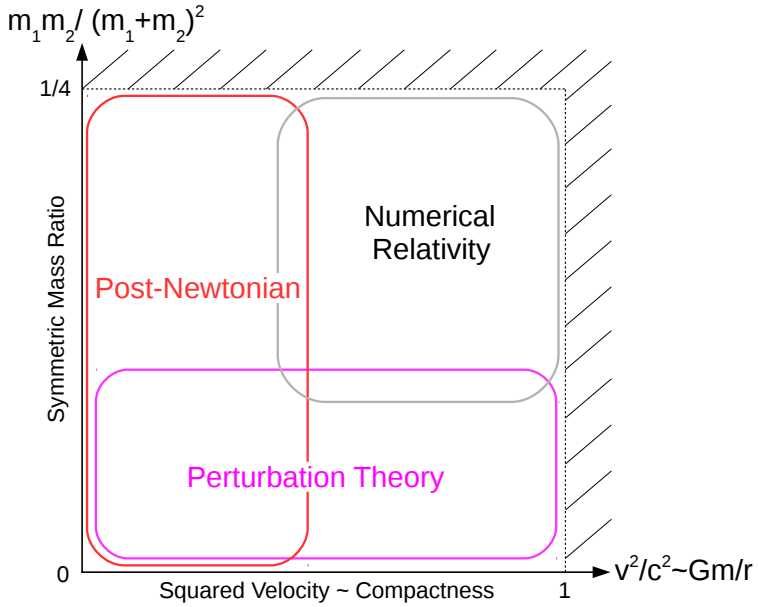

FIGURE 2.3: Illustration of the regions in parameter space where different methods of solving the GW waveform are used. On the x-axis, the orbital velocities of the bodies (illustrating compactness), and on the y-axis, the symmetric mass ratio (higher value equals more similar mass). Figure from [49].

2.3.1 Numerical Relativity

To establish the theoretical model for a waveform, we need to solve the Einstein equations (1.16) corresponding to the source of the GW. The only method that does not make any analytic approximation to the Einstein equations is NR, although some numerical approximations are needed. Nevertheless, NR is the most accurate tool for modeling GW sources. One major drawback of this method is that these numerical calculations are computationally intensive, requiring a supercomputer level of memory. However, there are ongoing efforts to accelerate these numerical methods and make them more efficient [50].

As a tensorial equation, the Einstein equations are not an explicit partial differential equation (PDE). This makes their calculations difficult to solve through numerical computation. Therefore, it is necessary to recast the Einstein equations in a format suitable for numerical calculations. There are several methods to achieve this, see chapter 9.4 of [29]. NR solves spacetime curvature on a mesh. It took several decades to develop an NR model that was numerically stable, the solution was to ensure a high mesh resolution in areas of high curvature. Techniques such as adaptive mesh refinement made it possible to create the first GW waveforms [51]. Nevertheless, several challenges are still present in modern NR, see [52] for an overview of state-of-the-art NR models.

Over the last decade, several NR waveforms have been developed and are capable of describing a variety of elements from CBCs, creating catalogs of publicly available waveforms, for example, see [53–56]. These waveforms are then used to make NR surrogate waveforms or to calibrate and test waveform approximants.

2.3.2 Post-Newtonian expansion

In the derivation presented in chapter 1, the Newtonian orbital dynamics (considering the quadrupolar radiation of orbital energy) in linearized gravity was presented. However, the inspiral phase can be represented more accurately by using the PN formalism. The main assumptions in this formalism are that the source is at once *slowly moving* and *weakly stressed*, i.e.

$$\frac{v}{c} \ll 1 \qquad \text{and} \qquad \left|\frac{T^{ii}}{T^{00}}\right|^{\frac{1}{2}} \ll 1. \tag{2.2}$$

It is conventional to define small dimensionless parameter x, related to orbital velocity v, and is by convention defined to the orbital frequency using Kepler's law:

$$x \equiv \frac{v^2}{c^2} \equiv (GM\omega_{orb}/c^3)^{2/3} \tag{2.3}$$

The idea of this approximation is to Taylor expand the binding energy $\mathcal{E}(x)$ and flux $\mathcal{F}(x) = -d\mathcal{E}/dt$ of the inspiral waveform in terms of x. For the exact analytical derivation, we refer the reader to [26, 57].

In this work, we make use of IMRPHENOMPV2 [46], a spin pressesing model of IMRPHENOMD [44]. The inspiral of this model is based on the standard frequency-domain PN approximate TAYLORF2 [36], which itself uses elements of its time-domain counterparts TAYLORT2 [35].

For PN in the time domain, one obtains a pair of parametric equations for GW phase Φ and time t [57] by expanding the ratio of effective flux over binding energy

[26, 58],

$$\begin{aligned} \frac{d\Phi}{dt} &= \frac{v^3}{M} \quad \rightarrow \quad \frac{d\Phi}{dv} = \frac{v^3}{M}\frac{dt}{dv}, \\ \frac{dv}{dt} &= -\frac{\mathcal{F}}{(d\mathcal{E}/dv)} \quad \rightarrow \quad \frac{dt}{dv} = -\frac{(d\mathcal{E}/dv)}{\mathcal{F}}, \end{aligned} \tag{2.4}$$

and integrating the expanded forms of $\mathcal{E}$ and $\mathcal{F}$ over dimensionless parameter x,

$$\begin{aligned} \Phi_{PN}^{(approx)}(x) =& \Phi_{ref}^{(approx)} + \Phi_{N}^{(approx)} \sum_{n=0}^{PN} \hat{\Phi}_n(x) x^n, \\ t_{PN}^{(approx)} =& t_{ref}^{(approx)} + t_{N}^{(approx)} \sum_{n=0}^{PN} \hat{t}_n(x) x^n, \end{aligned} \tag{2.5}$$

with reference quantities $\Phi_{ref}^{(approx)}$ and $t_{ref}^{(approx)}$ as integration constants, and where $\Phi_{N}^{(approx)} \cdot \hat{\Phi}_n(x)$ and $t_{N}^{(approx)} \cdot \hat{t}_n(x)$ are the n^{th} order prefactors of the PN expansion. The PN expansion takes steps of $\frac{1}{2}$ because the expansion is defined in orders of velocity ($v^k \sim x^{k/2}$). For TAYLORT2, coefficients for equations 2.5 are derived to the 3.5 PN order, see [57] for their full expressions.

The analog to TAYLORT2 in the frequency domain is TAYLORF2, where we re-expand the PN series and integrate in terms of frequency f instead of t. One uses the Stationary Phase Approximation (SPA) (further discussed in section 4.1.3) to re-express the waveform in Fourier amplitude $A(f)$ and the Fourier-domain phase $\Psi(f)$, where the velocity is related to frequency via $\frac{v^2}{c^2} = (GM\pi f/c^3)^{2/3}$. This yields

$$\Psi_{PN}^{(approx)}(x) = \Psi_{ref}^{(approx)} + \Psi_{N}^{(approx)} \sum_{n=0}^{PN} \hat{\Psi}_n(x) x^n, \tag{2.6}$$

where $\Psi_{ref}^{(approx)}$ is a reference phase as integration constants and $\Psi_{N}^{(approx)} \cdot \hat{\Psi}_n(x)$ are the n^{th} order prefactors of the PN expansion. Also for TAYLORF2 this is done to 3.5 PN order, see [57] for derived expressions for $\Psi_{3.5}^{(F2)}(x)$. An important note is that phases Φ and Ψ can be re-expressed into each other via the SPA.

The amplitude $A(f)$ of a GW does not change much and therefore often approximated to the leading order as

$$A_{PN}^{(F2)}(f) \simeq A_0 f^{-7/6} \propto \frac{M^{5/6}}{D_L}\sqrt{\frac{2\eta}{3\pi^{1/3}}} f^{-7/6}, \tag{2.7}$$

with M, η, and D_L the source's total mass, symmetric mass ratio, and luminosity distance.

For the inspiral part of the waveform model IMRPHENOMD, a combination of the PN parts from TAYLORF2 and a fitting function are used to construct the phase and the amplitude,

$$\begin{aligned} \Phi_{\text{ins}} =& \Phi_{PN}^{(\text{F2})} + \frac{1}{\eta}\left(\sigma_0 + \sigma_1 f + \frac{3}{4}\sigma_2 f^{3/4} + \frac{3}{5}\sigma_3 f^{5/3} + \frac{1}{2}\sigma_4 f^2\right), \\ A_{\text{ins}} =& A_{\text{PN}} + A_0 \sum_{i=1}^{3} \rho_i f^{\frac{6+i}{3}}, \end{aligned} \tag{2.8}$$

with σ_i and ρ_i the fitting parameters, found by fitting the ansatz to NR waveforms [44, 59].

The complicated phenomenology of precessing BBHs makes waveform modeling challenging, but it can be done by the so-called twisting up of IMRPHENOMD into IMRPHENOMPV2 [46]. This is done via a precession correction to $h_{l,m}$ defined in the HOM expansion in equation 1.39,

$$h^P_{2,m} = e^{-im\alpha_{PN}} \sum_{|m'|=2} e^{im\epsilon_{PN}} d^2_{m',m}(-\beta_{PN}) h_{2,m'}, \tag{2.9}$$

where angles α, β, and ϵ are related to the angles between the spin vectors $\vec{S}_i$ and orbital angular momentum $\vec{L}$ and are PN approximated, see [30, 46, 60]. $d^2_{m',m}$ denote the Wigner d-matrices, see [61].

IMRPHENOMPV2 uses a single-spin approximation parameterised by the aligned effective-spin parameter χ_{eff} (which comes naturally out of the 1.5PN order in frequency domain) and the precession effective-spin parameter χ_p, expressed in the spin parameters defined in section 2.1:

$$\begin{aligned} \chi_{eff} =& \frac{a_1 \cos(\theta_1) + q a_2 \cos(\theta_2)}{1+q}, \\ \chi_p =& \max\Big(a_1 \sin(\theta_1), \frac{4q+3}{4+3q} q a_2 \sin(\theta_2)\Big), \end{aligned} \tag{2.10}$$

which are often used to describe spin measurements from processing BHs. With this, we have arrived at the complete description of the inspiral for IMRPHENOMPV2, where the waveform is described in the frequency domain with amplitude $A^{(Pv2)}_{\text{ins}}$ and phase $\Phi^{(Pv2)}_{\text{ins}}$.

2.3.3 Black Hole Perturbation

The importance of perturbation theory cannot be understated in the analytical description of GWs, as we started from perturbed linearized gravity in section 1.2.1. Historically, perturbative analysis of GW sources has largely focused on PN theory, which fails to go much further than the inspiral phase. Strong-field perturbation theory is therefore essential to explain the waveform of the quasi-normal ringdown following the merger of a binary system. One essential method to describe the strong field dynamics after the merger is black hole perturbation (BHP) theory.

In BHP, we consider the metrics of perturbed isolated black holes. Isolated, stationary black hole spacetimes are described by either the *Schwarzschild* or the *Kerr* metric, depending on whether they are non-rotating or rotating respectively. Their corresponding metrics are studied in extent, for further reading see [16, 17].

We assume the metric and stress-energy tensors can be expanded in powers of a small parameter ϵ,

$$\begin{aligned} g^{exact}_{\mu\nu} =& g_{\mu\nu} + \epsilon h^{(1)}_{\mu\nu} + \epsilon^2 h^{(2)}_{\mu\nu} + \mathcal{O}(\epsilon^3), \\ T_{\mu\nu} =& \epsilon T^{(1)}_{\mu\nu} + \epsilon^2 T^{(2)}_{\mu\nu} + \mathcal{O}(\epsilon^3), \end{aligned} \tag{2.11}$$

where $g_{\mu\nu}$ is the metric we choose to perturb. The perturbations show up as additional terms in the Einstein equations 1.16, generally considered only at first order:

$$G^{(1)}_{\mu\nu}[h^{(1)}] = \frac{8\pi G}{c^4} T^{(1)}_{\mu\nu}. \tag{2.12}$$

This has then to be solved in a BH metric, the calculations of which are beyond the scope of this thesis and we refer the reader to [62].

In this case, we study PN initial conditions, in the Close-Limit (CL) expansion (head-on collisions), where the metric takes the form:

$$g_{\mu\nu}^{\rm PN} = g_{\mu\nu}^{\rm Schwarz} + h_{\mu\nu}, \tag{2.13}$$

where $g_{\mu\nu}^{\rm Schwarz}$ is the Schwartschild metric of a BH with mass M (total mass of the binary in one BH). The perturbation $h_{\mu\nu}$ in this limit becomes,

$$h_{\mu\nu} = G \sum_{n\geq 0} \sum_{k\geq 0} \hat{h}_{\mu\nu}^{(n,k)} \epsilon_{PN}^{n} \epsilon_{CL}^{k+1} + \mathcal{O}(G^2), \tag{2.14}$$

where $\hat{h}_{\mu\nu}^{(n,k)}$ are the coefficients of the expansion in both, which in turn is done to PN order n ($\epsilon_{PN} \sim \frac{v^2}{c^2}$ or known as parameter x in PN literature) and CL order k [28, 63][1]. In the CL, we expand under,

$$\epsilon_{CL} \sim \frac{r_{12}}{r} \ll 1, \tag{2.15}$$

where the binary separation r_{12} is sufficiently small compared to the distance r from any field point to the center of mass of the source. The CL calculations can then be characterized as a superposition of complex frequencies known as Quasi-Normal Modes (QNMs), see [65] for an overview of QNM expansions for different metrics and starting conditions.

This is used in IMRPHENOMD (and by extension in IMRPHENOMPV2) to characterize the features from the end of the merger to the ringdown (MRD) of the GW. This is modeled by defining the ringdown frequency $f_{\rm RD}$ and its damping frequency $f_{\rm damp}$. The fitting functions for the phase and the amplitude take the form [44, 59]:

$$\begin{aligned} \Phi_{\rm MRD} =& \frac{1}{\eta}\left(\alpha_0 + \alpha_1 f - \alpha_2 f^{-1} + \frac{4}{3}\alpha_3 f^{3/4} + \alpha_4 \arctan\left(\frac{f-\alpha_5 f_{\rm RD}}{f_{\rm damp}}\right)\right), \\ A_{\rm MRD} =& A_0 \gamma_1 \frac{\gamma_3 f_{\rm damp}}{(f-f_{\rm RD})^2 + (\gamma_3 f_{\rm damp})^2)} \exp\left(\frac{\gamma_2 (f-f_{\rm RD})}{\gamma_3 f_{\rm damp}}\right), \end{aligned} \tag{2.16}$$

with α_i and γ_i the fitting parameters.

To bridge the gap between the inspiral and the merger ringdown model, an intermediate (int) phase and amplitude are provided as ansatz based on NR data,

$$\begin{aligned} \Phi_{\rm int} =& \frac{1}{\eta}\left(\beta_0 + \beta_1 f + \beta_2 \ln(f) - \frac{\beta_3}{3} f^{-3}\right), \\ A_{\rm int} =& A_0(\delta_0 + \delta_1 f + \delta_2 f^2 + \delta_3 f^3 + \delta_4 f^4), \end{aligned} \tag{2.17}$$

where β_i and δ_i are fitting parameters, they need to match NR *and* require the boundary conditions to be met, fixed by matching phase and amplitudes with the merger-ringdown and the inspiral.

How these parameters are obtained can be found in [44, 59]. Importantly, stitching together the PN inspiral, intermediate, and merger-ringdown parts yields a waveform model that is accurate and fast to compute.

[1] We do also do an expansion in G, called the Post-Minkowskian expansion [64].

Chapter 3

Detection and Analysis of Gravitational Waves

The first hints of the existence of GWs came from indirect detections. In 1977, the measurements of binary pulsar systems, by Hulse and Taylor [5] gave the observational evidence. Pulsars are rapidly spinning NSs, which radiate a characteristic jet of electromagnetic radiation out of their polar regions, resulting in periodic pulses measured on Earth [66]. The Hulse-Taylor binary manifested a decay in the orbital period. Thr latter matched the prediction made when accounting for energy losses through GW emission, yielding a Nobel prize for Hulse and Taylor in 1993.

For the measurement of GWs from CBCs, the development of extremely precise instruments was needed. Many years of experiments with possible detector designs and data analysis algorithms led to the current detection facilities using laser interferometers [21]. The construction of the Laser Interferometer Gravitational-wave Observatory (LIGO) [67] and Virgo [68] detectors led to all the 93 GWs confirmed today, with many candidate GW observations [69] still yet to be confirmed. This network of detectors is now extended with the KAGRA [70] detector and upgraded Advanced LIGO [71] and Virgo [72], with the construction of LIGO-Inda [73] on its way. Development and planning of the next generation of detectors have started, with projects such as Einstein Telescope (ET) [74] and Cosmic Explorer (CE) [75]. Also, plans of constructing a space-based interferometer LISA [76, 77] have been formally adopted and accepted by the European Space Agency as of this year. With these detectors, we can probe a wide range of the GW frequency spectrum, see figure 3.1.

A more recent development to probe GWs is the use of pulsar timing arrays [78]. Here the periodic nature of pulsars is used as a clock, timing the arrival time of pulses of electromagnetic radiation. If a GW passes, a slight change in the time of arrival between pulses can be measured. In 2021, the NANOGrav Collaboration released 12.5 years of observation [79]. This detection gave the first hints into the existence of a GW with wavelengths on an astronomical scale, GW background, and many other insights [80]. However, this area of research is still in its infancy and further measurements are needed to confirm these observations.

Finding GWs inside of the data is a hard problem. Due to the large sources of noise for interferometers and the small signal amplitude, extracting the faint signal requires advanced analysis techniques. In this thesis, we focus on the Parameter Estimation (PE) of CBC.

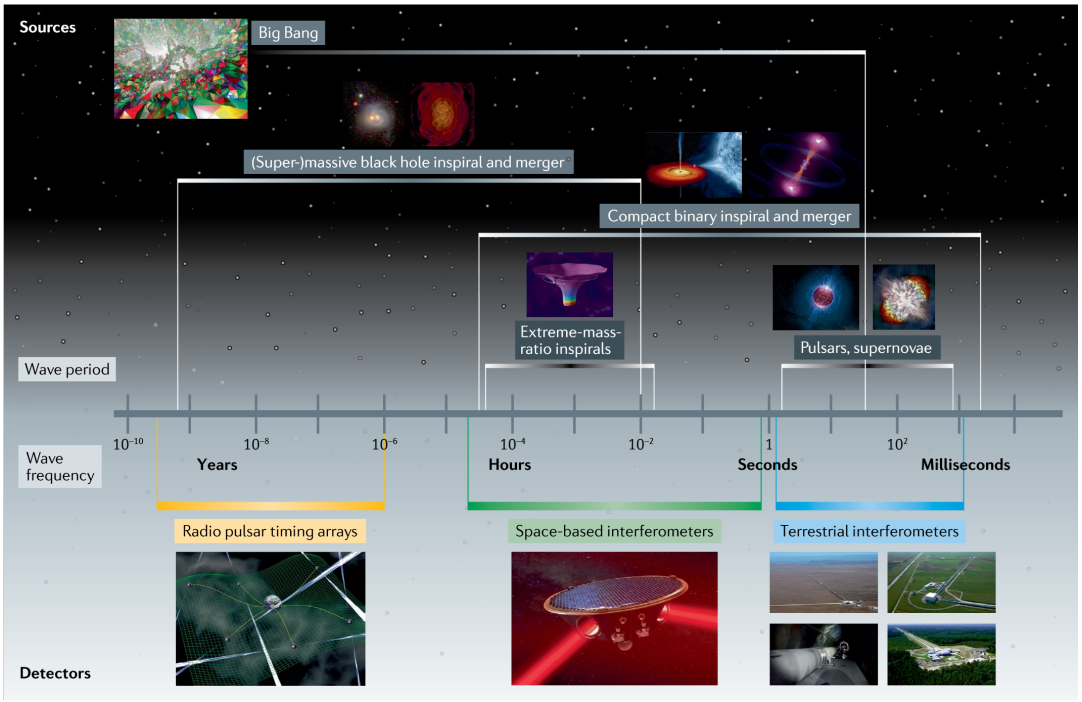

FIGURE 3.1: The spectrum of GWs, showing different source classes above and sensitive of different detectors below. Figure from [81].

3.1 Laser Interferometers

Although GWs are generated from the densest objects in the universe, spacetime appears to be quite rigid. When calculating the magnitude of deformation of spacetime by the time the GW reaches Earth, one finds it is ten thousand times smaller than the nucleus of an atom [82]. A technique capable of measuring this is the laser interferometer, pioneered by the experiment of Michelson and Morley [83], originally designed to measure the luminiferous aether (the historically postulated medium of light).

The general concept of an interferometer goes as follows: a focused beam of light is split into two different paths. After some distance is traveled, these paths are recombined back together. At this point, the light of the two paths interferes with itself. A photodetector then measures the intensity, measuring constructive or destructive interference depending on the phase difference between the light from the two paths. With this, one can study differences on an incredibly small scale, because of the small wavelength of light.

Current GW detectors use this concept as follows. A laser beam is sent onto a beam splitter that separates the light between two arms, with lengths $L_\perp$ and $L_\parallel$, perpendicular and parallel to the beam. A mirror, or the so-called test-mass, at the end of the arms, reflects the light. The combined light of the two arms is then collected and the interference is measured with a photodetector. This is called the strain of the detector. Due to the difference in traveled distance $\Delta L = 2L_\perp - 2L_\parallel$, the observed interference will change. If a GW passes through the detector, it will stretch and contract the spacetime interval between a ring of particles (test masses) according to polarizations h_+ and $h_\times$, as illustrated in figure 1.2. This introduces a path difference ΔL. For a schematic visualization, see figure 3.2.

To measure significant displacements, detectors require long arms, with 3 km

and 4 km for Virgo and LIGO respectively. These arms are maintained under ultra-high vacuum to ensure the laser is unimpeded by anything that could scatter, refract, reflect, or absorb its photons. However, this is insufficient to be sensitive to the contractions caused by a typical GW (order 10^{-18} m). A slue of optical techniques is used to get the best sensitivity out of the detector, see the schematic in figure 3.3. Here we describe the key components of the detector setup, see [84] for a deeper explanation.

Fabry-Perot cavities: This technique places one semitransparent mirror in each arm, making the light bounce numerous times between mirrors before it reaches the detector. This multiplies the path difference around 50 times, greatly increasing the sensitivity [85].

Seismic isolation: The mirrors are suspended masses in a multi-stage pendulum system. By tuning the resonant frequencies of the suspension system, one can dampen certain frequencies. This apparatus reduces the undesired motion of the test-mass due to seismic motion by about a factor of 10^{12} [86].

Power recycling cavities: Introducing a one-way mirror before the beam splitter, laser light that would have escaped is recycled back into the system. This plays a critical role in boosting the laser power within the interferometer arms, improving sensitivity [87].

Modulators and Mode cleaners: An optical modulator allows precise control over light properties, typically used to impose a phase modulation. Cleaners help to maintain the laser beam's purity and spatial mode. Together they provided a very well-defined phase, which allows for precise measurements of phase differences [84].

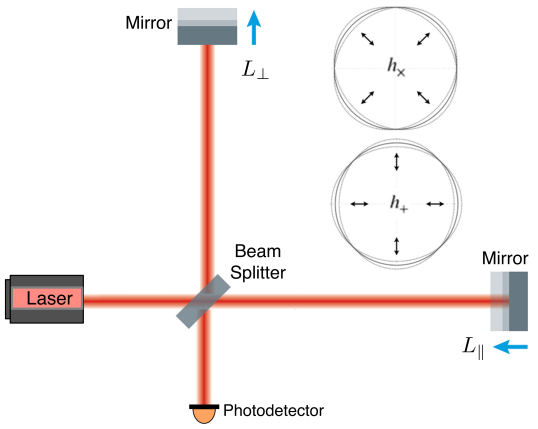

FIGURE 3.2: Simplified schematic an interferometer.

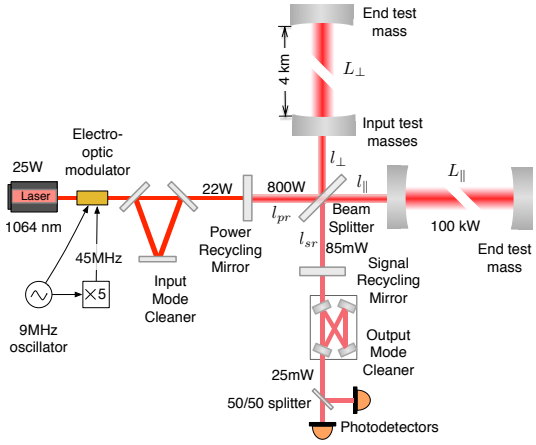

FIGURE 3.3: Realistic schematic of the LIGO interferometer setup. Figure from [84].

3.1.1 Detector Response and Sensitivity

Now that we have shown how the detector allows for the measurement of the GW strain, we have to characterize how an incoming GW affects this data. The change in path length of a given arm δL depends on how the GW goes through the detector

which involves calculating the spacetime interval

$$\int_0^{L_\parallel} \sqrt{ds_\parallel^2} = L + \delta L_\parallel \qquad \text{and} \qquad \int_0^{L_\perp} \sqrt{ds_\perp^2} = L + \delta L_\perp, \tag{3.1}$$

where L is the arm length if no GW is present. These define the GW strain

$$h = \frac{\Delta L}{L} = \frac{\delta L_\perp - \delta L_\parallel}{L}, \tag{3.2}$$

defined in the detector frame [88]. The description of the spacetime interval in the radiation frame is given by equation 1.29, but this only describes an incoming GW propagating along the z-direction in the detector frame. Therefore, we need to transform the polarizations h_+ and $h_\times$ from the radiation (defined by the TT-gauge propagating in the z-direction) into the detector frame (with x and y-axis defined as the parallel and perpendicular arms of the detector), see figure 3.4. We define the *antenna pattern functions*: F_+ and $F_\times$, which are the projection factors to express the polarizations of the GW source in the detector frame, yielding the strain

$$h(t) = F_+(\theta, \phi, \psi) h_+(t) + F_\times(\theta, \phi, \psi) h_\times(t), \tag{3.3}$$

with $h_+(t)$, $h_\times(t)$ the polarisations defined in equation 1.50. The antenna pattern functions are defined as [88]

$$\begin{aligned} F_+(\theta, \phi, \psi) =& \frac{1}{2}(1 + \cos(\theta)^2)\cos(2\phi)\cos(2\psi) - \cos(\theta)\sin(2\phi)\sin(2\psi), \\ F_\times(\theta, \phi, \psi) =& \frac{1}{2}(1 + \cos(\theta)^2)\cos(2\phi)\sin(2\psi) + \cos(\theta)\sin(2\phi)\cos(2\psi). \end{aligned} \tag{3.4}$$

Note that for some angles θ, ϕ, and ψ, the pattern functions are zero, meaning that incoming GWs from these directions will not be measurable. Therefore, an L-shaped detector has more or less sensitivity depending on the sky position of the source.

Observe that the detector and thus angles θ and ϕ are relative to the Earth's surface. Therefore, they will change constantly with the rotation of the Earth, when pointing in a similar position in the sky. To avoid this, the sky position of a source is often expressed in equatorial coordinates, composed of the right ascension RA and declination DEC, see [31].

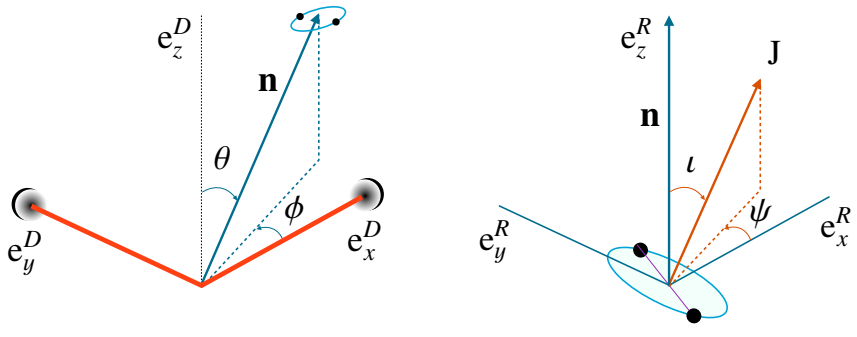

FIGURE 3.4: Representation of the detector and radiation frame. With the normal vector $\hat{n}$ pointing in the propagation direction of the GW. Angles θ and ϕ denote the polar and azimuth angles of $\hat{n}$ in the detector frame, while ι and ψ denote the polar and azimuth angles of total angular momentum $\hat{J}$ in the radiation frame. Figure from [24].

3.2 Dealing with the Noise

Despite all the technologies used to reduce the noise in a GW detector, their respective strain data is still riddled with noise. Understanding noise sources is beyond the scope of this thesis and we refer the interested reader to [89]. A detector's sensitivity is generaly represented by the Power Spectral Density (PSD) or its square root Amplitude Spectral Density (ASD), see figure 3.5. The PSD measures the magnitude of noise at specific frequencies (lower PSD equals less noise).

When a GW is present in the detector, the recorded data d is

$$d(t) = n(t) + h(t), \tag{3.5}$$

where n is the noise, and h is the GW strain. When we measure the noise over a period T and perform a Fourier transform ($\tilde{n}(f)$), it is characterized as

$$\langle |\tilde{n}(f)|^2 \rangle_T = \frac{S_n(f)}{2T}, \tag{3.6}$$

where $\langle . \rangle$ denotes an average. The function $S_n(f)$ now illustrates the PSD.

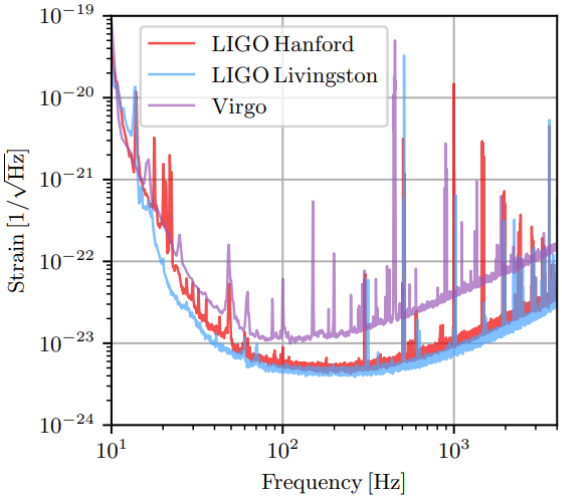

FIGURE 3.5: Amplitude spectral density (square root of the power spectral density) of the LIGO and Virgo detectors during the third observation run [90].

To compare measurements against the noise, we define the noise-weighted inner product (one can see this as a noise-weighted average)

$$\langle a \mid b \rangle = \int_{-\infty}^{\infty} \frac{\tilde{a}^*(f)\tilde{b}(f) + \tilde{a}(f)\tilde{b}^*(f)}{S_n(f)} df = 4\Re \left(\int_0^{\infty} \frac{\tilde{a}^*(f)\tilde{b}(f)}{S_n(f)} df \right), \tag{3.7}$$

where a and b are arbitrary functions. This allows us to define how well a possible signal template s matches the data d, i.e. $\langle d \mid s \rangle$, without worrying about noise effects. This procedure is the basis of matched filtering, see [91]. This allows us to define the Signal-to-Noise Ratio (SNR) ρ, defined by

$$\rho = \langle d \mid \hat{s} \rangle \qquad \text{where} \qquad \hat{s}(t) = \frac{s(t)}{\sqrt{\langle s \mid s \rangle}}, \tag{3.8}$$

where $\hat{s}$ is defined to normalize the signal template.

Let a template signal s exactly equal a signal GW strain h in data d, and neglecting noise effects, such that $d \approx h$, we can define the optimal SNR

$$\rho_{\text{opt}} = \langle h \mid \hat{h} \rangle = \frac{\langle h \mid h \rangle}{\sqrt{\langle h \mid h \rangle}} = \sqrt{\langle h \mid h \rangle}. \tag{3.9}$$

This quantifies the best SNR possible for a given signal and is often used to describe how measurable this signal is. With a network of multiple detectors, one defines the total SNR of the network as

$$\rho^2_{\text{combined}} = \sum_{n=1}^{N_{\text{det}}} \rho^2_n, \tag{3.10}$$

where N_{det} is the number of detectors. Currently, there are three observing detectors active, see [92] for the live status of the GW detector network.

Figure 3.6 illustrates the process of signal identification in the data. In the top row, we see the SNR plotted over time for the best-fitting template for GW170814 [93]. Observe that at the time the template fits the data best, we see a spike in SNR, meaning a signal could be present. In this case, the GW was detected on the fourteenth of August 2017. There is a slight time difference between the peaks. This is due to the different locations on Earth where the detectors are situated, yielding a small time delay due to the GW propagation speed.

In the bottom three plots of figure 3.6 is plotted the whitened strain data (thin lines), meaning it is weighted with the ASD to make the noise less visible. The thick grey line plotted on top shows the 90% best-fitting signal templates.

In reality, detector noise can be non-Gaussian, and so-called glitches can be present in the data [94]. Therefore, it is important to quantify the statistical significance before one confirms a detection. One does this by computing the probability distribution of ρ_{combined}. This can be done by time-sliding the templates per detector $s(t + \Delta t_{\text{shift}})$ where Δt_{shift} is larger than the travel time between detectors. This ensures that the calculated SNR cannot correspond to astronomical origin and thus is computed over noise. Making a histogram of the ρ_{combined} calculated over many different values for time yields the so-called background probability distribution of ρ_{combined}. To quantify a detection, one computes the area under the probability distribution larger the measure SNR ($P(> \rho_{\text{measured}})$). This yields the false-alarm rate, i.e. the expected time it will take for this SNR to be detected due to purely noise. For GW170814 this rate was 1 in 27000 years [93].

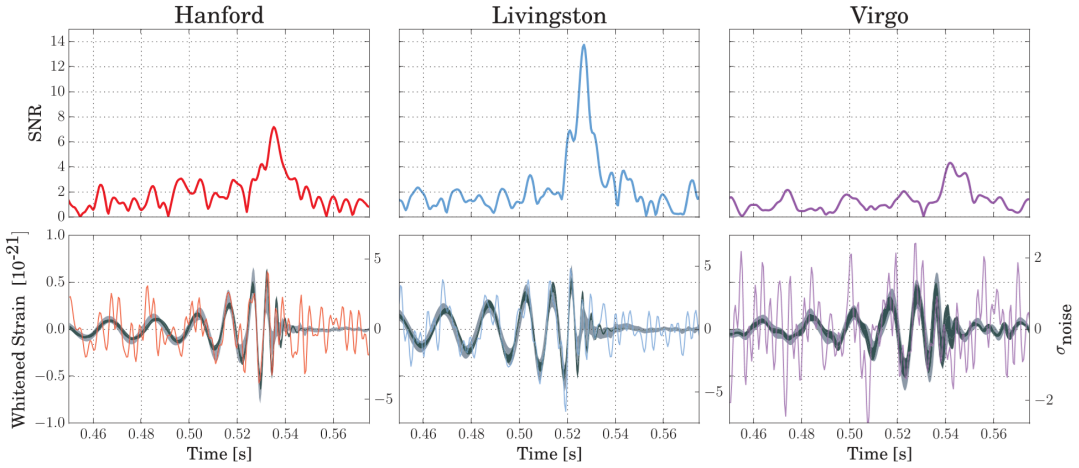

FIGURE 3.6: Detector SNR and whitened strain of event GW170814. Adapted from [93].

3.3 Parameter Estimation

A logical next question is: How to find the parameters of the signal? Let $h(\boldsymbol{\theta}; t)$ define a template, with

$$\boldsymbol{\theta} = (\mathcal{M}_c, q, \vec{S}_1, \vec{S}_2, D_L, \iota, \psi, \theta, \phi, t_c, \Phi_c), \tag{3.11}$$

the GW parameters of a waveform in the detector frame. In this section, we will briefly describe the techniques used to find the parameters $\boldsymbol{\theta}$ that best fit the data, hence the name Parameter Estimation (PE). The main tool used in PE is Bayesian inference [95].

Let us start by introducing Bayesian statistics. Let A and B be two parameters, that are probabilistically conditional on each other. To link different conditional probabilities, one uses Bayes' theorem [95]:

$$P(B \mid A) = \frac{P(A \mid B)P(B)}{P(A)}. \tag{3.12}$$

In words, this reads as follows: the probability of drawing parameter $B \sim P(B \mid A)$ given a drawn value of parameter A, equals the probability of drawing parameter $A \sim P(A \mid B)$ given a drawn value of parameter B, times the probability of parameter value $B \sim P(B)$ being drawn divided by the probability of parameter value $A \sim P(A)$ being drawn. For GWs, A would be measuring data d, and B would be the presence of signal with parameters $\boldsymbol{\theta}$ in the data. Usually, the waveform with parameters $\boldsymbol{\theta}$ is based on some sort of hypothesis $\mathcal{H}$, for example, the waveform model chosen to simulate the GW signal. Bayes' theorem in the context of GWs takes the form

$$P(\boldsymbol{\theta} \mid d, \mathcal{H}) = \frac{P(d \mid \boldsymbol{\theta}, \mathcal{H})P(\boldsymbol{\theta} \mid \mathcal{H})}{P(d \mid \mathcal{H})}, \tag{3.13}$$

where the following elements are defined as:

1. **Posterior** $P(\boldsymbol{\theta} \mid d, \mathcal{H})$: The probability of signal $h(\boldsymbol{\theta}, t)$ given data $d(t)$.
2. **Likelihood** $P(d \mid \boldsymbol{\theta}, \mathcal{H})$: The probability to observe data $d(t)$ containing signal $h(\boldsymbol{\theta}; t)$ given certain GW parameters $\boldsymbol{\theta}$.
3. **prior** $P(\boldsymbol{\theta} \mid \mathcal{H})$: The probability of parameters $\boldsymbol{\theta}$ for signal $h(\boldsymbol{\theta}; t)$.
4. **evidence** $P(d \mid \mathcal{H})$: The probability of observing data $d(t)$.

The evidence can be seen as a normalization factor given that it is not dependent on $\boldsymbol{\theta}$. It can be computed to set the total posterior distribution equal to one (i.e. $\int d\boldsymbol{\theta} P(\boldsymbol{\theta} \mid d, \mathcal{H}) = 1$).

To find the probability, we exploit a property of the noise. Assume that the noise $\tilde{n}(f)$ at a specific frequency is Gaussian, where the variance is given by $S_n(f)$ at that frequency. With this, we can construct the Gaussian probability distribution of the noise

$$P[n] = \mathcal{N} \exp\left(-2 \int_{-\infty}^{\infty} \frac{|\tilde{n}(f)|^2}{S_n(f)} df\right) = \mathcal{N} e^{-\frac{1}{2}\langle n|n\rangle}, \tag{3.14}$$

with $\mathcal{N}$ a normalization factor [91]. From equation 3.5, we can define noise as $n(t) = d(t) - h(\boldsymbol{\theta}; t)$, which is true under the assumption a signal is present in the data. Therefore, the likelihood is

$$P(d \mid \boldsymbol{\theta}, \mathcal{H}) = P[n] = P[d - h] = \mathcal{N} e^{-\frac{1}{2}\langle d - h(\boldsymbol{\theta}) | d - h(\boldsymbol{\theta})\rangle}. \tag{3.15}$$

One commonly uses the log-likelihood

$$\ln\left(P(d \mid \boldsymbol{\theta}, \mathcal{H})\right) = \ln(\mathcal{N}) - \frac{1}{2}\langle d - h(\boldsymbol{\theta}) \mid d - h(\boldsymbol{\theta})\rangle = C + \langle d \mid h\rangle - \frac{1}{2}\langle h \mid h\rangle, \quad (3.16)$$

where C is a constant.

With PE one seeks to find the parameter probability distributions (posteriors), i.e. evaluating the inner products in the equation 3.16 for the complete parameter space. Because of the high dimensionality, computing the inner products over the entire space is impossible and inefficient, given that for most of the parameter space the probability is next to zero. Therefore, commonly used techniques such as nested sampling and Markov Chain Monte Carlo have been developed to explore the probability space of the parameters efficiently, see [91] and references therein. They yield the posterior $P(\boldsymbol{\theta} \mid d, \mathcal{H})$, calculated with Bayes' theorem. They are probability functions for the individual parameters in $\boldsymbol{\theta}$ that fit the data d the best.

Although these techniques have been very successful, being used in all GW detections so far, computing the posterior of a single signal can take weeks of computational time. Therefore, we use Neural Posterior Estimation (NPE) discussed in chapter 6, which is a machine learning-based approach. This promises significant speedups over conventional methods with similar performance.

3.3.1 Hypothesis Testing

Consider two competing hypotheses $\mathcal{H}_1$ and $\mathcal{H}_2$, for example:

$\mathcal{H}_1$: Signal template $h(\boldsymbol{\theta}_1)$ of a BBH event is modeled to be consistent with GR.

$\mathcal{H}_2$: Signal template $h(\boldsymbol{\theta}_2)$ of a BBH event is modeled to be consistent with another theory.

One wants to know which hypothesis is more likely, given the observed data. This is done via a procedure called hypothesis ranking, where one compares the probabilities for both hypotheses given the data. One can define an *odds ratio* (also known as *likelihood ratio*)

$$O_2^1 \equiv \frac{P(\mathcal{H}_1 \mid d)}{P(\mathcal{H}_2 \mid d)} = \frac{P(d \mid \mathcal{H}_1)P(\mathcal{H}_1)}{P(d \mid \mathcal{H}_1)P(\mathcal{H}_2)}, \quad (3.17)$$

where Bayes' theorem was used in the second step to express the odds ratio in terms of evidence $P(d \mid \mathcal{H})$ and prior probability of the hypothesis $P(\mathcal{H})$. One usually does not have prior knowledge about the hypotheses, so often they are considered equal $P(\mathcal{H}_1) = P(\mathcal{H}_2)$.

To obtain the evidence, one computes the integral over all parameter space, i.e.

$$\int d\boldsymbol{\theta} P(\boldsymbol{\theta} \mid d, \mathcal{H}) P(d \mid \mathcal{H}) = \int d\boldsymbol{\theta} P(d \mid \boldsymbol{\theta}, \mathcal{H}) P(\boldsymbol{\theta} \mid \mathcal{H}) = P(\boldsymbol{\theta} \mid d, \mathcal{H}), \quad (3.18)$$

where we used equation 3.13 and $\int d\boldsymbol{\theta} P(\boldsymbol{\theta} \mid d, \mathcal{H}) = 1$. This gives the odds ratio

$$O_2^1 = \frac{\int d\boldsymbol{\theta}_1 P(d \mid \boldsymbol{\theta}_1, \mathcal{H}_1) P(\boldsymbol{\theta}_1 \mid \mathcal{H}_1)}{\int d\boldsymbol{\theta}_2 P(d \mid \boldsymbol{\theta}_2, \mathcal{H}_2) P(\boldsymbol{\theta}_2 \mid \mathcal{H}_2)}, \quad (3.19)$$

where $\boldsymbol{\theta}_1$ and $\boldsymbol{\theta}_2$ can differ in parameterizations given the models in the different hypotheses. This odds ratio is used to rank hypotheses: If $O_2^1 > 1$ then the data is in favor of $\mathcal{H}_1$, and if $O_2^1 < 1$ they favor $\mathcal{H}_2$. When $O_2^1 \approx 1$ the data is uninformative regarding $\mathcal{H}_1$ and $\mathcal{H}_2$.

Chapter 4

Test of General Relativity

Modeling CBC signals in modified gravity theories is still in its infancy, with alternative waveform models being actively researched on both the analytical [96–99] and numerical [100–103] fronts. Current waveform models used in GW analysis rely on approximation and thus lack certain physical accuracy [104, 105], which is crucial for the precision needed for GR tests. Instead, the strategy for testing GR is introducing deviation parameters on a given waveform model. These tests have not seen any statistically significant deviation for GR so far [10], but there are some caveats. For instance, within GR certain exotic objects exist, such as fuzzballs [106], gravastars [107], boson stars [108], dark matter stars [109], etc, for which waveform models have not been studied extensively. Also, detector noise may lead to unintentional observed deviations from GR [105]. Therefore, effects seen by tests of possible physics beyond GR need to be evaluated carefully.

Generally, one can distinguish three different regimes of deviations in a modified theory of gravity (see [110] for a complete overview):

1. Generation: modeling deviations in the dynamical properties of the source and its radiation. The introduction of additional fields or higher curvature corrections can alter the binary's properties, such as angular momentum, binding energy, and flux [96, 111, 112]. This can be modeled by appropriately altering the inspiral dynamics in the waveform.

2. Polarizations: as seen in section 1.2.2, for a GW only the tensor modes h_+ and $h_\times$ survive. In general, a network of GW detectors can detect six polarizations[1], hence searching for evidence of the other modes is also an effective way to probe GR violations.

3. Propagation: GWs can also differ from GR in the way they traverse space. Phenomena like amplitude damping [113], birefringence [114], and dispersion [14] of GWs can be different in modified gravity. A subset of these theories for modified propagation are often called Lorentz invariant violations (LIV) because they break the Lorentz invariant nature of GWs in GR.

In this chapter, we discuss a modification of GW propagation with a Modified Dispersion Relation (MDR). We derive the necessary theoretical tools to understand how to modify GW waveforms and explore the tests of GR already conducted in this area of research.

4.1 Modified Dispersion Relation

In general, a dispersion relation describes the effect of the interaction between a wave and the medium it travels in. It relates the frequency ω to the wavenumber

[1] Any metric theory allows for 6 modes, certain gauges eliminate them, see chapter 7.2 from [3]

k, resulting in different wave propagation velocities, depending on its frequency. To understand dispersion relations, we start with the wave-equation (1.24) for GWs in a vacuum. Filling in the general solution for $h_{\mu\nu} = H_{\mu\nu}e^{i(\vec{k}\cdot\vec{r}-\omega t)}$ yields

$$\omega_{GW}^2 = c^2k^2, \tag{4.1}$$

which is the dispersion relation for GWs in GR. However, these waves are *dispersionless*, meaning that the wave speed is independent on ω and k, and travel at constant speed c.

This velocity is called *phase velocity* v_p to distinguish it from the *group velocity* v_g which we will define below. It is the temporal change of a point at a fixed phase of the wave,

$$\begin{aligned} kz - \omega t &= \text{Constant} \\ d\frac{(kz-\omega t)}{dt} = 0 \rightarrow \frac{dz}{dt} &= \frac{\omega}{k} \\ v_p &= \frac{\omega}{k}, \end{aligned} \tag{4.2}$$

which in the case of this example is constant. A wave is dispersive if the phase velocity is not constant, i.e. if $\omega(k)$ is not a linear function of k.

So far we have looked at propagating waves with a single frequency ω. However, we have seen that a GW source produces a wave, with a frequency spectrum. Now imagine we have a dispersive system so that a wave packet consists of different frequencies traveling at different speeds. This packet, or group of waves, can have a well-defined shape and thus one can track its propagation speed. It turns out that this velocity is related to the slope of $\omega(k)$ through

$$v_g = \frac{d\omega(k)}{dk}, \tag{4.3}$$

which is called the *group velocity*, see chapter 6.3 of [115] for derivations. As the wave propagates, the differing speeds of the components of this group will spread out over the propagation direction. In other words, it will disperse. Hence the name dispersion.

In this thesis, we will consider a Modified Dispersion Relation (MDR) of a gravitational wave. In the literature, the dispersion relation is often noted in terms of energy-momentum instead of frequency-wavenumber. This has its origins in quantum mechanics as the first theories of MDR involved theories of massive graviton [14]. From particle physics, we know particles are associated with waves, where energy and momentum are quantized to frequency and wavenumber via the Planck constant. So,

$$E = \hbar\omega \qquad \text{and} \qquad p = \hbar k, \tag{4.4}$$

where substituting these in equation 4.1 gives dispersion relation

$$E^2 = p^2c^2. \tag{4.5}$$

Now, we can use the particle-wave duality in quantum mechanics to derive yet another velocity, namely the *particle velocity*. Imagine a massive particle going through flat space-time with $E = \gamma mc^2$ and $p = \gamma m v_{\text{par}}$, where γ is the Lorentz factor. Then, the particle velocity is

$$v_{\text{par}} = c^2\frac{p}{E}, \tag{4.6}$$

where we assume that this still holds in curved geometries given that $P^\mu P_\mu (= -m^2c^2)$ should be an invariant quantity.

When looking for MDR, we consider a generalized relation due to an additional term in the dispersion relation,

$$E^2 = p^2c^2 + A_\alpha (pc)^\alpha, \tag{4.7}$$

where A_α and α are phenomenological parameters, and find their origin in different non-GR theories dependent on the choice of α.

4.1.1 Friedmann-Lemaître-Robertson-Walker metric

So far we have considered GWs traversing through a vacuum. However, we know that our Universe is not as static. Therefore, We have to consider GR on cosmological scales. Here we will derive the metric description with the following assumption. If we average on large scales, our universe is *homogeneous* (the same at every place) and *isotropic* (the same in all directions). This is considered the standard model of cosmology and is mainly supported by observations from the Cosmic Microwave Background (CMB) [116] and galaxy distribution [117].

The Friedmann–Lemaître–Robertson–Walker (FLRW) metric describes a homogeneous, isotropic, and expanding universe. The four-dimensional line element takes the form

$$ds^2 = -dt^2 + a(t)^2 \gamma_{ij} dx^i dx^j, \tag{4.8}$$

where $a(t)$ is the scale factor, which describes the expansion of the universe. It is important to note that we have no spatial-time elements (g^{0i}) because of isotropy. γ_{ij} defines the spatial metric yet to be defined. For homogeneity and isotropy to hold everywhere, we must have constant intrinsic spatial curvature. This leads to three possibilities: flat, spherical, and hyperbolic curvatures, the derivation of which can be found in [16]. Accounting for this in equation 4.8, the line element becomes

$$ds^2 = -dt^2 + a^2(t)[\frac{dr^2}{1 - Kr^2} + r^2 d\Omega^2], \tag{4.9}$$

where we have expressed the spatial coordinates in spherical coordinates. K encodes the curvature and is either zero, positive, or negative depending on flat, spherical, or hyperbolic curvature.

With the metric obtained, we now want to determine how the line element evolves. Therefore we need to study the scale factor $a(t)$, with commonly used definitions

$$H(t) \equiv \frac{\dot{a}(t)}{a(t)}, \qquad 1 + z(t) \equiv \frac{a(t_0)}{a(t)}, \qquad a(t_0) \equiv 1, \tag{4.10}$$

where the index $t = t_0$ indicates today's value. $H(t)$ is the Hubble constant ($H(t_0) = H_0 \approx 70$ km/s/Mpc being approximately today's value[2] [119]), and $z(t)$ is cosmological redshift. Using these definitions, we can start by solving the Einstein equations for this metric for a *perfect fluid*,

$$G_{\mu\nu} = 8\pi T_{\mu\nu}, \qquad \text{where} \qquad T_{\mu\nu} = (\rho(t) + P(t))U_\mu U_\nu + P(t) g_{\mu\nu}, \tag{4.11}$$

[2]The Hubble Constant has two main measurements: one based on cosmic microwave background radiation suggesting about 67 km/s/Mpc, and the other involving direct observation of nearby galaxies suggesting about 73.8 km/s/Mpc. This discrepancy is known as the Hubble tension [118].

where ρ and P are energy density and momentum respectively and U_μ the four-velocity. Here we used the conventional to absorb the cosmological constant term into the energy-momentum tensor [3].

For the derivation of $G_{\mu\nu}$, one needs to calculate the Ricci tensor and scalar in the FLRW metric, which can be found [16]. This results in

$$G_{00} = 3\Big[\Big(\frac{\dot{a}(t)}{a(t)}\Big)^2 + \frac{K}{a(t)^2}\Big] \qquad \text{and} \qquad G_{ij} = -\Big[2\frac{\ddot{a}(t)}{a(t)} + \Big(\frac{\dot{a}(t)}{a(t)}\Big)^2 + \frac{K}{a(t)^2}\Big]g_{ij}, \tag{4.12}$$

where if we plug the equations into the Einstein field equations we get

$$\Big(\frac{\dot{a}(t)}{a(t)}\Big)^2 = \frac{8\pi}{3}\rho(t) - \frac{K}{a(t)^2} \qquad \text{and} \qquad \frac{\ddot{a}(t)}{a(t)} = -\frac{4\pi}{3}(\rho(t) + 3P(t)), \tag{4.13}$$

the Friedmann and Raychaudhuri equations for the temporal and spatial parts respectively.

Since we are considering a perfect fluid, we can derive a continuity equation for the evolution of matter in this metric. Considering energy conservation $\nabla_\mu T^{\mu\nu} = 0$ in the rest-frame yields

$$\dot{\rho}(t) = -3\frac{\dot{a}(t)}{a(t)}(\rho(t) + P(t)), \tag{4.14}$$

with the assumption of a constant equation of state, $P(t)/\rho(t) = \text{constant}$[4], with solution

$$\rho(t) = \rho(t_0)a(t)^{3(1+P(t)/\rho(t))}. \tag{4.15}$$

With this, we can calculate the critical density today $\rho_{crit}(t_0) = \frac{3H_0^2c^4}{8\pi G} \approx 1.3 \times 10^{11} M_\odot Mpc^{-3}$. We now present the Friedman equation 4.13 weighted by the value it takes at $t = t_0$,

$$\frac{H(t)^2}{H(t_0)^2} = \Omega_r a(t)^{-4} + \Omega_M a(t)^{-3} + \Omega_K a(t)^{-2} + \Omega_\Lambda \tag{4.16}$$

with $\Omega_i \equiv \rho_i/\rho_{crit}$, dimensionless constants relating the different 'densities' for $i = r, M, K, \Lambda$ for radiation, matter, curvature, and dark energy respectively. The measured cosmological parameters are: $\Omega_r \approx \times 10^{-4}, \Omega_M \approx 0.32, \Omega_\Lambda \approx 0.68$, and $|\Omega_K| < 0.005$ [120]. We commonly approximate to flat spacetime $K = 0$ and radiationless $\Omega_r \approx 0$ so that

$$\frac{H(t)^2}{H(t_0)^2} = \Omega_M a(t)^{-3} + \Omega_\Lambda \Rightarrow \frac{H(t)}{H_0} = \sqrt{\Omega_M(1 + z(t))^3 + \Omega_\Lambda}. \tag{4.17}$$

With the foundations derived, we now look at the implications this has on GWs. Consider the GW emitted in frame $t = t_{em}$ and observed in frame $t = t_{obs}(= t_0)$. A non-dispersive GW propagating in the radial direction in flat space-time would have a $ds^2 = 0$, giving $dt^2 = a(t)^2 dr^2$, such that

$$dt_{em}^2 = a(t_{em})^2 dr^2 \qquad \text{and} \qquad dt_{obs}^2 = a(t_{osb})^2 dr^2. \tag{4.18}$$

[3] Where the energy and momentum are redefined as $T_{\mu\nu} - \frac{\Lambda}{8\pi}g_{\mu\nu} \equiv T_{\mu\nu}, \rho + \frac{\Lambda}{8\pi} \equiv \rho$ and $P - \frac{\Lambda}{8\pi} \equiv P$.

[4] $P(t)/\rho(t)$ depend on the fluid considered, where the values are 0 for matter, $\frac{1}{3}$ for radiation, and -1 for dark energy.

When combined those we find

$$dt_{obs} = \frac{a(t_{osb})}{a(t_{em})} dt_{em} = (1 + z(t_{em}))dt_{em}. \tag{4.19}$$

This means that frequency $\omega_{GW}[\frac{1}{\text{time}}]$ and energy $E = \hbar\omega$ are also redshifted,

$$\omega_{obs} = \frac{\omega_{em}}{1 + z(t_{em})} \qquad \text{and} \qquad E_{obs} = \frac{E_{em}}{1 + z(t_{em})}. \tag{4.20}$$

As a consequence, the luminosity $\mathcal{L} = \frac{dE}{dt}$ and flux $\mathcal{F} = \frac{\mathcal{L}}{4\pi r^2}$ change as,

$$\mathcal{L}_{obs} = \frac{1}{(1 + z(t_{em}))^2} \mathcal{L}_{em} \qquad \text{end} \qquad \mathcal{F}_{obs} = \frac{1}{(1 + z(t_{em}))^2} \frac{\mathcal{L}_{em}}{4\pi r^2}. \tag{4.21}$$

From this, we define the *luminosity distance* D_L, which will replace the distance r of an observed GW,

$$D_L = (1 + z(t_{em}))r = (1 + z(t_{em})) \int_{t_{em}}^{t_{obs}} \frac{cdt}{a(t)} = c(1 + z(t_{em})) \int_{z(t_{obs})}^{z(t_{em})} \frac{dz}{H(z)}. \tag{4.22}$$

Using equation 4.17 and implying the t dependency in z, the luminosity distance takes the form

$$D_L(z) = \frac{c(1 + z)}{H_0} \int_0^z \frac{dz'}{\sqrt{\Omega_M(1 + z')^3 + \Omega_\Lambda}}. \tag{4.23}$$

One can extend this for the chirp mass $\mathcal{M}_c$, by plugging in the luminosity distance and GW redshifted frequency in the formula of $h(\omega)$ we find:

$$\mathcal{M}_c \quad \rightarrow \quad \mathcal{M}_c^z = (1 + z)\mathcal{M}_c. \tag{4.24}$$

Note that total mass $M \rightarrow M^z = (1 + z)M$ and thus component masses $m_i \rightarrow m_i^z = (1 + z)m_i$ scale the same. This means that the GW parameters absorb all z dependence; thus, redshift is not directly observable from the GW signal alone. To obtain the redshift of a GW, one needs to inversely determine it from the measured luminosity distance, using constants of cosmology from other measurements.

With this metric derived, we now have a canvas on which we can study modified dispersion relations of GWs on cosmological scales.

4.1.2 Wentzel–Kramers–Brillouin approach

The Wentzel–Kramers–Brillouin (WKB) method is a mathematical technique for obtaining approximate solutions to linear differential equations with spatially or temporally varying coefficients. This approach can be used to create an analytical framework for studying GWs and has been developed in [121, 122] However, this approach is more general. In this thesis, we will follow the derivation in [123].

The WKB method works as follows. Given a differential equation

$$\epsilon \frac{d^N y(x)}{dx^N} + \sum_{n=1}^{N-1} a_n(x) \frac{d^n y(x)}{dx^n} = 0, \tag{4.25}$$

with ϵ a small parameter and $a_n(x)$ an arbitrary function defining the differential equation. The WKB method solves the differential equation via the ansatz

$$y(x) = \exp\Big[\frac{1}{\delta}\sum_{n=0}^{\infty}\delta^n b_n(x)\Big], \tag{4.26}$$

where $b_n(x)$ is to be determined by taking the limit for $\delta \to 0$ and solving for increasing order in ϵ/δ^n. The solution obtained with the WKB approach is valid provided that parameter ϵ is small. In the case of GWs, we study the evolution of a second-order differential equation of a time-dependent function $h(t)$, or inversely frequency $h(\omega)$. Here, we study modifications on cosmological timescales of order $\frac{1}{H(z)}$. In this case, $\omega_{GW} >> H_0$, meaning the GW parameters' time variation is much smaller than the waves' frequency, making this a good approximation.

In [122], the authors derive the WKB approximation in terms of wavenumber $h(k)$ at the time of emission and detection. Their dispersion relation reads

$$\omega = ck + \Delta\omega, \tag{4.27}$$

where $\Delta\omega$ encapsulated the modification from the normal dispersion relation.

For a GW emitted at redshift z_{em}, the phase shift takes the form [123]

$$h_{MDR}(\omega) = h_{GR}(\omega)e^{-i\int_0^{z_{em}}\Delta\omega/H(z)dz} = h_{GR}(\omega)e^{i\Delta\Psi(\omega)}, \tag{4.28}$$

where h_{GR} is the GW predicted by GR and h_{MDR} the MDR corrected waveform. $\Delta\Psi$ is the overall phase shift caused by the GR modification.

To find an expression for $\Delta\Psi$ one can start from equation 4.7 and derive $\Delta\omega$

$$\omega^2 = c^2k^2\Big[1 + A_\alpha\Big(\frac{\hbar ck}{a(z)}\Big)^{\alpha-2}\Big], \tag{4.29}$$

where using equation 4.27 gives

$$\Delta\omega \approx \omega\frac{A_\alpha}{2}\Big(\frac{\hbar ck}{a(z)}\Big)^{\alpha-2} \approx \frac{A_\alpha\hbar^{\alpha-2}\omega^{\alpha-1}}{2}(1+z)^{\alpha-2}. \tag{4.30}$$

Here we assume that $A_\alpha << 1$, which is supported by measurements [10]. This gets us to a simple expression for the phase shift

$$\Delta\Psi(\omega) \approx -\frac{A_\alpha\hbar^{\alpha-2}\omega^{\alpha-1}}{2}\int_0^{z_{em}}\frac{(1+z)^{\alpha-2}}{H(z)}dz. \tag{4.31}$$

It is then conventional to define an effective distance similar to equation 4.23,

$$D_\alpha(z) = \frac{c(1+z)^{1-\alpha}}{H_0}\int_0^z\frac{(1+z')^{\alpha-2}dz'}{\sqrt{\Omega_M(1+z')^3+\Omega_\Lambda}}, \tag{4.32}$$

so that we end up with

$$\Delta\Psi(\omega) \approx -\frac{A_\alpha\hbar^{\alpha-2}[\omega(1+z_{em})]^{\alpha-1}}{2c}D_\alpha(z_{em}). \tag{4.33}$$

Note that A_α and D_α are dimensionful parameters but $\Delta\Psi$ needs to be dimensionless. D_α always has dimension distance, while the dimension of A_α depend on the chosen

alpha ([energy]$^{2-\alpha}$).

The $\Delta\Psi$ phase modification is only due to propagation and thus does not depend on the source's characteristics, meaning this holds for any GW. Observe that phase shift $\Delta\Psi$ is defined for a given redshift. However, as we have seen for the FLRW metric, this redshift is absorbed in the parameters of the GW and thus not a direct observable. To more directly observe MDR effects, one has to study the effects on the arrival phase and the relative time delays between frequency components of the CBC waveform.

4.1.3 Stationary Phase Approximation

Relating the arrival phase of a binary inspiral waveform to the phase shift $\Delta\Psi$ can be done via the Stationary Phase Approximation (SPA). It is common to do GW data analysis in a frequency-domain (i.e., Fourier domain) representation, as an alternative to the time-domain waveform. The SPA provides a good way to go from time to frequency domain [26]. Assume the general form of the waveform is

$$h(t) = \sum_j A_j(t) e^{-i\phi_j(t)}, \tag{4.34}$$

where A_j and ϕ_j are the amplitude and phase for the j^{th} emission mode in the CBC waveform. In this thesis, we study waveforms generated by quadrupole radiation (the $j = 22$ mode). Here we describe the SPA under arbitrary emission modes as derived in [123].

The Fourier transform takes the form

$$\tilde{h}(\omega) = \sum_j \int A_j(t) e^{i\omega t - \phi_j(t)} dt. \tag{4.35}$$

The SPA is applicable if the waveforms' amplitude evolution is slower than that of the phase. This can be done on a mode-by-mode basis,

$$\frac{d\ln(A_j(t))}{dt} = \frac{1}{A_j(t)} \frac{dA_j(t)}{dt} << \frac{d\phi_j(t)}{dt}. \tag{4.36}$$

In general, this is a good approximation for binary inspiral formulated in GR, see [124]. Given that we assume only a GR modification in the propagation and not in the generation, this approximation still holds.

Before solving equation 4.35 using SPA, it is good to study the phase $\phi_j(t)$ in more detail,

$$\phi_j(t) = 2\pi \int_{t_{j,c}}^{t} F_j(t')dt' + \phi_{j,c} = 2\pi F_{j,c}(t) + \phi_{j,c}, \tag{4.37}$$

where $t_{j,c}$ is the time of arrival of the different coalescence frequencies $F_{j,c}(t)$, where we take into account that there is a time difference between different modes. $\phi_{j,c}$ is the phase at the arrival time, all measured in the detector frame. These coalescence frequencies emitted simultaneously do not necessarily arrive at the same time if we have different propagation velocities due to an MDR. These different arrival times are characterized by $t_{j,c}$.

Under SPA, the solution of the Fourier transform becomes

$$\tilde{h}(\omega) = \sum_j \frac{A_j(t_j)}{2\sqrt{2\pi}\sqrt{\frac{dF_j(t_j)}{dt}}} e^{i\Psi_j(\omega)} dt, \qquad \text{where} \qquad \Psi_j(\omega) = \omega t_j - \phi_j(t_j) - \pi/4. \tag{4.38}$$

t_j is derived from finding the arrival time of a point in the phase by setting $d\phi/dt \equiv \omega$, i.e.

$$\frac{d\phi_j(t)}{dt}\Big|_{t=t_j} = 2\pi F_j(t_j) \equiv \omega. \tag{4.39}$$

Note that by solving this, t_j becomes frequency-dependent $t_j(\omega)$.

$\Psi_j(\omega)$ is the frequency-domain phase, with analogous role as $\Delta\Psi$ in the WKB approach from the previous section. To find the connection, first combine equations 4.37 and 4.38 yielding:

$$\Psi_j(\omega) = \omega t_{j,c} - \int_{\omega_{j,c}}^{\omega} (t_j(\omega') - t_{j,c}) d\omega' - \phi_{j,c} - \pi/4, \tag{4.40}$$

where the integral is the shift in phase corresponding to the time delay between the different frequency modes compared to the coalescence time. This approximation is still within GR, where $\phi_j(t)$ will not change over time.

If there is a modified propagation of GWs, the coalescence phase at arrival $\phi_{j,c}$ can be different from the coalescence phase at emission. This happens if the phase velocity differs from the propagation velocity. Also, since an MDR during propagation changes the arrival time of different frequencies, the frequency-time evolution is modified in the detector frame concerning the relation at the emission frame, thus resulting in a different time ordering of frequencies detected than expected from the source. This departure from GR in both the coalescence phase and the change in arrival time can be encompassed in the overall frequency-domain shift $\Delta\Psi(\omega)$, giving

$$\Psi_j(\omega) = \Psi_j^{GR}(\omega) + \Delta\Psi(\omega). \tag{4.41}$$

4.1.4 Particle, Phase, and Group Velocities

The velocity at which a GW propagates is crucial in determining the travel time of different frequency components. In this section, we will discuss the main points explained by the authors in [123]. There are three different types of velocities to calculating the arrival phase under the SPA:

1. Particle velocity:
   A common approach in the literature [125, 126], which associates the particle velocity to the arrival time.

2. Phase velocity:
   The speed of the phase of a given frequency is used to calculate the frequency-domain phase shift. It is related to the particle velocity.

3. Group velocity:
   Here the speed is associated with the arrival of a given frequency in the *wavepacket*. The speed of the packet is described by the group velocity [123].

In this section, we derive the frequency-domain phase Ψ within the SPA, equation 4.40, using the different velocity approaches. We compare and connect them, motivating the use of the group velocity in our approach, making similar arguments as in [123].

Until recently, the commonly used approach for deriving $\Delta\Psi$ caused by MDR was using particle velocity. This particle is thought of as a massive graviton, carrying the gravitational force, but one can extend this approach to higher orders in α. In this interpretation, we assume that the momenta in equation 4.7 are associated with the propagation speed of a massive particle. Using equation 4.6, we derive that the linear order of A_α the particle velocity is

$$v_{\text{par}} \approx c - \frac{1}{2} A_\alpha c (\hbar\omega)^{\alpha-2}. \tag{4.42}$$

The phase velocity of a GW is given by ω/k, see equation 4.2. Combining this with the dispersion relation (4.29), we can also approximate the phase velocity in the linear order of A_α, giving

$$v_p \approx c + \frac{1}{2} A_\alpha c (\hbar\omega)^{\alpha-2}. \tag{4.43}$$

Notice that the particle and phase velocity are equivalent to each other with a difference in sign of A_α, meaning that both interpretations of propagation under this version of MDR are indistinguishable.

For the group velocity, we take the derivative $d\omega/dk$, see equation 4.3. Computing the derivative and combining terms to linear order in A_α gives

$$v_g \approx c - \frac{1}{2}(1-\alpha) A_\alpha c (\hbar\omega)^{\alpha-2}. \tag{4.44}$$

The next step in obtaining the frequency-domain phase for the different velocities is calculating the time delay between each frequency mode. For that, let us take two different frequencies $\omega^{(1)}$ and $\omega^{(2)}$ evaluated in the source frame. This is done by equating the propagated distance of the two frequencies together, which is valid under the assumption that the time differences are small with respect to the total travel time. The propagated distance is obtained by integrating over time, giving

$$r = \int_{t_{em}}^{t} v(\omega^{(1)}, t') \frac{dt'}{a(t')} = \int_{t_{em}-\Delta t_{em}}^{t-\Delta t} v(\omega^{(2)}, t') \frac{dt'}{a(t')}, \tag{4.45}$$

where Δt is our measured time delay of interest and Δt_{em} is the time delay between the two frequencies in the emission frame. We can assume that these time delays are small compared to the Hubble time, meaning that the last integral becomes

$$\int_{t_e-\Delta t_{em}}^{t-\Delta t} v(\omega^{(2)}, t') \frac{dt'}{a(t')} = \int_{t_{em}}^{t} v(\omega^{(2)}, t') \frac{dt'}{a(t')} + v(\omega^{(2)}, t)\Delta t - v(\omega^{(2)}, t_{em})\Delta t_{em}. \tag{4.46}$$

Lastly, we consider the product of small terms $\Delta t A_\alpha$ to be negligible, resulting in the time difference

$$\Delta t \simeq (1+z_{em})\left(\Delta t_{em} - \frac{1}{1+z_{em}} \int_{t_e}^{t} \frac{v(\omega^{(1)}, t') - v(\omega^{(2)}, t')}{c} \frac{dt'}{a(t')}\right), \tag{4.47}$$

where z_{em} is the redshift to the emission frame. Filling in the respective velocities and computing the integral gives us time delays of phase and group velocity

$$\begin{aligned}\Delta t_p =&(1+z_{em})\Big(\Delta t_{em} - \frac{A_\alpha}{2c} D_\alpha \Big(\frac{1}{(\hbar\omega^{(1)})^{2-\alpha}} - \frac{1}{(\hbar\omega^{(2)})^{2-\alpha}}\Big)\Big),\\ \Delta t_g =&(1+z_{em})\Big(\Delta t_{em} - \frac{(1-\alpha)A_\alpha}{2c} D_\alpha \Big(\frac{1}{(\hbar\omega^{(1)})^{2-\alpha}} - \frac{1}{(\hbar\omega^{(2)})^{2-\alpha}}\Big)\Big).\end{aligned} \tag{4.48}$$

For the last step, we need to compute Ψ_j as defined in equation 4.40, but re-express it in terms already derived above

$$\Psi_j(\omega) = \omega t_{j,c} - \int_{\omega_{j,c}}^{\omega} \Delta t_{j,c} d\omega' - \phi_{j,c} - \pi/4, \tag{4.49}$$

where $\Delta t_{j,c}$ is now the time delay for the j^{th} mode with respect to the coalescence time. Given that our velocities in question are not mode-dependent, from now on we will drop the index j, where every computed phase shift will hold for every mode. Furthermore, the time delay of equation 4.47 was computed between two arbitrary frequencies, but in the SPA we had taken the coalescence frequency as a reference, thus taking $\omega^{(2)}$ as ω_c and $\omega^{(1)}$ as ω. This means that we now can find $\Delta\Psi$, combining equations 4.41 and 4.49, with Ψ^{GR} have no modification, where every term is the same as emitted

$$\Psi^{GR}(\omega) = -\int_{\omega_c}^{\omega} \Delta t_{em,c} d\omega' - \phi_{em,c} - \pi/4. \tag{4.50}$$

For the computation of the integral and other terms in Ψ we refer to [123], here we will only look at the results. For the particle/phase velocity, the resulting $\Delta\Psi$ takes the form

$$\Delta\Psi(\omega) = \begin{cases} -\frac{A_\alpha}{2c\hbar(1-\alpha)} D_\alpha \Big(\frac{1}{(\hbar(1+z_{em})\omega)}\Big)^{1-\alpha} & \alpha \neq 1 \\ \frac{A_1}{2c\hbar} D_1 \ln\Big(\frac{\omega}{\omega_0}\Big) & \alpha = 1 \end{cases}, \tag{4.51}$$

where we had to split the equation at $\alpha = 1$ due to a divergence in the general solution. The normalization frequency ω_0 in the case of $\alpha = 1$ is defined where $\phi(\omega_0/e) = \phi_{em}(\omega_0/e)$, where e is Euler's number. In other words, the frequency at which the phase ϕ is the same as what GR would predict. Unfortunately, this constraint is not enough to know ω_0 beforehand, one has to put extra constraints on the MDR, usually from particle physics [126]. It is conventional to relate the frequency to the chirp mass $e/\omega_0 = 2G\mathcal{M}_c/c^3$.

For the group velocity, the frequency-domain phase shift takes the form

$$\Delta\Psi(\omega) = -\frac{A_\alpha}{2c\hbar} D_\alpha \Big(\frac{1}{(\hbar(1+z_{em})\omega)}\Big)^{1-\alpha}. \tag{4.52}$$

Observe that with some rewriting this is exactly the same expression as equation 4.33. This shows that under SPA, the group velocity-derived phase shift is the same as in the WKB approximation. Note that we do not have a divergency at $\alpha \to 1$, instead at $\alpha = 1$ there is no frequency-dependent MDR contribution in the leading order of A_α.

Notice that at $\alpha = 0$, both approaches yield the same phase shift. This corresponds to the massive graviton, mostly studied in previous work, [125, 126]. However, the group velocity approach naturally leads to the WKB approach. In [123], they compared both the group and particle velocity approaches and demonstrated how to translate constraints between both approaches for GWs with multiple frequency modes. The inclusion of higher-order modes yields a more accurate description of the waveform and thus these waveforms are appealing for TGR. Given that WKB formalism is the relevant approach for higher-order modes, the group velocity interpretation is a sensible choice for studying MDR.

4.1.5 Final Waveform

To construct the waveform used in this thesis, we used a frequency-domain model. To simplify the MDR correction, we define an effective parameter A_{eff} that encompasses together with α all of the GR modification

$$A_{eff}(z) = \frac{D_\alpha(z)}{D_L(z)}(1+z)^{\alpha-1}A_\alpha. \tag{4.53}$$

This can be determined by obtaining the redshift with the measured luminosity distance. Note that for this calculation we assume a flat, matter-energy dominant FLRW metric for the distances as defined above in equations 4.23 and 4.32.

Now we can formulate the frequency-dependent phase as

$$\Delta\Psi(f) = -\frac{\pi D_L h^{\alpha-2}}{c}A_{eff}f^{\alpha-1}, \tag{4.54}$$

where we used that $\hbar\omega = hf$, with h the plank constant. So, our final waveform becomes

$$h^{MDR}(f) = h^{GR}(f)e^{i\Delta\Psi(f)}. \tag{4.55}$$

4.2 Constraints found in the Literature

Binary Neutron Star (BNS) mergers are one of the most direct probes we have for observing the propagation speed of GWs. On the 17th of August 2017, the Advanced LIGO and Virgo detectors observed such an event, GW170817 [8, 127]. Near simultaneously, a Gamma-Ray Burst (GRB), GRB 170817A was observed at the Fermi Gamma-ray Burst Space Telescope [128] as well as an Anti-Coincidence Shield for the Spectrometer for the International Gamma-Ray Astrophysics Laboratory [129]. This combined direct measurements of gravitational and electromagnetic radiation for the first time. With some conservative assumptions on both the emission time difference between the electromagnetic and the GW and the travel distance from the source made in [130], we can put a lower and upper bound on the propagation speed v_{GW} of GWs, compared to the speed of light

$$-3\times10^{-15} \leqslant \frac{v_{GW}-c}{c} \leqslant 7\times10^{-16}. \tag{4.56}$$

This is our first indication that our modification to GR in which $v_{GW} = c$ has to be orders of magnitude smaller compared to the speed of light, meaning that parameter A_α, which determines the scale of the deviation in propagation speed is small.

To constrain the order and values for A_α at different α, one has to test different MDR waveforms against observed GWs. The most recent study is done with GWTC-3 [10], in which the authors perform a suite of GR tests using CBC signals observed up to the end of the third observing run. This thesis will only focus on their results regarding MDR corrections in propagation.

In [10], the MDR test is done on 12 events on top of the 31 events from previous results from GTWC-1 [131] and GWTC-2 [132], making a total of 43 events. Two events are identified to be problematic, GW200219D and GW200225B. They have the lowest residual SNR and are found to have the strongest impact on biasing the combined posteriors. These events require detailed analysis to understand the reasons for the observed deviations, which is yet to be studied. Thus, their analysis is performed both including and excluding these events.

Their analysis considers MDR using the particle velocity as defined above (eq. 4.51) and uses waveform model IMRPHENOMXHM [133]. They perform discrete steps in parameter α of 0.5, excluding $\alpha = 2$, given that the propagation speed modification is frequency independent for this value. Figure 4.1 shows violin plots representing the posterior probability of A_α, where the redshift is obtained from the luminosity distance [10]. Figure 4.2 shows the upper and lower bounds of the $< 90\%$ credible interval for A_α. A combination and comparison of the bounds found for GWTC-1, GWTC-2, and GWTC-3 are given in table 4.1. $Q_{\rm GR} = P(A_\alpha < 0)$ which gives the probability to have $A_\alpha < 0$, where $A_\alpha = 0$ is the GR value. Thus, large or small values of the GR quantile indicate that the distribution is not peaked close to the GR value, with a $Q_{\rm GR} = 50\%$ implying the distribution is centered on the GR value.

One can focus on the $\alpha = 0$ result to predict the graviton mass, where $A_0 = m_g^2 c^2$. This gives us the 90% credible upper bound of $m_g \leq 1.27 \times 10^{-23}$ eV/c^2 [10].

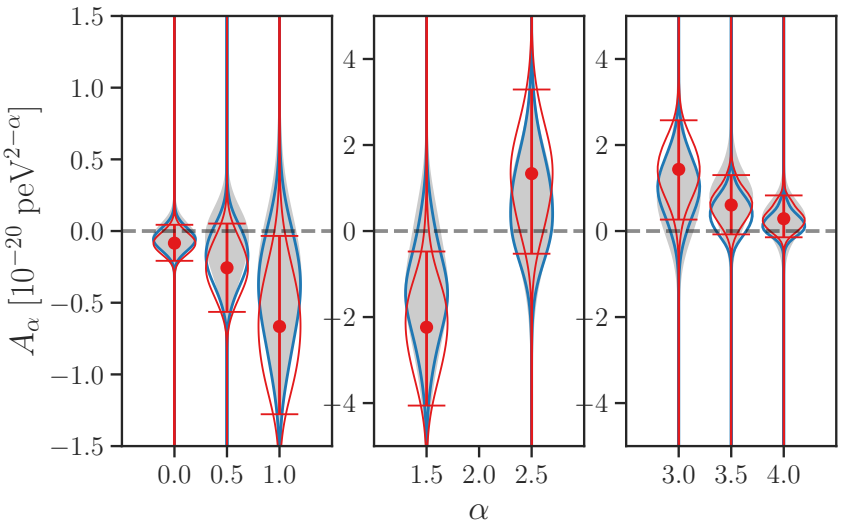

FIGURE 4.1: Results from [10]. The red violin plots show the combined posteriors of the parameter A_α calculated from the GWTC-3 events with the error bars denoting the 90% credible intervals. Blue violins are the combined posteriors after excluding GW200219D and GW200225B. The gray plots in the background are the combined posteriors corresponding to GWTC-2 [132].

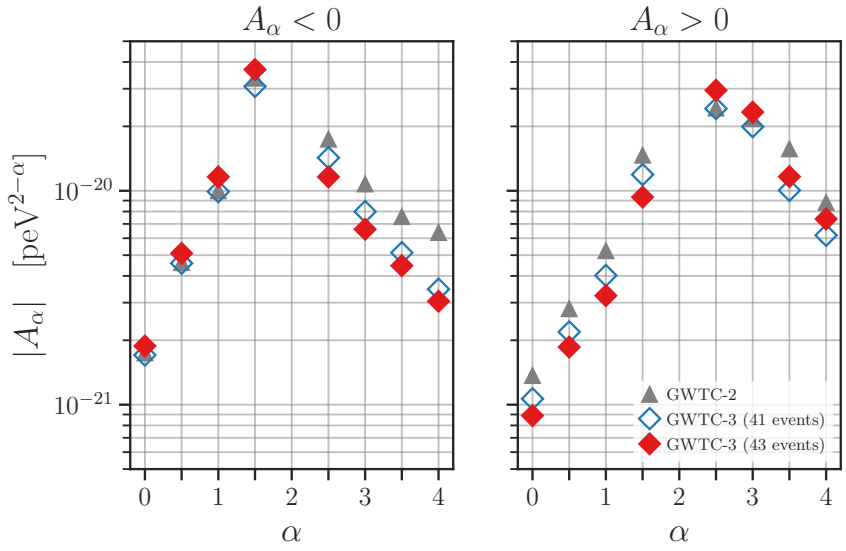

FIGURE 4.2: Result from [10]. The scatter plot of 90% credible upper bounds on the modulus of deviation parameters A_α. The one-sided bounds are computed for positive and negative values of the parameters separately. Filled (open) diamond markers represent the GWTC-3 bounds including (excluding) GW200219D and GW200225B. The gray markers in the background denoted the numbers obtained from GWTC-2 [132].

	m_g	$\lvert\bar{A}_0\rvert$			$\lvert\bar{A}_{0.5}\rvert$			$\lvert\bar{A}_1\rvert$			$\lvert\bar{A}_{1.5}\rvert$			$\lvert\bar{A}_{2.5}\rvert$			$\lvert\bar{A}_3\rvert$			$\lvert\bar{A}_{3.5}\rvert$			$\lvert\bar{A}_4\rvert$		
	$[10^{-23}$ eV$/c^2]$	$<$ $[10^{-45}]$	$>$	Q_{GR} [%]	$<$ $[10^{-38}]$	$>$	Q_{GR} [%]	$<$ $[10^{-32}]$	$>$	Q_{GR} [%]	$<$ $[10^{-26}]$	$>$	Q_{GR} [%]	$<$ $[10^{-14}]$	$>$	Q_{GR} [%]	$<$ $[10^{-8}]$	$>$	Q_{GR} [%]	$<$ $[10^{-2}]$	$>$	Q_{GR} [%]	$<$ $[10^{4}]$	$>$	Q_{GR} [%]
GWTC-1	4.70	7.99	3.39	79	1.17	0.70	73	2.51	1.21	70	6.96	3.70	86	5.05	8.01	28	2.94	3.66	25	2.01	3.73	35	1.44	2.34	34
GWTC-2	1.76	1.75	1.37	66	0.46	0.28	66	1.00	0.52	79	3.35	1.47	83	1.74	2.43	31	1.08	2.17	17	0.76	1.57	12	0.64	0.88	25
GWTC-3	1.27	1.88	0.89	86	0.51	0.19	91	1.16	0.32	96	3.69	0.93	98	1.16	2.95	13	0.66	2.33	2	0.45	1.16	7	0.30	0.74	15

TABLE 4.1: Results for the modified dispersion analysis of GWTC-1 [131], GWTC-2 [132] and GWTC-3 [10]. The table shows 90%-credible upper bounds on the graviton mass m_g and the absolute value of the dimensionless phenomenological parameter $\bar{A}_\alpha = A_\alpha / \mathrm{eV}^{2-\alpha}$. The $<$ and $>$ labels denote the bounds on $|\bar{A}_\alpha|$ for $A_\alpha > 0$ and $A_\alpha < 0$ respectively.

Part II

Machine Learning

Chapter 5

Neural Networks

In this work, we have developed a Machine Learning (ML) method, capable of testing an MDR for GW. The use of an ML-based approach is justified by its enormous speedups over conventional methods. Due to the small effect expected for MDR, one has to perform PE on a large number of signals to get any meaningful information. Using conventional methods, described in section 3.3, will take a large amount of computational time, which is why we use an ML-based method, described in chapter 6. To understand this method, one first has to understand one of its fundamental components, a Neural Network (NN).

NNs form the basis of Artificial Intelligence (AI), a field that has exploded in the last few years. When recent generative AI became available to the public, with models such as GPT [134] and DALL-E [135], people started to be aware of their immense power. Large language models like these have been a great new tool for providing meaningful conversations with people. When asked what an NN is, the AI explains it as follows:

> *A neural network is a type of artificial intelligence model inspired by the human brain. It consists of interconnected layers of nodes, known as "neurons", which process information using dynamic state responses to external inputs. Each neuron takes in multiple inputs, applies a weight to them, and passes them through an activation function to produce an output. The network learns by adjusting these weights based on the error of its predictions during training. This enables the model to recognize complex patterns and make predictions or decisions based on input data.*
>
> -CHATGPT-4

This touches on all major concepts involving NNs. In the coming sections, we will elaborate on each of them.

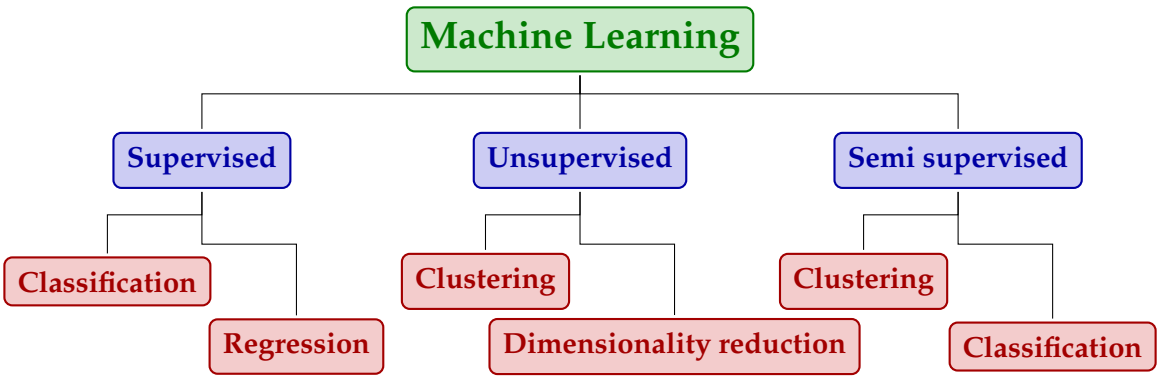

FIGURE 5.1: Machine learning types and applications [136].

5.1 Fundamental Concepts of Machine Learning

In general, ML is an umbrella name for algorithms that are designed to interpret large amounts of data. These techniques can be divided into three subclasses: supervised, unsupervised, and semi-supervised [137–139]. This divide is made to characterize the input and output of the algorithm. A supervised model is given a dataset and the desired target, it aims to "learn" the best mapping from data to the target. This process is called training. Unsupervised learning aims to find information in the data, without knowing the desired output. Figure 5.1 shows an overview of these classes and their applications, see [136] for commonly used ML algorithms.

ML is particularly promising for GW research since it allows us to analyze the big stream of data in an extremely short time. Many ML techniques have been tested on several GW analysis tasks, including methods to characterize the quality of data and classify the noise [11]. ML techniques have also been successful in GW modeling, detection, and parameter inference [12].

In this research, we employ supervised and unsupervised methods to construct an ML model, capable of doing PE for GW signals alternated by an MDR.

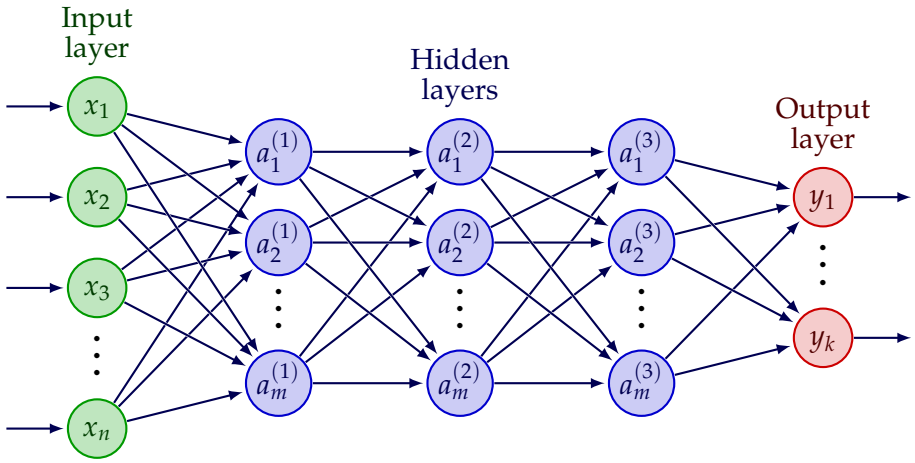

FIGURE 5.2: Illustration of the basic structure neural network.

5.1.1 Networks

An NN is a model in ML and part of a subfield called deep learning [140]. It has its origin as a numerical representation of the neural processes in the brain. It consists of an interconnected network of nodes (neurons) that can process information. One characterizes the flow of information in so-called layers of nodes, where the transformation flows from one layer to the next, characterized by the type of network. Figure 5.2 is drawn as a simple representation of a standard neural network, in which:

Input layer: The input data $\mathbf{x}$.

Hidden layer(s): The intermediate transformations of the data $\mathbf{a}^{(i)}$ in the i^{th} layer.

Output layer: The output of the network $\mathbf{y}$.

Here we introduced a new notation $\mathbf{x} = (x_1, x_2, \ldots, x_n)$ which defines a discrete list of numbers, in this case, the input data.

In this chapter, we will focus on the multi-layer perceptron, which consists of linear layers and non-linear activation functions. However, countless new NN architectures are proposed and updated regularly. To list a few commonly found in the literature: Recurrent Neural Networks (RNNs), Convolutional Neural Networks (CNNs), Generative Adversarial Network (GAN), Transformer Neural Networks (TNN), and countless more [141].

5.1.2 Multi-Layer Perceptron

The transformation of information between nodes from input $\mathbf{x}$ to output $\mathbf{y}$ can be parameterized by a multi-layer perceptron. In the simplest case, it is characterized by weights w_{ij} and biases b_i. Consider the transformation between two layers $\mathbf{a}^{(0)}$ and $\mathbf{a}^{(1)}$ as illustrated in figure 5.3, yields

$$a_1^{(1)} = \sum_{j=1}^{n} w_{1j} \cdot a_j^{(0)} + b_1^{(0)}, \tag{5.1}$$

which can be expressed as a matrix product,

$$\begin{aligned} \begin{pmatrix} a_1^{(1)} \\ \vdots \\ a_m^{(1)} \end{pmatrix} &= \begin{pmatrix} w_{11} & \dots & w_{1n} \\ \vdots & \ddots & \vdots \\ w_{m1} & \dots & w_{mn} \end{pmatrix} \begin{pmatrix} a_1^{(0)} \\ \vdots \\ a_n^{(0)} \end{pmatrix} + \begin{pmatrix} b_1^{(0)} \\ \vdots \\ b_m^{(0)} \end{pmatrix}, \\ \mathbf{a}^{(1)} &= \mathbf{W}^{(0)}\mathbf{a}^{(0)} + \mathbf{b}^{(0)}, \end{aligned} \tag{5.2}$$

where the discrete valued weights in matrix $\mathbf{W}$ and bias $\mathbf{b}$ parameterize the transformation of the layer connections.

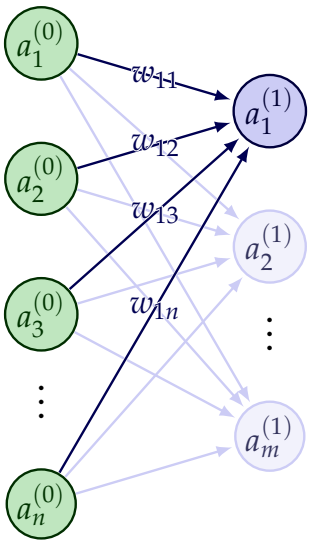

FIGURE 5.3: Illustration of connection between the layers.

So far, this NN can only describe linear transformations. To improve the network's expressivity, one introduces a so-called activation function $f(\mathbf{a})$. These are non-linear functions, introducing crucial non-linearity in the model transformation. Common activation functions are RELU and GELU functions [142],

$$\begin{aligned} f_{\text{RELU}}(\mathbf{a}) &= \begin{cases} \mathbf{a} & \mathbf{a} > 0 \\ 0 & \mathbf{a} \leq 0 \end{cases}, \\ f_{\text{GELU}}(\mathbf{a}) &= \frac{1}{2}\mathbf{a}\left(1 + \text{erf}\left(\frac{\mathbf{a}}{\sqrt{2}}\right)\right), \end{aligned} \tag{5.3}$$

where erf is the error function. The transformation to the next layer is then defined by

$$\mathbf{a}^{(i+1)} = f\left(\mathbf{W}^{(i)}\mathbf{a}^{(i)} + \mathbf{b}^{i}\right). \tag{5.4}$$

The transformation from input to output $\mathbf{x} \rightarrow \mathbf{y}$ is parameterized by a series of weights $\mathbf{W}^N$ and biases $\mathbf{b}^N$. N represents the number of layers in the network, called the neural depth. This collection of layers is called a multi-layer perceptron.

5.2 Training

By tuning the weights and biases, one can change the network output to the desired target output. This optimization process is called training. When training an NN, one essentially performs a form of parameter fitting. In this case, the parameters

are the weights and biases that comprise the network, usually an enormous number with modern networks reaching an order of a billion parameters [143]. Finding the optimal point, that best matches the target output, in this parameter space is therefore a hard endeavor. Described in this section are the key concepts used to combat this problem.

One starts by partitioning the data into three parts.

Training set: The dataset used for fitting the network parameters.

Validation set: The dataset used to validate the performance (not used for fitting).

Test set: The dataset used after the model is trained to assess the model's accuracy.

The training and validation sets are used in the training loop. This loop iterates first over the training set, where according to the methods explained below, the parameters of the network are optimized. To validate this optimization step, data from the validation set is used, where this data is never used for optimizing but serves to check if the optimization step was fruitful and to prevent overfitting. Training a network consists of iterating the above process for a large number of steps. After training, the model's performance is tested on unseen data, i.e. the test set. This checks if the trained model did not overfit, so the performance should be in line with the validation set.

5.2.1 Loss function

To characterize which direction the model should move in parameter space, the loss function $L(.)$ is defined. The inputs of this function are typically the network output $\mathbf{y}$ and the target output $\hat{\mathbf{y}}$. A common example is the mean-square error (MSE)

$$L_{\text{MSE}}(\mathbf{y}; \hat{\mathbf{y}}) = \frac{1}{N} \sum_{i=0}^{N} (y_i - \hat{y}_i)^2. \tag{5.5}$$

The MSE provides a distance from which the output is removed from the target. In general, the lower this loss gets, the better the fit.

There are many loss functions commonly used in ML. Their use is for a wide range of network architectures, see [144] for a recent review on this topic. Any loss function should have at least the following properties: It is continuous and differentiable, with a well-defined gradient with respect to the model parameters. Differentiability is essential because it allows for gradient-based optimization methods.

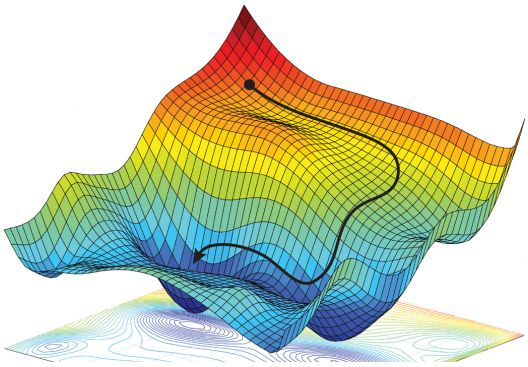

FIGURE 5.4: 2D representation of the loss function, where the arrow indicates the gradient descent process going from a high to a low place in the loss landscape. Figure from [145].

5.2.2 Gradient descent

To optimize the network, one needs to find the minimum of the loss function with respect to the data and the network parameters. The process of minimizing the loss is done during the training of the network. The fundamental technique used in this process is gradient descent.

Consider a loss function $L(\mathbf{y}; \hat{\mathbf{y}})$, where $\mathbf{y}$ is parameterized with weights $\mathbf{W}$ and biases $\mathbf{b}$ as transformation of input data $\mathbf{x}$. In the context of training, we can consider $\mathbf{x}$ and $\hat{\mathbf{y}}$ to be constant and imply their dependence in the loss function, i.e.

$$L(\mathbf{y}; \hat{\mathbf{y}}) = L(\mathbf{W}, \mathbf{b}; \mathbf{x}, \hat{\mathbf{y}}) = L(\mathbf{W}, \mathbf{b}). \tag{5.6}$$

Figure 5.4 illustrates the loss function as a surface, where the height indicates the value of the loss function. The other axes are the network parameters, in this 2D representation, these can be one weight and one bias. This forms the loss landscape, which in reality is a high-dimensional surface spanning all network parameters.

During training, we take small steps $\boldsymbol{\epsilon}$ in parameter space. To first order Taylor expansion, the loss

$$L(\mathbf{W} + \boldsymbol{\epsilon}, \mathbf{b} + \boldsymbol{\epsilon}) \simeq L(\mathbf{W}, \mathbf{b}) + \boldsymbol{\epsilon} \cdot \boldsymbol{\nabla} L(\mathbf{W}, \mathbf{b}), \tag{5.7}$$

where $\boldsymbol{\nabla} L(\mathbf{W}, \mathbf{b})$ defines the gradient of the loss function along the step. We want to ensure that the step we take minimizes the loss, which one can do with

$$L(\mathbf{W} + \boldsymbol{\epsilon}, \mathbf{b} + \boldsymbol{\epsilon}) = L(\mathbf{W}, \mathbf{b}) - \gamma |\boldsymbol{\nabla} L(\mathbf{W}, \mathbf{b})|^2 \leq L(\mathbf{W}, \mathbf{b}). \tag{5.8}$$

Combining equations 5.7 and 5.8 one finds

$$\begin{aligned} \boldsymbol{\epsilon} &\equiv -\gamma \boldsymbol{\nabla} L(\mathbf{W}, \mathbf{b}) \\ (\mathbf{W}, \mathbf{b})^{\mathbf{new}} &= (\mathbf{W}, \mathbf{b})^{\mathbf{old}} - \gamma \boldsymbol{\nabla} L(\mathbf{W}, \mathbf{b}), \end{aligned} \tag{5.9}$$

which defines the step $\boldsymbol{\epsilon}$ taken in parameter space. The parameter γ indicates the size of the step. This is often called the *learning rate*, a training parameter chosen to be not too big to prevent overshooting the loss minimum, but also not too small such that the minimum is reached in a reasonable amount of time.

This optimization scheme is called Stochastic Gradient Decent (SGD), and together with an adequate loss function and an expressive network, defines the complete training process of an NN network.

5.2.3 Optimizer

In reality, the high-dimensional surface described by the loss function is often very complicated. Navigating it with a scheme as SGD is slow and inefficient. Therefore, other optimizers have been created to aid training efficiency.

In this thesis, we use Adam (derived from adaptive moment estimation) to train the network [146]. It combines two gradient descent-based elements:

Moment 1: Parameter that takes into account current and previous gradient $\boldsymbol{\nabla} L$.
Moment 2: Parameter that takes into account squared gradients $|\boldsymbol{\nabla} L|^2$.

These moments are estimates of the mean and the uncentered variance of the gradient for each trainable parameter. This enables the optimizer to retain the gradient information from the previous steps, building up 'momentum' for each parameter. This momentum helps to move faster through the loss landscape and avoids getting stuck in local minima, making training more efficient.

5.3 Neural Contextualization Methods

As explained above, ML methods are used to study large datasets. Each input can consist of thousands or sometimes millions of values, for example, images. However, taking the complete dimensions as input quickly makes NNs enormous, and often hard to train. Instead, methods have been developed to reduce the dimensionality of the data, whilst retaining its information. This can be done both supervised and unsupervised or a combination of the two.

The goal is to create a transformation that contextualizes the data in such a way, that it is easier to access its information. Usually, this involves lowering the dimension of the data in a clever way. See [147, 148] for an overview of data reduction techniques.

In this research, we make use of two of these methods to represent GW data: Singular Value Decomposition (SVD) and a Residual Network (ResNet). As explained in chapter 3, much of the GW data strain is noise. Therefore, these methods seek to aid in lowering the data's dimensionality without losing much GW signal information, effectively removing some of the noise.

5.3.1 Singular Value Decomposition

SVD is an unsupervised ML technique that performs an eigendecomposition for non-square matrices. It is a method to decompose real or complex matrices. In general, ML applications using SVD involve matrix approximation, lowering the dimensionality of a matrix without losing much of its information [149, 150].

In principle, the SVD is a generalized eigenvalue decomposition, including non-square matrices. Let $n \times m$ matrix $\mathbf{X}$ be a data collection of network inputs, then

$$\mathbf{X} = \mathbf{U}\mathbf{\Sigma}\mathbf{V}^{\dagger}, \tag{5.10}$$

where $\mathbf{U}$ is an $m \times m$ unitary matrix, $\mathbf{\Sigma}$ an $m \times n$ diagonal matrix, and $\mathbf{V}$ is an $n \times n$ unitary matrix where $\mathbf{V}^{\dagger}$ is the conjugate transpose of $\mathbf{V}$. This reduces to the eigenvalue decomposition if $n = m$, then $\mathbf{U} = \mathbf{V}$. See [151] for a mathematical derivation.

like the eigenvalue decomposition, the SVD offers an orthonormal basis, where the columns of $\mathbf{U}$ represent 'eigenvectors' of matrix $\mathbf{X}$ and $\mathbf{\Sigma}$ their ordered 'eigenvalues' ($\mathbf{\Sigma} = \text{diag}(\sigma_1, \cdots, \sigma_m)$, where $\sigma_1 > \sigma_2 \cdots > \sigma_m$). This ordering ensures that the first vectors in $\mathbf{U}$ are on the so-called principle axis, meaning they point in the direction closest to most vectors in $\mathbf{X}$. One can project the information contained in $\mathbf{X}$ along a selected first number of vectors from $\mathbf{U}$. This yields the mathematically minimal mean squared distance between the data points and their projections, finding the best linear approximation to the data. If there are certain patterns or similarities in the data, this method will capture them, and use them to represent the data in a lower dimension.

In the context of GW, we use an SVD approach described in [152]. First, we define a data matrix $\mathbf{H}$ redefining $\mathbf{X}$. Let $\mathbf{H}$ consist of waveforms, where $h(t)$ is now a measurement over discrete time, such that waveforms are denoted as $\mathbf{h}$ of length n. Define

$$\mathbf{H} = \{\mathbf{h}_1, \mathbf{h}_2, \mathbf{h}_3, \cdots, \mathbf{h}_m\}, \tag{5.11}$$

then in component from, equation 5.10 becomes

$$H_{ij} = \sum_{k=1}^{m} u_{ik}\sigma_k v_{ki}. \tag{5.12}$$

Therefore, the reduced reconstruction of H is defined as

$$H_{ij} \approx H'_{ij} := \sum_{k=1}^{m'} u_{ik}\sigma_k v_{ki}, \tag{5.13}$$

where $m' \ll m$. This drastically reduces the number of basis vectors $\mathbf{U}$ needed, but this new $\mathbf{U}'$-basis still captures most information of the data. It is conventional to call this the SVD basis, with their vectors $\mathbf{u}'_k$ called SVD kernels.

One additional effect of representing the data in an SVD basis is noise reduction. The SVD basis is made on $\mathbf{H}$ containing noiseless GW strains. In this way, the SVD basis spans a space, optimized to represent GW signals. Noise information will roughly be represented equally over each basis vector. Since we reduce the dimensionality, a significant part of the noise will not be captured.

5.3.2 Residual Networks

Where the SVD basis is the optimal data representation for a generic GW $\mathbf{h}$ out of a dataset $\mathbf{H}$, it is not necessarily the best for a specific GW signal. In this research, we seek to do PE on a GW strain, which involves specific information from signal $\mathbf{h}$. This information is captured by specific SVD kernels. Therefore we seek a method that distills this information and puts it in a more insightful context, further reducing the dimensionality.

For this task, we employ a ResNet [153]. Suppose a NN that transforms input SVD representation $\mathbf{x}$ in a useful context $\mathbf{y}$. Then this transformation is characterized as $\mathcal{T}(\mathbf{x}) = \mathbf{y}$. When this transformation is sufficiently complex, one needs to add an increasing number of layers to the network. The results in a problem called degradation, where additional layers result in problems such as higher training errors, vanishing gradients, and saturated model performance [153, 154].

A ResNet tackles these problems, by introducing the so-called *skip connection* or *residual connection*. These allow deep NNs (many layers) to still retain input information by adding the input after the transformation and training the residual ($\hat{\mathcal{T}}$), i.e.

$$\hat{\mathcal{T}}(\mathbf{x}) = \mathcal{T}(\mathbf{x}) - \mathbf{x}, \tag{5.14}$$

where output is now defined as $\mathbf{y} = \hat{\mathcal{T}}(\mathbf{x}) + \mathbf{x}$. Figure 5.5 shows how such transformation could look like, which constitutes a residual block.

In practice, one stacks multiple of these blocks after each other, which has shown to be an effective method for contextualizing data [155]. The exact residual transformation depends on the chosen layer transformation under the skip connection.

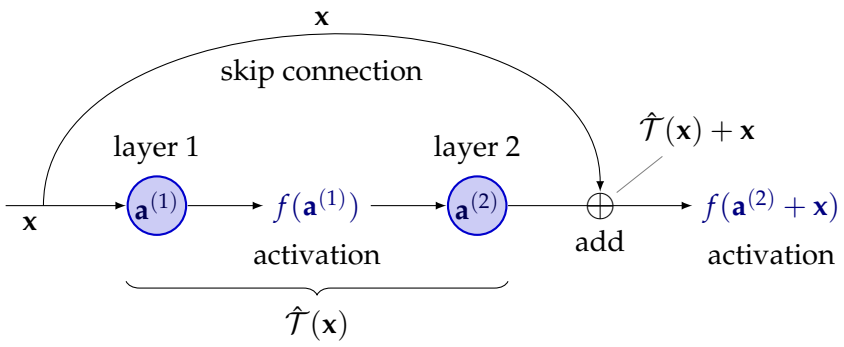

FIGURE 5.5: Illustration of a residual block.

Chapter 6

Neural Posterior Estimation

As discussed in chapter 3, the PE of GWs involves comparing data against simulated strains. Therefore, it falls under the umbrella of simulation-based inference. This can be done with a variety of classical and ML-based techniques [156]. In this work, we develop an ML method that can do PE for GW signals changed by an MDR. The technique used for this application is Neural Posterior Estimation (NPE) [157]. In this chapter, we will present one of the techniques used to do NPE, called Normalizing Flows (NFs).

The idea behind NPE is to do the neural equivalent of PE as described in section 3.3. The goal is to get close to the real posterior $P(\boldsymbol{\theta}|\mathbf{d})$ of a given discretized data strain $\mathbf{d}$, using via ML methods, hence

$$P_{NPE}(\boldsymbol{\theta}|\mathbf{d}) \approx P(\boldsymbol{\theta}|\mathbf{d}), \tag{6.1}$$

where the probability function P_{NPE} is represented by an NPE method.

For GWs, many NPE methods have been explored for various PE tasks [158–161]. The main advantage of NPE is its speed during inference compared to classical techniques [12, 91]. Where classical methods have to explore parameter space by computing the likelihood for each point (i.e. simulating the waveform and performing match filtering for each parameter set $\boldsymbol{\theta}$), an ML approach fits the data directly to the posterior because it already "knows" the whole parameter space of $\boldsymbol{\theta}$. The NPE algorithm gets to "know" the parameter space because it is trained on millions of simulated data. So, the primary distinction between PE and NPE lies in the fact that NPE transfers the majority of the computation to the training stage. Once trained, it is highly efficient in deriving the posterior.

This work uses an NPE method based on NFs [162]. NFs offers a natural way to generate distributions with a neural network. The effectiveness of this method in the analysis of GWs has been demonstrated in studies such as [158, 163, 164]. Although this technique provides very fast inference, posteriors can be less accurate than classical PE methods provide. To combat this, techniques such as importance sampling [165] and neural tuning [166] have been developed. These methods improve the posteriors to the desired comparability with conventional techniques, while maintaining significant speedups.

6.1 Normalizing Flows

The main idea behind NFs is to construct a NN that transforms a simple probability distribution $P(\mathbf{x})$ to the desired "more complicated" distribution $P(\mathbf{y})$. The simple distribution from which the transformation starts is called the base distribution and a popular choice is a normal distribution. During training, one uses the inverse transformation to transform samples from the desired distribution $\mathbf{y} \sim P(\mathbf{y})$, into

samples describing the base distribution $\mathbf{x} \sim P(\mathbf{x})$. This mapping allows the samples to "flow" through the transformation, resulting to be "normally" distributed (when a normal distribution is chosen as the base), hence the name *normalizing flows* [13, 162].

Important requirements of NFs are the invertibility and differentiability of the transformation,

$$\begin{aligned} \mathcal{T}(\mathbf{x}) &= \mathbf{y}, & \mathcal{T}^{-1}(\mathbf{y}) &= \mathbf{x}, \\ \mathbf{x} &\sim P_{\text{base}}(\mathbf{x}), & \mathbf{y} &\sim P_{\text{target}}(\mathbf{y}), \end{aligned} \tag{6.2}$$

where $\mathbf{x}$ and $\mathbf{y}$ are samples from the base P_{base} and desired P_{target} distribution, and $\mathcal{T}$ and $\mathcal{T}^{-1}$ the forward en inverse transformation, parameterized by the flow network. Transformations that are both invertible and differentiable are called *diffeomorphisms* and require that input and output have the same dimensionality $|\mathbf{x}| = |\mathbf{y}|$. Under these conditions, target distribution P_{taget} is well-defined and can be obtained via change of variables

$$P_{\text{target}}(\mathbf{y}) = \frac{P_{\text{base}}(\mathbf{x})}{|\det(J_{\mathcal{T}}(\mathbf{x}))|} \qquad \text{or} \qquad P_{\text{base}}(\mathbf{x}) = \frac{P_{\text{target}}(\mathbf{y})}{|\det(J_{\mathcal{T}^{-1}}(\mathbf{y}))|}, \tag{6.3}$$

where the Jacobian matrix $J_{\mathcal{T}}$ contains all partial derivatives of $\mathcal{T}$ with respect to the input elements x_n,

$$J_{\mathcal{T}}(\mathbf{x}) = \begin{pmatrix} \frac{\partial \mathcal{T}(x_1)}{\partial x_1} & \cdots & \frac{\partial \mathcal{T}(x_1)}{\partial x_n} \\ \vdots & \ddots & \vdots \\ \frac{\partial \mathcal{T}(x_n)}{\partial x_1} & \cdots & \frac{\partial \mathcal{T}(x_n)}{\partial x_n} \end{pmatrix}. \tag{6.4}$$

In practice, one uses a NN to parameterize the transformation $\mathcal{T}$.

Total transformation $\mathcal{T}$ is often split into layers of smaller transformations, hence the transformation needs to be *composable*. Imagine an NF consisting of many layers $\mathbf{a}^{(i)}$ connected with layer transformations $\mathcal{T}_i$. These NF layers together transform $\mathbf{x} \to \mathbf{y}$, now defined as $\mathbf{a}^{(0)} \to \mathbf{a}^{(k)}$. If all transformations $\mathcal{T}_i$ are diffeomorphic, the the following identities apply

$$\begin{aligned} \mathcal{T} &= \mathcal{T}_k \circ \cdots \circ \mathcal{T}_2 \circ \mathcal{T}_1, \\ \mathcal{T}^{-1} &= (\mathcal{T}_k \circ \cdots \circ \mathcal{T}_2 \circ \mathcal{T}_1)^{-1} = \mathcal{T}_1^{-1} \circ \mathcal{T}_2 \circ \cdots \circ \mathcal{T}_k^{-1}, \\ \det(J_{\mathcal{T}}(\mathbf{a}^{(0)})) &= \det(J_{\mathcal{T}_k}(\mathbf{a}^{(k-1)})) \cdots \det(J_{\mathcal{T}_1}(\mathbf{a}^{(0)})) = \prod_{i=0}^{k} \det(J_{\mathcal{T}_i}(\mathbf{a}^{(i)})), \end{aligned} \tag{6.5}$$

this is illustrated in figure 6.1, showing how an NF can transform a base distribution into a desired one.

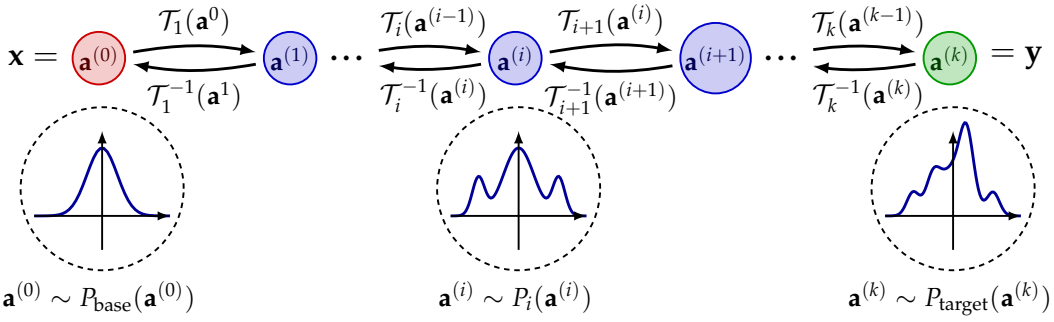

FIGURE 6.1: Illustration of an NF network, consisting of many layer transformations.

6.1.1 Bernstein Polynomials

For a typical NF network, the choice of transformation function is crucial. It not only affects the speed of the network via the difficulty of computing the inverse and derivative, but also dictates its expressive power and numerical stability. For our method, we use Bernstein polynomials that help to mitigate these effects [167]. Consider a transformation function $\mathcal{B}_n(x)$ that form the so-called Bernstein basis

$$\mathcal{B}_n(x) = \sum_{k=0}^{n} \alpha_k \binom{n}{k} x^k (1-x)^{n-k} \quad \text{with} \quad x \in [0,1]\,, \tag{6.6}$$

where $\binom{n}{k}$ is the binomial coefficient and α_k a constant that can be tuned to change the transformation. Note that these polynomials always take input $x \in [0,1]$, this ensures that the bounds of any n^{th} order polynomial are $\mathcal{B}_n(0) = \alpha_0$ and $\mathcal{B}_n(1) = \alpha_n$. If we ensure that all values α_k are monotonically increasing (i.e. $\alpha_{k-1} < \alpha_k < \alpha_{k+1}$[1]), then for all $x \in [0,1]$ the Bernstein polynomials are also monotonic funtions bounded by $\mathcal{B}_n(x) \in [\alpha_0, \alpha_n]$ [169]. This ensures that we can set out bounds for the in- and output of the transformation, mainly that samples from the base distribution need to be scaled such that $\mathbf{x} \in [0,1]$ and our target samples lay in bounds $\mathbf{y} \in [\alpha_0, \alpha_n]$. By fixing α_0 and α_n to the desired target range but keeping the rest of α_k as trainable parameters, we ensure that the output $\mathbf{y}$ stays bounded, making it very stable.

In fact, one can prove that: among all non-negative bases on a given interval, the Bernstein polynomial basis is optimally stable [170, 171].

For the inverse of the transformation of a given y, we solve for $x \in [0,1]$,

$$\begin{aligned} \sum_{k=0}^{n} \alpha_k \binom{n}{k} y^k (1-x)^{n-x} &= y \\ \sum_{k=0}^{n} (\alpha_k - y) \binom{n}{k} x^k (1-x)^{n-k} &= 0. \end{aligned} \tag{6.7}$$

Because the Berstein polynomial is monotonically increasing and we have ensured that y lays within the interval, x has a unique solution. This is solved by performing a root-finding method [172]. The method we employ is a bisection search. Although no analytic inverse exists of this transformer, the benefits of numerical stability and efficiency in expressing complex transformation within fewer parameters make this the ideal transformer to use for our application.

6.1.2 Coupling Flow

We have seen that GW signals have multiple parameters describing the waveform, and thus a higher-dimensional posterior to characterize. Constructing an NF network that treats all these distributions separately will greatly increase the number of computations needed to obtain the Jacobian determinant. To reduce the computational load, one likes to restrict the Jacobian to a triangular matrix. Its determinant only depends on its trace, reducing the number of computations significantly. One method that does this, by "coupling" different parameters together, is called *coupling flow* [173].

[1] We define α_k with network parameters θ_k by first using the softmax function to get positive values $\theta'_k = f_{\text{softmax}}(\theta_k) = e^{\theta_k} / \sum_{j=1}^{n} e^{\theta_j}$. From these values, we determine the coefficients $\alpha_k = \alpha_0 + \sum_{j<k} \theta'_k (\alpha_n - \alpha_0)$ for $k = 1, \ldots, n-1$. This ensures that the α_k are monotonically increasing in $[\alpha_0, \alpha_n]$ [168].

Let $\mathbf{x}_M$ be a M-dimensional input vector. A coupling flow layer, see figure 6.2, works by splitting the input into $\mathbf{x}_{1:m}$ and $\mathbf{x}_{m+1:M}$, where m is the element where we split usually chosen to be $m = M/2$. Then the total transformation $\mathcal{T}(\mathbf{x}_M) = \mathbf{y}_M$ is split into two parts:

The first part of the input $\mathbf{x}_{1:m}$ is transform via identity, i.e. $\mathbf{x}_{1:m} = \mathbb{1}(\mathbf{y}_{1:m}) = \mathbf{y}_{1:m}$. Thus the first part is left unchanged, but used to condition for the second half.

The second part $\mathbf{x}_{m+1:M}$ transformation is more involved. First we define the so-called coupling network $\mathcal{C}(\mathbf{x}_{1:m})$. This couples the parameters $\mathbf{x}_{1:m}$ to the other parameters $\mathbf{x}_{m+1:M}$. The transformation from $\mathbf{x}_{m+1:M}$ to $\mathbf{y}_{m+1:M}$ is given by the coupling transformation

$$\mathcal{T}_C(\mathbf{x}_{m+1:M}; \mathcal{C}(\mathbf{x}_{1:m})) = \mathbf{x}_{m+1:M}. \tag{6.8}$$

Hence, transformer $\mathcal{T}_C$ transforms $\mathbf{x}_{m+1:M}$, but is parameterized by $\mathcal{C}(\mathbf{x}_{1:m}))$.

Calculating the inverse of a coupling flow layer, see figure 6.2, is simple because of the following symmetry. Observe that $\mathbf{y}_{1:m} = \mathbf{x}_{1:m}$ and thus the output of the coupling network $\mathcal{C}(\mathbf{y}_{1:m}) = \mathcal{C}(\mathbf{x}_{1:m})$. This means that the only function needed to invert is $\mathcal{T}_C$, such that

$$\mathcal{T}_C^{-1}(\mathbf{y}_{m+1:M}; \mathcal{C}(\mathbf{y}_{1:m})) = \mathbf{x}_{m+1:M}. \tag{6.9}$$

An important observation one should make is that the coupling network $\mathcal{C}$ does not have the restriction of *diffeomorphic* transformations that NF dictates because it only parameterizes the transformation. This allows us to use any network, which grants much more expressive transformations.

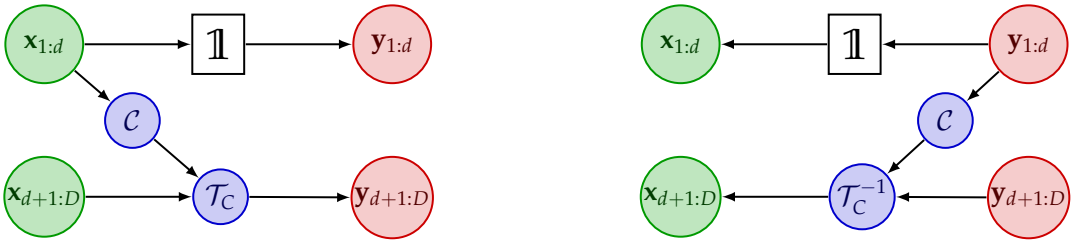

FIGURE 6.2: Illustration of the coupling transformation and its inverse.

The main advantage of this flow structure is computational efficiency. From equation 6.2 we know that to compute the change in variables of probability distributions, one needs to compute the determinant of the Jacobian matrix. This usually involves calculating $M \times M$ derivatives and computing a determinant of order M, so a total $\mathcal{O}(M^3)$ calculations are needed. The Jacobian matrix of a coupling flow is

$$J_{\mathcal{T}} = \begin{pmatrix} \frac{\partial \mathcal{T}_C(\mathbf{x}_{1:m};\mathcal{C})}{\partial \mathbf{x}_{1:m}} & \frac{\partial \mathcal{T}_C(\mathbf{x}_{m+1:M};\mathcal{C})}{\partial \mathbf{x}_{1:m}} \\ \frac{\partial \mathcal{T}_C(\mathbf{x}_{1:m};\mathcal{C})}{\partial \mathbf{x}_{m+1:M}} & \frac{\partial \mathcal{T}_C(\mathbf{x}_{m+1:M};\mathcal{C})}{\partial \mathbf{x}_{m+1:M}} \end{pmatrix} = \begin{pmatrix} \mathbb{1} & 0 \\ \frac{\partial \mathcal{T}_C(\mathbf{x}_{1:m};\mathcal{C})}{\partial \mathbf{x}_{m+1:M}} & \frac{\partial \mathcal{T}_C(\mathbf{x}_{m+1:M};\mathcal{C})}{\partial \mathbf{x}_{m+1:M}} \end{pmatrix} = \begin{pmatrix} \mathbb{1} & 0 \\ J_{1:m} & J_{m+1:M} \end{pmatrix}. \tag{6.10}$$

The Jacobian determinant is $|\mathbb{1} \cdot \det(J_{m+1:M}) - 0 \cdot \det(J_{1:m})| = |\det(J_{m+1:M})|$, notice that the anti-diagonal yield zero, so the derivatives of that part do not have to be calculated. what remains is $|\det(J_{m+1:M})|$, which one only has to calculate the derivatives concerning $\mathbf{x}_{m+1:M}$. This greatly reduces the order of computations.

To the observant reader, this procedure only transforms half of our parameters. Naturally, one wants to transform all parameters to their desired distribution. This is solved by introducing so-called permutation transformations or linear flows between coupling layers [13]. In the simplest case, one shuffles the input parameters $\mathbf{x}_M$ before putting it into the next flow transformation. This makes sure that a different set of parameters is transformed.

In this work, we make use of a simple anti-diagonal permutation $\mathbf{W}$. Let $\mathbf{a}_M^{(0)}$ and $\mathbf{a}_M^{(1)}$ be M-dimension layers, then our permutation takes form

$$\begin{aligned} \mathbf{a}_M^{(1)} &= \mathbf{W}\mathbf{a}_M^{(0)} \\ \begin{pmatrix} \mathbf{a}_{1:m}^{(1)} \\ \mathbf{a}_{m+1:M}^{(1)} \end{pmatrix} &= \begin{pmatrix} 0 & \mathbb{1} \\ \mathbb{1} & 0 \end{pmatrix} \cdot \begin{pmatrix} \mathbf{a}_{1:m}^{(0)} \\ \mathbf{a}_{m+1:M}^{(0)} \end{pmatrix} = \begin{pmatrix} \mathbf{a}_{m+1:M}^{(0)} \\ \mathbf{a}_{1:m}^{(0)} \end{pmatrix}. \end{aligned} \tag{6.11}$$

This switches the untransformed and transformed parts of the coupling flow, so this permutation ensures that after two flow layers, every parameter is transformed once. Observe that the absolute determinant of W equals one, so it does not affect the change of variables for the probabilities distributions in equation 6.2.

6.1.3 Conditional Normalizing Flows

For the application of GW PE, one not only wants to transform to the parameter posteriors, but one wants to do that conditional on a given data strain, i.e. we want the transformation, that yields the posteriors of parameters $\boldsymbol{\theta}$, to be dependent on a given data strain $\mathbf{d}$ (containing GW strain $\mathbf{h}(\boldsymbol{\theta})$ within the data). NF models that perform this are called conditional normalizing flows [174].

The posterior that we want to estimate with NPE will take the following form

$$P_{NPE}\left(\boldsymbol{\theta}|\mathbf{d}\right) = P_{\text{base}}\left(\mathbf{x}\right)\left|\det(J_{\mathcal{T}}(\mathbf{x};\mathbf{d}))\right|^{-1} \qquad \text{with} \qquad \mathcal{T}(\mathbf{x};\mathbf{d}). \tag{6.12}$$

Where we can impose a $\mathbf{d}$ condition on the transformation $\mathcal{T}$. There are several ways one can implement this, see [174] for an overview.

A coupling flow can incorporate this quite naturally. Remember that the coupling transformation was given by equation 6.8. It is hard to put a condition on the input ($\mathbf{x}_{m+1;M}$) of transform $\mathcal{T}_C$, given it will likely spoil diffeomorphism. On the contrary, we are free to put the condition on the coupling network $\mathcal{C}$, given that it does not have the restrictions of an NF transformation. Therefore we construct an NN that is conditioned by both the first half of $\mathbf{x}_M$ and GW strain D, i.e. $\mathcal{C}(\mathbf{x}_{1:m}, \mathbf{d})$. This can be done by adding more input dimensions to the coupling network. With a multi-layer perceptron, as described in chapter 5, one can map the output of the coupling network to the number of parameters that parameterize the coupling transformation $\mathcal{T}_C(\mathbf{x}_{m+1;M}; \mathcal{C}(\mathbf{x}_{1:m}, \mathbf{d}))$.

6.1.4 Training the Flow

In the sections above we have characterized how one parameterizes an NF transformation and its inverse. What is left is to define how to train the transformation such that it transforms to the desired distribution. Figure 6.3 illustrates the schemes followed during training and inference.

The training procedure can be thought of as consisting of three different steps:

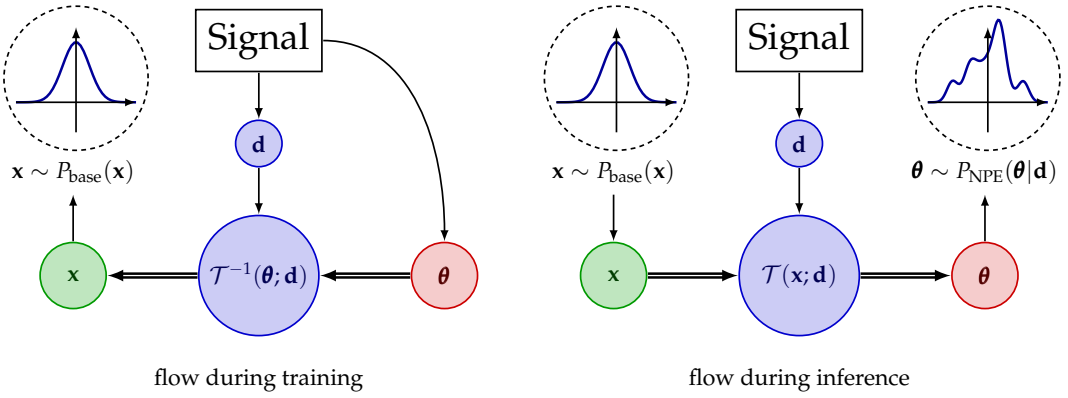

FIGURE 6.3: Illustration of the flow during training and inference.

Step 1. Data Generation: Simulating GW signals, yielding $\mathbf{d}$ and their according $\boldsymbol{\theta}$. One can think of a data generator making samples $\mathbf{d}, \boldsymbol{\theta}$ described by the desired posterior $P(\boldsymbol{\theta}|\mathbf{d})$.

Step 2. Inverse Flow: Performing the inverse flow transformation, obtaining parameters $\mathbf{x} = \mathcal{T}^{-1}(\boldsymbol{\theta};\mathbf{d})$ and the Jacobian determinant $|\det(J_{\mathcal{T}}^{-1}(\boldsymbol{\theta};\mathbf{d}))|$.

Step 3. Optimize: With the obtained quantities from step 2, one can calculate $P_{\text{NPE}}(\boldsymbol{\theta}|\mathbf{d})$. Via a loss function, one can characterize how well this probability distribution describes the desired one. The parameters describing the flow transformation $\mathcal{T}$ are then optimized to minimize the loss.

To optimize the transformation, we use the maximum (log-)likelihood loss $L_{\text{ML}}(.)$. This technique is also used in likelihood base inference [175], a widely used method of doing GW PE classically. The idea behind maximum likelihood is what the name suggests, maximizing the probability[2] according to the parameters describing it, in the context of ML, these parameters are the trainable parameters of the network. For NPE, the probability studied is parameterized by the flow transformation given in equation 6.12, which can be parameterized with the inverse transformation with

$$P_{NPE}\left(\boldsymbol{\theta}|\mathbf{d}\right) = P_{\text{base}}\left(\mathcal{T}^{-1}(\boldsymbol{\theta};\mathbf{d})\right)|\det(J_{\mathcal{T}^{-1}}(\boldsymbol{\theta};\mathbf{d}))|, \tag{6.13}$$

where we now have an expression for P_{NPE} that only depends on parameters know while training.

What we want to find is the best transformation $\mathcal{T}[\text{par}_{\text{best}}]$, where par_{best} are the parameters of the network that yield the optimal transformation. This is done by maximizing the posterior probability, i.e.

$$\begin{aligned}\mathcal{T}[\text{par}_{\text{best}}] &= \text{ARGMAX}_{(\text{par})}\left[P_{NPE}\left(\boldsymbol{\theta}|\mathbf{d}\right)\right], \\ &= \text{ARGMAX}_{(\text{par})}\prod_{i=1}^{N}\left[P_{NPE}(\boldsymbol{\theta}^{(i)}|\mathbf{d}^{(i)})\right],\end{aligned} \tag{6.14}$$

where $\boldsymbol{\theta}^{(i)}$ and $\mathbf{d}^{(i)}$ are the parameters and data strains of one specific GW signal, where there are a total of N signal samples in the dataset.

[2] The probability used classically is the likelihood defined by Bayes theorem, hence the name.

To make this a loss function that one can minimize, one takes the negative log

$$L_{ML}(\mathcal{T};\boldsymbol{\theta},\mathbf{d}) \equiv -\sum_{i=1}^{N} \log\left(P_{NPE}(\boldsymbol{\theta}^{(i)}|\mathbf{d}^{(i)})\right), \tag{6.15}$$

where we can use equation 6.13 to express the loss in know variables

$$L_{ML}(\mathcal{T};\boldsymbol{\theta},\mathbf{d}) = -\sum_{i=1}^{N}\left[\log\left(P_{\text{base}}(\mathcal{T}^{-1}(\boldsymbol{\theta};\mathbf{d}))\right) + \log\left(|\det(J_{\mathcal{T}^{-1}}(\boldsymbol{\theta};\mathbf{d}))|\right)\right]. \tag{6.16}$$

Notice that it is possible to put any non-negative scalar in front of the equation without changing the minimum of the loss function. In practice, one often takes the mean log-likelihood, such that the loss takes form

$$L_{ML}(\mathcal{T};\boldsymbol{\theta},\mathbf{d}) = -\frac{1}{N}\sum_{i=1}^{N}\left[\log\left(P_{\text{base}}(\mathcal{T}^{-1}(\boldsymbol{\theta};\mathbf{d}))\right) + \log\left(|\det(J_{\mathcal{T}^{-1}}(\boldsymbol{\theta};\mathbf{d}))|\right)\right]. \tag{6.17}$$

This is done so that the loss does not depend much on the size of the dataset, which makes it easier to compare losses. Finding the minimum loss will yield the best parameterization of $\mathcal{T}$, and thus describes the optimal distribution P_{NPE} given the data.

After training on millions of simulated GW signals, the transformation of conditional NF is tuned to be at the loss minimum. With this trained transformation one can infer the parameter posteriors of a GW data signal with only the data $\mathbf{d}$. One does that by sampling the base distribution and transforming these samples through the flow as illustrated in figure 6.3.

Part III

Research and Implementation

Chapter 7

Methodology

Now that we have laid out the theory, we can focus on the implementation. In this chapter, we explain the methods used to make our framework for performing NPE on GW signals with an MDR.

The entire framework is coded in Python using the JAX library [176]. The latter is similar to NUMPY in its functionality, but with built-in automatic differentiation, which makes it ideal for ML tasks. It allows for parallelization, using `vmap`, which enables fast data generation. Its just-in-time (`jit`) compiler transforms the code into a primitive version which allows for high-performance array computing. This can be run on accelerated hardware like a GPU, which makes the computational time orders of magnitude faster, and ideal for doing ML.

This chapter is structured as follows:

- First, we give a brief overview of the methods tested during the framework development and motivate the techniques used in our final framework.
- Secondly, we define the data generation process and talk about the characteristics of the data.
- Lastly, we present the architecture of the framework.

7.1 Brief Overview of Method Testing

At the beginning of our research, we decided to start with building a framework around a simple toy model. This was done to have good control over the complexity of the input data. The toy model used was a simple damped harmonic oscillator, parameterized by

$$h_{HO}(A, \omega, \phi, \delta; t) = A \sin(\omega t - \phi) e^{-\delta t}, \tag{7.1}$$

where A, ω, ϕ, and δ are the parameters for the model to infer. The first models were trained on noiseless data. We found that a conditional coupling flow, discussed in sections 6.1.2 and 6.1.3, yielded stable and accurate results.

Adding simple Gaussian noise to the signal worsened the performance significantly and major adaptation of the network was needed. Performing SVD on the signal, see figure 7.1, helped with the noise problems, drastically improving the network's performance. As discussed in section 5.3.1, this technique extracts the main features of the data and reduces the noise effects. In practice, the method works as follows. One plots the eigenvalues of the Σ matrix, looking at which kernel the eigenvalue curve flattens (the point at which the information captured by additional kernels is minor), determining how many kernels should be included in the reduced basis. This process is plotted in figure 7.1 where a dataset of toy model signals is used. Determining from the Σ curve, about 150 kernels are needed. Then, the data is represented in this SVD basis, yielding a noise-reduced version of the signal. In

figure 7.1, both the signal with noise (blue) and the SVD representation of this signal (green) are plotted above each other. On top is plotted the original signal (red) without noise. Observe that the SVD representation is significantly closer to the pure signal than the signal with noise, meaning that this successfully reduced the noise. However, there are some notable artifacts. Some small spikes are still visible, which is due to spikes in the noise. Although the noise is Gaussian, peaks are still expected. More interesting is the worsening of the fit from the SVD representation at the end of the strain. This is due to the data from which the SVD is made. Due to the damped nature of the harmonic oscillator, the amplitude is significantly reduced towards the end of most signals in the dataset, leading to less information captured by the SVD in that area of the signal. Although not all information might be captured with the SVD representation, it is more than enough to create a working NF model for noisy signals.

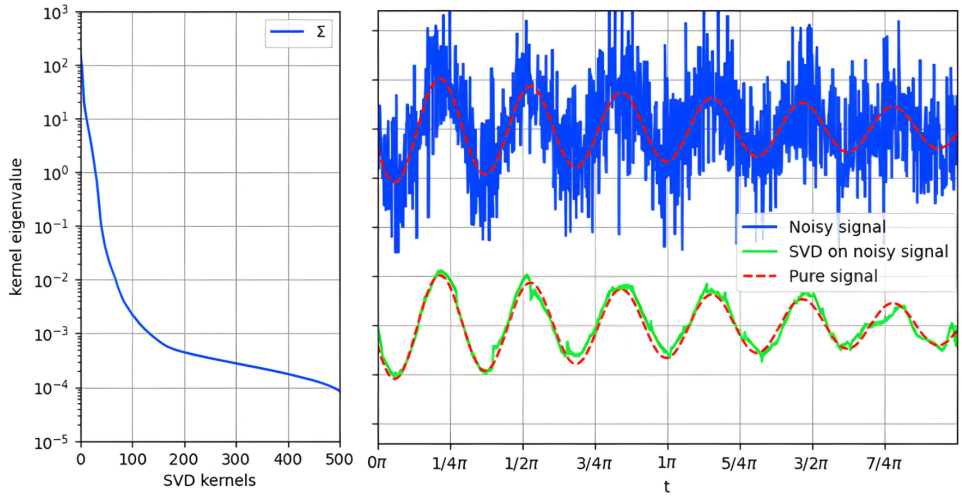

FIGURE 7.1: Example of an SVD of the signal for a damped harmonic oscillator. Left we represent the eigenvalues, and right the signal with noise as well as the signal reconstructed based on the SVD.

After this success, we moved on to GW signals generated by the data generator described in section 7.2. First, we tested this architecture on simplified GWs, meaning the signals were generated with no spin or MDR correction and no noise. After increasing the dimensionality of the network parameters (to deal with the increased complexity of the data), this approach yielded satisfactory results. Unfortunately, the introduction of noise led to a drastically reduced performance. This was solved by introducing a residual network to better contextualize the SVD basis to condition the NF on, see section 5.3.2. When gradually increasing the complexity by introducing more GW parameters, we finally had a model that could do NPE on GW signals with a modified dispersion relation.

However, during inference, the framework would occasionally present instabilities in the posteriors. Part of the posterior would lay outside of the regions that they were bound to. The exact cause of this behavior is still unknown, but we believe it may have been the transformer used. Initially, the NF was built with monotonic rational-quadratic splines as the transformer function, see [177] for details on spline transformers. By changing the transformer functions to Bernstein polynomials, the instabilities were no longer present. As described in section 6.1.1, this transformer provides optimal stability. This yielded a stable architecture that could be optimized for doing NPE on MDR-corrected waveforms.

7.2 Data Generation

In this research, we use simulated waveforms with an MDR correction, explained in chapter 4. The waveforms are generated according to equation 4.55, where the GW polarizations are modeled using the IMRPHENOMPV2 waveform [46], as seen in chapter 2[1]. Because both the derivation of MDR and the waveform model are defined in the frequency domain, we choose to do the whole framework in this domain.

7.2.1 Priors on the Parameters

The data generation starts by choosing the parameters $\boldsymbol{\theta}$ describing the waveform. For this, we describe probability functions for each parameter, the prior, to determine the range of values that parameter can take. When a new signal is generated, one sample is taken from these prior distributions. Table 7.1 summarizes the prior configuration of each parameter.

Parameter	Prior
Chirp mass ($\mathcal{M}$)	$\mathcal{U}(20,100)M_{\odot}$
Mass ratio (q)	$\mathcal{U}(0.125,1)$
Spin Amplitudes ($a_{1,2}$)	$\mathcal{U}(0,1)$
Spin tilt angles ($\theta_{1,2}$)	Uniform in sine
Spin vector azimuthal angle (ϕ_{JL})	$\mathcal{U}(0,2\pi)$
Spin precession angle (ϕ_{12})	$\mathcal{U}(0,2\pi)$
Inclination angle (θ_{JN})	Uniform in sine
Wave polarization (ψ)	$\mathcal{U}(0,\pi)$
Polar sky angle (θ)	$\mathcal{U}(0,2\pi)$
Azimuth sky angle (ϕ)	Uniform in cosine
Luminosity distance (D_L)	Rescaled to follow SNR (Mpc)
SNR	$P_{beta}(10,50)$
Coalescence time (t_c)	$\mathcal{U}(t_{\text{ref}}-0.1, t_{\text{ref}}+0.1)s$
Phase of coalescence (Φ_{ref})	$\mathcal{U}(0,2\pi)$
Phenomenological parameter α	Chosen from $[0, \frac{1}{2}, 1, \frac{3}{2}, 2, \frac{5}{2}, 3, \frac{7}{2}, 4]$
Phenomenological parameter A_{eff}	$\mathcal{U}(-5\times10^{-19}, 5\times10^{-19})$ peV$^{(2-\alpha)}$

TABLE 7.1: Summary of the parameters considered and their respective priors to generate BBH signals.

For most parameters, we consider a uniform prior distribution ($\mathcal{U}(\text{minimum}, \text{maximum})$), as shown in table 7.1. Some angles are chosen to be uniform in sine or cosine. This is done so that the spherical coordinates of both the spins and sky angles correspond to be uniform on the sphere.

[1]The waveforms are generated using the RIPPLE [178] library, more information on this topic is found in section 7.2.2.

To ensure we present our framework with signals in the detectable range, we choose to sample the signal's SNR. This is done with a scaled beta distribution

$$\begin{aligned} a =& 1 + T_{\text{SNR}} \frac{P_{\text{SNR}} - \text{Min}_{\text{SNR}}}{\text{Max}_{\text{SNR}} - \text{Min}_{\text{SNR}}}, \\ b =& 1 + T_{\text{SNR}} \frac{\text{Max}_{\text{SNR}} - P_{\text{SNR}}}{\text{Max}_{\text{SNR}} - \text{Min}_{\text{SNR}}}, \\ P_{\text{beta}}(x; a, b) =& \frac{\Gamma(a+b)}{\Gamma(a)\Gamma(b)} x^{a-1}(1-x)^{b-1}, \end{aligned} \tag{7.2}$$

where Γ is the gamma function. We chose the values for SNR temperature $T_{\text{SNR}} = 15$, peak SNR $P_{\text{SNR}} = 20$, SNR minimum $\text{Min}_{\text{SNR}} = 10$, and SNR maximum $\text{Min}_{\text{SNR}} = 50$ (see appendix A for an illustration). To adjust the SNR, we scale the luminosity distance accordingly. Importantly, this scaling is done before adding the MDR correction, because the phase shift according to the GR modification is parameterized partly by D_L. Because the correction to the waveform due to an MDR only introduces a frequency-dependent phase shift, this does not affect the optimal SNR[2].

Each value of phenomenological parameter α describes a different theory, for example, the value $\alpha = 0$ describes a massive graviton. This makes the morphologies of signals generated with different values drastically different. Therefore, we choose to keep α constant within the framework and train different models on each value of α. For the phenomenological parameter A_{eff}, a prior found in the literature is often a symmetric log, where the sample is uniform in the logarithm. However, our experiments found this leads to biases and unstable posteriors. Therefore, we chose a uniform prior to sample A_{eff}.

The coalescence time and phase are measured at a reference time of $1e9$ seconds GPS time. We vary the coalescence time with 0.1 seconds uniformly around this time. For real-world signals, one might think that this short time interval is a problem. However, the network is trained on all possible sky positions at that specific time. The only thing that changes when measuring at another time is that the earth has rotated. This means that we can artificially rotate the results for the sky position to represent the network at a different time. We still introduce a small timeshift because real strains containing a GW have some uncertainty in the exact coalescence time, which we like to get a posterior for.

7.2.2 Waveform Generation

As already mentioned, for the generation of the polarizations h_+ and $h_\times$ we use the IMRPHENOMPV2 model. It takes the parameters sampled from the prior and generates how the polarizations in the detector frame. This model is part of LALSIMULATION [33] but this package is not compatible with JAX. Therefore, we use the identical implementation of IMRPHENOMPV2 in the JAX-based library RIPPLE [178]. This ensures the speedups given in the JAX environment. We implemented the antenna pattern functions (equation 3.4) in JAX to transform the polarization to the detector frame. This is tested to be identical to the functions in the BILBY [179] library.

For the data setup, we use the current detector network, i.e. LIGO Hanford, LIGO Livingston [71], and Virgo [72]. Their noise realizations are generated from

[2] This is due to the phase canceling in the inner product, i.e. $\langle h^{\text{MDR}} \mid h^{\text{MDR}} \rangle = \langle h e^{i\Delta\Psi} \mid h e^{i\Delta\Psi} \rangle = e^{i\Delta\Psi - i\Delta\Psi} \langle h \mid h \rangle = \langle h \mid h \rangle$.

their PSD corresponding to their design sensitivity [180, 181]. The waveform generation is set up in five steps:

1. GW polarizations are generated according to the drawn priors.
2. The polarizations and luminosity distance are scaled according to the sampled SNR.
3. The GR modification is added to the polarizations according to the sampled phenomenological parameters.
4. The polarizations are combined into GW detector strain $h(t)$ and whitened according to PSD of the detector.
5. Gaussian noise is added to the signal to make a realistic whitened data strain

This whitening step is done to normalize the power at all frequencies, such that the resulting signal $\mathbf{d}$ has a standard deviation close to 1. Excess power, such as the presence of a GW, at any frequency will be more visible in this representation. This makes it easier for the NPE architecture.

Our data $\mathbf{d}$ is generated from a minimum frequency of 20 Hz and with a sampling frequency of 2048 Hz a reference frequency of 20 Hz. The duration of the simulated data is 10 seconds, making the total dimension of $\mathbf{d}$ for three detector strains in frequency domain $(3, 10241)$.

7.2.3 Flat-Space

The representation of the parameters to the network is also important. Because each parameter has its own prior, the domain of each parameter is different. For the network to function properly, we need to ensure that these domains are similar to one another. This is done by so-called flat-space transformations, where we map all parameters to the same "flat" domain. This is especially necessary for the Bernstein transformation, given that its inputs can only be on the domain $\mathbf{x} \in [0, 1]$. An important note is that these flat-space transformations need to be invertible to allow for both training and inference.

For parameters with uniform priors, this mapping is trivial. One scaled the minimum and maximum to be the bounds of the desired domain. For the angles in both the spin and sky locations parameters, this mapping is more involved. The angles have periodic properties that are hard to grasp for our model. To solve this we designed a particular flat-space transformation. As an example, consider the sky position angles θ, ϕ, and the luminosity distance D_L. These parameters give the position vector $\vec{r}$ from earth to the source. This vector spans a spherical volume in Cartesian space, which we project to a cubical volume. The x, y, and z coordinates of this transformation are now not periodic and are used to map to the desired flat-space domain. Similarly, one can do the same procedure with the spin vectors $\vec{S}_{1,2}$.

In the early stages of development, we found that the flat-space domain of $[-4, 4]$ worked and kept using it. In the Bernstein transformations, this domain is then again trivially mapped to domain $[0, 1]$.

7.3 Network Architecture

Our network is implemented using JAX-based ML packages EQUINOX [182] and FLOWJAX [183]. EQUINOX is used for the general architecture of the network, whilst FLOWJAX is specifically used for the creation of the NF.

7.3.1 Context Network

The first step of contextualizing the data is SVD, as described in section 5.3.1. Note that we generate our signals in the frequency domain, thus the SVD kernels are complex. During testing, we found that for the phenomenological value of $\alpha = 0$, 700 kernels in the SVD basis were enough to properly model the signal (see appendix A for an illustration). This number is kept the same throughout the different values of α to ensure that the network stays the same size. This number is sufficient for each value of α considered in this research, given that the MDR significantly changes the signal. This is due to the phase shift scaling with $\Delta\Psi(f) \propto h^{\alpha-2} f^{\alpha-1}$. As a back-of-the-envelope calculation, the product between the Planck constant in peV ($\mathcal{O}(10^{-3})$) and a typical GW frequency ($\mathcal{O}(10^{2})$) will yield a value smaller than 1, thus with increasing alpha, the phase shift gets smaller.

Remember that the dimension of the generated data $\mathbf{d}$ is $(3, 10241)$. After the SVD this will be reduced to $(3, 700)$. Unfortunately, we cannot feed complex values to this network architecture, therefore we split the complex and real parts. The input for the ResNet is (6,700).

To further contextualize the data we use a residual network, as described in section 5.5. Figure 7.2 illustrates the architecture of our ResNet. We start with a liner input layer $\mathbf{x}$ that takes the dimension $(6, 700)$ to (1024), this is called an encoder. We found that layer normalization [184] in this transformation is essential for stabilizing the GW signal information. So, the residual block begins with a GELU activation function (equation 5.3) followed by a normalization layer. The first linear layer transforms the input to four times the dimension (4096). After another GELU activation and normalization layer, the second linear layer takes the dimension back to (1024). Moving up and down the dimension enables the network to have enough parameters to extract the data's information without changing the input and output dimensions. This residual block is repeated five times before parsing to the decoder $\mathbf{y}$. Here, a linear layer transforms the dimension of the context to the output dimension of (512).

This output $\mathbf{y}$ is the context of the data given to the NF network. In the context of NF, we will represent the contextualized data as $\mathbf{d}'$.

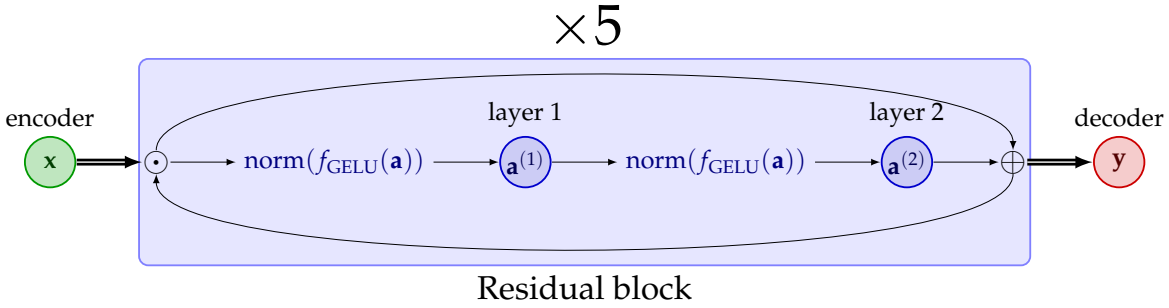

FIGURE 7.2: Illustration of the architecture of the residual network. In the blue box is the residual block represented, which is repeated five times in this network.

7.3.2 Normalizing Flow Architecture

The flow architecture is based on a conditional coupling flow, described in sections 6.1.2 and 6.1.3. An illustration of the flow is given in figure 7.3. The transformation is parameterized with Bernstein polynomials $\mathcal{B}_n$, see equation 6.6. Our model uses

the Bernstein polynomial up to order $n = 64$. This means that the trainable parameters describing the transformations have dimension 64, thus the coupling network $\mathcal{C}$ needs to have 64 as its output dimension.

The flow transforms the 16 parameters describing the signal, i.e.

$$\boldsymbol{\theta} = (\mathcal{M}_c, q, a_1, a_2, \theta_1, \theta_2, \phi_{JL}, \phi_{12}, \theta_{JN}, \psi, D_L, \theta, \phi, t_c, \Phi_{ref}, A_{eff}). \tag{7.3}$$

The coupling network $\mathcal{C}$ has inputs of half the parameters (8) and the data from the context network $\mathbf{d}'$ with dimension (512). Figure 7.3 shows the coupling network on the right. It consists of two linear layers connected via the RELU activation function. The first layer takes the input dimension (520) to the dimension (50). the second layer transforms the dimensions to (64), the needed dimension for the Bernstein parameterization.

As shown left in figure 7.3, the total flow consists of seven repeated coupling flow layers. The green arrows indicate the flow during inference, while the red arrows mark the training direction of the flow.

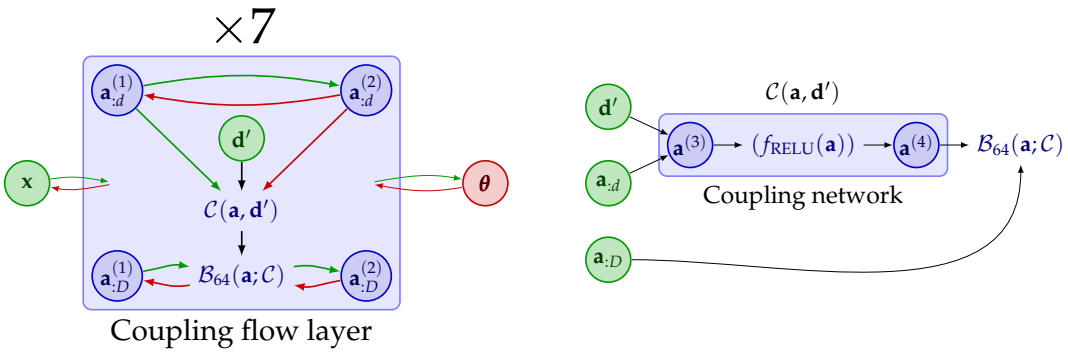

FIGURE 7.3: Illustration of the architecture of the coupling flow and the coupling network. On the left, we see the flow represented by the arrows, where green represents the direction during inference and red the direction during training. On the right, we see the inputs that parameterize the transformation.

The base distribution we use is a truncated normal within the interval of $[-4, 4]$, where samples from the distribution $\mathbf{x}$ are used as input of the flow transformation. Similar to the flat-space transformation, sampling from this probability distribution allows us to have good control of the input domain and lets us easily scale to the [0,1] domain of the Bernstein transformation.

7.3.3 Training

During the training process, about 400 million samples are generated. For training, we use the Adam optimizer with a learning rate of 1×10^{-4}, from the OPTAX package [185]. This allows us to find the minimum of the loss more efficiently, as explained in section 5.2.3.

Our training procedure consists of 100000 epochs. Each of them starts by taking 4096 samples from the data generator, split into 90% training and 10% validation samples. During each epoch, samples are parsed through the network in batches of 512, where the network is optimized to minimize the training loss. After training, the validation loss is calculated. If this is lower than the previous lowest validation loss, the network parameters are updated. Regardless of whether the network parameters are updated or not, the validation step marks the end of an epoch. This process is repeated until 100000 epochs are reached.

Chapter 8

Results and Discussion

In this section, we present our results. First, we show the posteriors obtained in the form of a corner plot. Then we test for possible bias using Probability Probability plots (PP plots). We will conclude with a discussion on measurements of phenomenological parameter A_α.

8.1 Corner Plots

A common representation of the posteriors of the GW parameters $\boldsymbol{\theta}$ are so-called corner plots. These plots visualize the 1d posterior distributions of each parameter on the diagonal, forming a triangular matrix of plots with the parameters on both axes. This matrix is filled in with the 2d probability contours of the two parameters located at that specific intersection of the matrix. This allows us to visualize correlations between parameters. The parameters $\boldsymbol{\theta}_{\text{True}}$ (true values) used for the generation of the injected signal are indicated by the orange lines. The vertical dashed lines in the 1d posteriors indicate the 90% confidence interval of the distribution. The contour plots correspond to 1, 2, and 3 standard deviations and have decreasing saturation, respectively. The median and 1 standard deviation values of each parameter are plotted above each posterior. Complete corner plots of prior sampled signals for different values for phenomenological parameter α can be found in Appendix B.

The corner plots are made with 15000 samples from the flow base distribution. We chose to convert some of the inference parameters $\boldsymbol{\theta}$, to express them in a more meaningful context.

For the spin, we use the expression χ_{eff} and χ_p as defined in equation 2.10. While gravitational waves depend on spin parameters beyond effective ones, extracting this information is a complex task due to the limited information per event and biases due to waveform model misspecification, see [186].

We also convert A_{eff} to A_α via equation 4.53. Note that this involves calculating redshift z. This cannot be obtained directly with GWs, therefore we need cosmological constants from other measurements. In this thesis, we use FLATLAMBDACDM cosmology described by constants obtained from PLANCK15 [120]. The redshift is obtained by converting the inferred luminosity distance. Given that the prior for A_{eff} is quite small, we choose to plot the values of A_α in $10^{-19}\text{peV}^{\alpha-2}$.

The coalescence time is represented by a time shift $\Delta\tau = t_{ref} - t_c$ from the reference time. This is done to keep the number more tractable.

The corner plots, figures B.1 to B.9, show that our model can infer all parameters. Given that this test of GR using an MDR with the group velocity is relatively new, there is no current literature on similar models to compare. From our observations, we can make the following statements.

1. In general, the network seems to produce similar posteriors that one would expect for the GW parameters.

2. True values of the injected signals lay in their posteriors as expected.

3. The network can make the difference between positive and negative values of A_α well. This is interesting, given that classical tests of MDR conducted in the past have relied on splitting the prior of this parameter in a positive and negative side [10, 131, 132]. This framework is able to infer both sides simultaneously.

In figure 8.1 we show some interesting phenomena of the corner plots regarding A_α and luminosity distance D_L. These two parameters are correlated with each other via equation 4.53. This is visible by the shape the contours make, see $\alpha = 0$ plot, where the contour has a diagonal and slightly curved shape. This is expected given that the parameters are linearly related, a larger D_L means more propagation distance. For the observed signal to keep a similar phase shift due to the MDR, A_α has to decrease. Observe that for $\alpha = 1$ the network is unable to infer A_α and we have a flat distribution. This is expected because, at this value of α, the phase shift according to the MDR is frequency-independent, see equation 4.54. This makes the measurement of A_α degenerate with the coalescence phase of the GW.

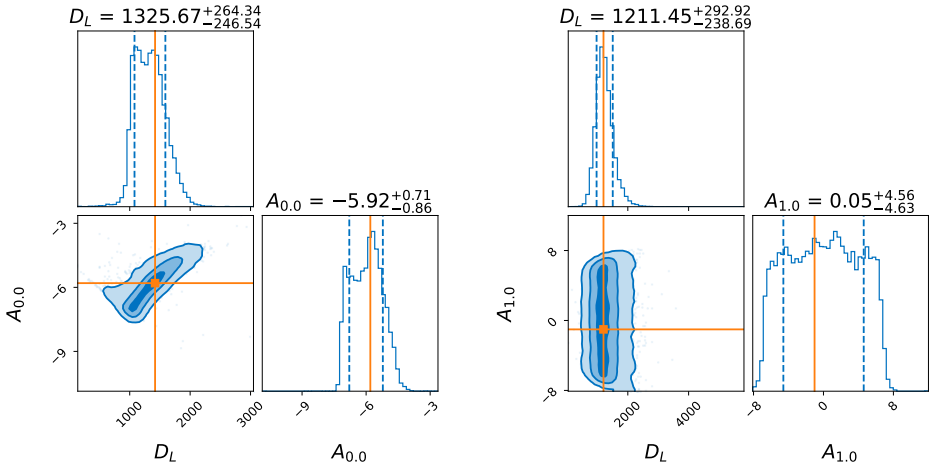

FIGURE 8.1: Corner plots of the posteriors of luminosity distance d_L[Mpc] and $A_\alpha[10^{-19}\text{peV}^{\alpha-2}]$ for $\alpha = 0$ (left) and $\alpha = 1$ (right).

In figure 8.2 we can also observe interesting phenomena regarding A_α and time shift $\Delta\tau$. These two parameters are uncorrelated with each other for all values of α except for $\alpha = 2$. This is visible by the diagonal shape the contours make This is expected because, at this value of α, the phase shift according to the MDR scales linearly with the frequency, which is identical to a time translation of the waveform. Therefore, the inference of these two parameters is degenerate and thus is significantly worsened.

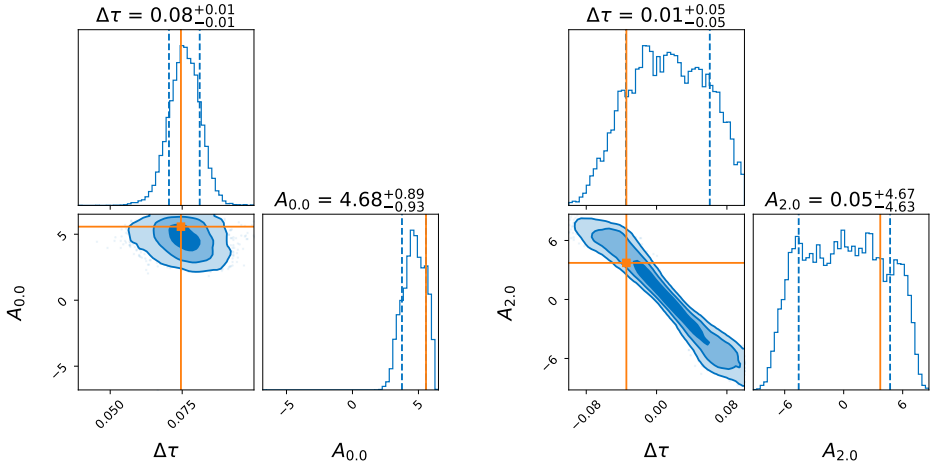

FIGURE 8.2: Corner plots of the posteriors of time shift $\Delta\tau$[s] and $A_\alpha[10^{-19}\ \mathrm{peV}^{\alpha-2}]$ for $\alpha = 0$ (left) and $\alpha = 2$ (right).

8.2 PP plots

To test the network for potential biases, we made PP plots (Probability-Probability plots). These plots are a measure of certain biases, necessary to have a trustworthy, i.e. non-biased network. On a PP plot, the cumulative fraction of true values (the parameter values used in data generation) in confidence interval (C.I.) is plotted against the width of the C.I. used. To give an example, on the lower 10% C.I. of the posterior distribution (from 0.0 to 0.1 in the pp-plot), we expect 10% of the injected values (true values) to lie within that C.I. and on C.I. from 0.0 to 0.5, we expect to find 50%, et cetera. A diagonal line in the PP plot shows that the posterior probability distributions behave how one would expect. Deviations of the diagonal can indicate bias but effects from fluctuations due to noise can also influence this.

For the creation of the PP plots given in figure 8.3, our model was tested on a dataset of 1000 simulated GW strains. Each strain was used to generate a posterior of 15000 samples. This is done for all different values of α. We choose to only infer the parameters used in data generation, and do no conversion on the spin parameters and A_{eff}. This is done to ensure that we do not introduce unwanted correlations between parameters, which could lead to perceived biases.

Plotted for each parameter in the label are the p-values. These are calculated with a Kolmogorov-Smirnov test [187] and are a measure to determine if the difference between the expected distribution of a parameter and the cumulative distribution function of the posterior distribution is significant. A p-value of 1 corresponds to a posterior distribution that is exactly Gaussian around its parameter. The posterior distributions for GW parameters are much more complicated and one can interpret the p-value of order 0.1 to be good. Usually, there are some outliers of lower p-values. If one bad posterior is generated from an outlier in the dataset, the p-value can be drastically lowered. The low p-values for $\Delta\tau$ and A_{eff} at $\alpha = 2$ are probably more susceptible to this due to their correlation. The other low p-values need further investigation. We expect longer training will improve the p-values further.

From the PP- plots shown in figure 8.3, we can make the following observations:

1. All parameters follow a diagonal line for every value of α, giving no indication of significant bias.
2. P-values of most parameters are as expected.
3. According to the lines and p-values of A_{eff}, the network is stable in inferring the phenomenological parameter.

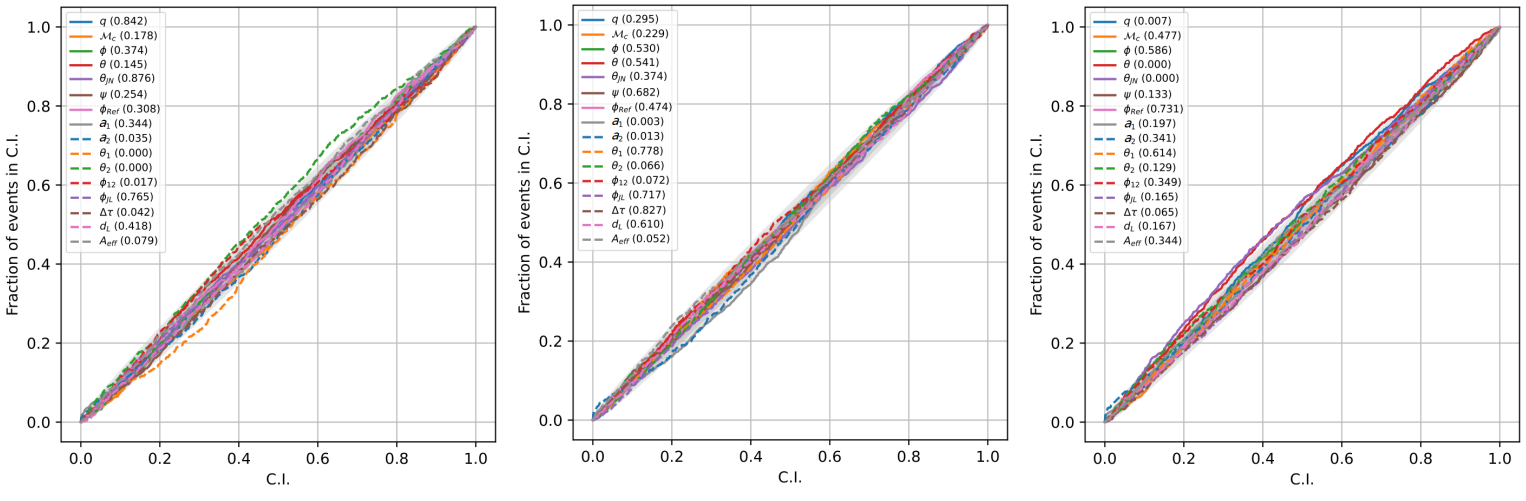

(A) $\alpha = 0$.

(B) $\alpha = \frac{1}{2}$.

(C) $\alpha = 1$.

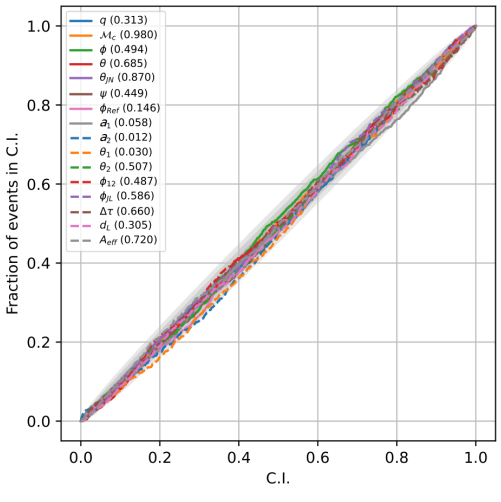

(D) $\alpha = \frac{3}{2}$.

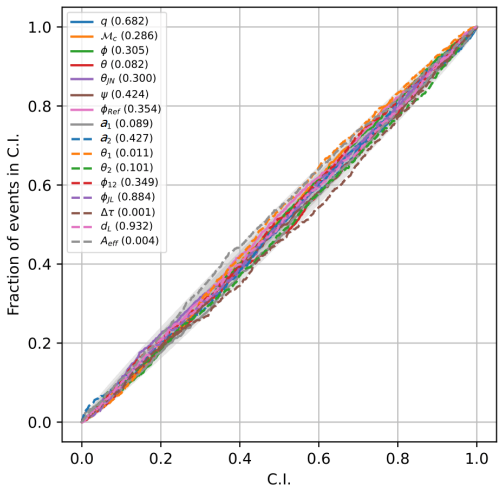

(E) $\alpha = 2$.

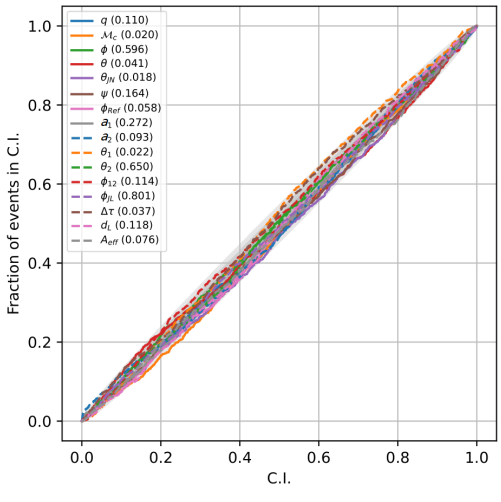

(F) $\alpha = \frac{5}{2}$.

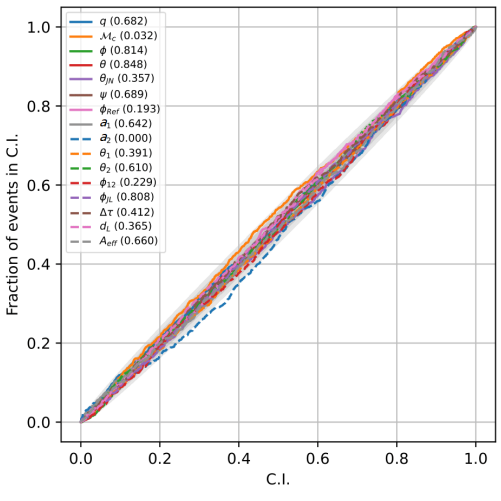

(G) $\alpha = 3$.

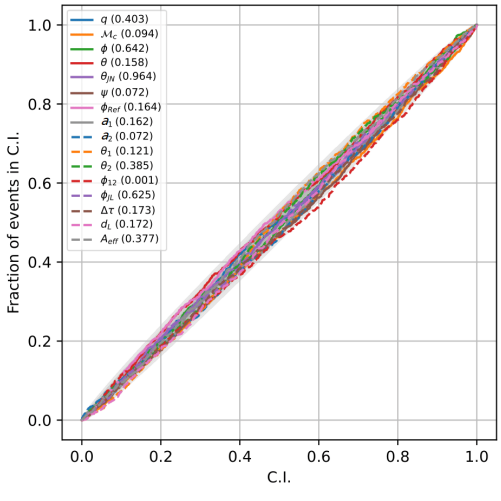

(H) $\alpha = \frac{7}{2}$.

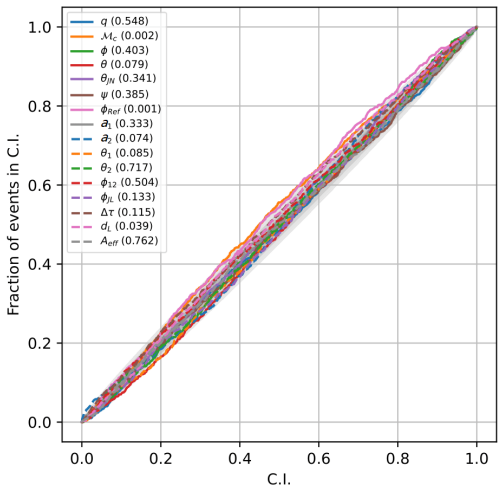

(I) $\alpha = 4$.

FIGURE 8.3: PP-plots for models trained on different values of phenomenological parameters α. One can observe that all parameters follow the diagonal, given no sign of significant bias.

8.3 Measurements of A_α

To illustrate how well the network can infer phenomenological parameter A_α, we created a similar plot as figure 4.1. Although not comparable, given that this figure is acquired by combining multiple signals and using an MDR correction derived for the particle velocity, a similar plot can illustrate the performance of the network at different values of α. Therefore, a signal was created with phenomenological parameter $A_{eff} = 0$, which is the same for all values of α. Figure 8.4 shows such a violin plot of A_α. The plotted posteriors have their mean indicated by a black dot and dashed lines reflecting the 90% confidence region.

Observe the expected flat posterior at $\alpha = 1$, where the phase shift $\Delta\Psi(f)$ according to the considered MDR is frequency independent, which makes it degenerate with the coalescence phase of the GW. In addition, we see that the posterior for $\alpha = 0$ is the most accurate. This is as expected, given that this value has the strongest effect on the signal, i.e. the value of the phase shift $\Delta\Psi(f)$ (equation 4.54) scales with $1/\hbar^2$ which is a large number. Remember that this value of α corresponds to a massive graviton, measuring $A\alpha$ accurately puts stronger constraints on the graviton mass. The worse performance at $\alpha = 2$ can be explained by the degeneracy between phase shift $\Delta\Psi(f)$ and the time shift $\Delta\tau$. In theory, this causes the values of the inferred A_α and $\Delta\tau$ to take any combination such that

$$\Delta\Psi(f)/f + \Delta\tau = -\frac{\pi h^{\alpha-2}}{c} D_\alpha(z)(1+z)^{\alpha-1} A_\alpha + \Delta\tau = \text{constant}, \tag{8.1}$$

effectively broadening both posteriors considerably. For the other values of α, the higher order in the Planck constant makes the GR deviation smaller, yielding worse posteriors. Interestingly, we get more accurate posteriors for the higher values of α, which is also observed in figure 4.1. This can be explained with similar arguments as for $\alpha = 0$, only here the $\Delta\Psi(f)$ depends on increasing order of the frequency. In the units used here, we have $h \sim \mathcal{O}(10^{-3})$, so frequencies close to $\mathcal{O}(10^3)$) will increase in order alpha, thus taking a bigger role in the overall waveform, yielding a stronger dependence on A_α.

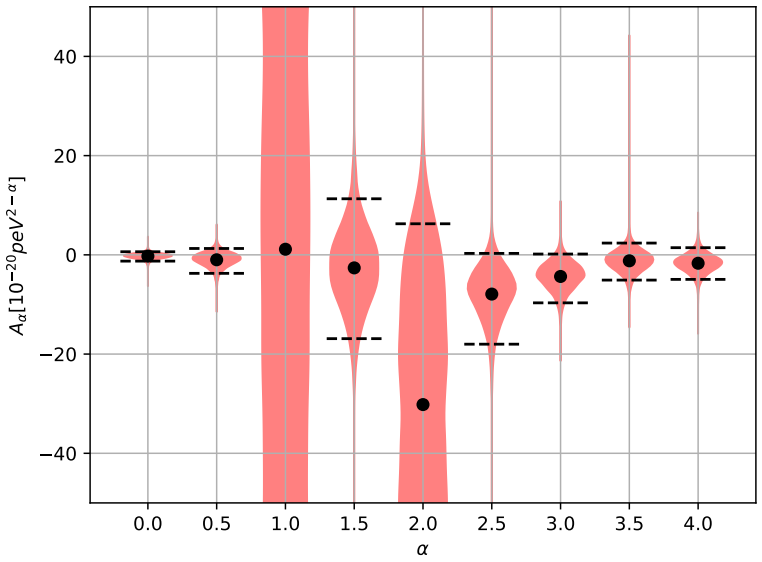

FIGURE 8.4: Violin plot of the posterior of A_α inferring the same GW stain, generated with $A_\alpha = 0$.

To further explore the behavior of our framework, we choose to compare three different values for effective parameter A_{eff}, between different SNR values. We do this analysis on a GW signal for phenomenological parameter $\alpha = 0$, corresponding to the massive graviton. Figure 8.5 shows the violin plots obtained, where the GW signal was generated with constant A_{eff} over the tested SNR range, with the values 0 (red), 10^{-19} (blue), and -10^{-19} (green). The choice of keeping A_{eff} constant is because this causes the MDR phase shift $\Delta\Psi(f)$ to scale linearly with the luminosity distance D_L. Given that we scale the D_L with the SNR, this results in a linear dependence on SNR for the phenomenology of $\Delta\Psi(f)$. We choose to show the posteriors for phenomenological parameter A_α, where one should note that for larger SNR, thus a smaller D_L, leading to smaller A_α. Therefore, in figure 8.5 the values of A_α corresponding to the used A_{eff} are plotted as back lines.

For the red posteriors corresponding to $A_{eff} = 0$, We observe the posteriors first shrink and then broaden with increasing the SNR. Given that there is no phase shift for the value of A_α, this behavior is suspected to come from the way the network is trained. As explained in section 7.2.1, the network is trained on a beta distribution of SNR values. This means that the network is primarily trained on samples where this distribution has the highest likelihood, in this case around SNR=20. This explains why the behavior of posteriors is the smallest around this point. We expect that exposing the network to more high SNR signals will improve these posteriors.

The blue and red posteriors, corresponding to $A_{eff} = \pm 10^{-19}$, show a more insightful correlation between the SNR of the signal and the inferred posteriors. First of all, observe that all inferred posteriors encompass the true values. This is important because this shows that this framework can correctly distinguish between positive and negative values for A_α. Furthermore, we observe that the posteriors improve with increased SNR. This is as expected because the phase shift $\Delta\Psi$ should be more pronounced with louder signals. At about the SNR value of 30, the posteriors are the same shape. This is expected to be due to the phase shift $\Delta\Psi(f)$ getting smaller due to shorter D_L, making inference of A_α harder.

Considering everything presented, the plots show that this framework is capable of making measurements of phenomenological parameter A_α.

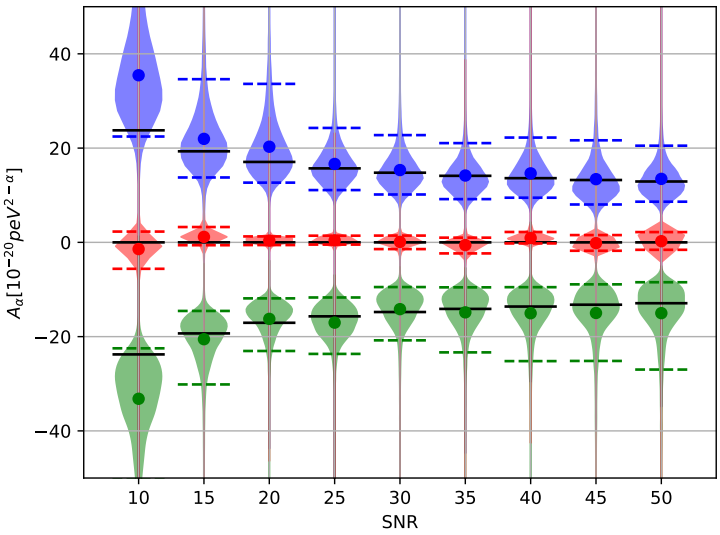

FIGURE 8.5: Violin plot of the posterior of A_α inferring the same GW signal with different SNR, generated with effective parameter $A_{eff} = 0$ (red), 10^{-19} (blue), and -10^{-19} (green) (conversion to A_α are the plotted black lines). The points and dashed lines indicate the mean and 90% confidence regions of the respective colored distribution.

Chapter 9

Conclusion and Outlook

This work presents a machine learning framework that can infer posteriors for phenomenological parameters describing modified dispersion relations in gravitational waves. With this proof-of-concept model, we show that a normalizing-flow-based model is a viable avenue for doing tests of general relativity relating to a modification in the propagation speed of gravitational waves. We have shown that our framework is capable of doing the complete parameter inference of all the gravitational wave parameters in addition to the one describing the modified dispersion relation.

Current tests of general relativity using conventional methods are time-consuming, given that they need to do complete parameter estimation for all values of α separately. This means multiple runs of methods such as nested sampling and Markov Chain Monte Carlo [91] per signal. Each run can take in the order of days to analyze [188–190], making a full analysis to test a modified dispersion relation on a signal in the order of multiple weeks. With the expected increase in the number of signals by a factor of ~ 3.3 in the fourth observing run due to detector sensitivity upgrades [180], a faster procedure of doing parameter estimation is needed Our procedure takes only in the order of seconds per signal. This means that this architecture can be used to do neural posterior estimation on a lot of signals in a matter of minutes.

The modified dispersion relation studied in this thesis was derived from the group velocity of a gravitational wave [123]. This is a relatively new approach with no parameter estimation results found in the literature. Therefore, this framework might give some insights into expected results. Firstly, our results show that it is possible to do parameter estimation on the positive and negative side of phenomenological parameter A_α at the same time. This might also be possible with classical methods. Furthermore, the inference of A_α at $\alpha = 1$ is degenerate with the phase[1], which might be wanted to be taken out of the analysis, similarly what is done for the previous test of general relativity [10, 131, 132]. Also, we observed that the analysis of A_α at $\alpha = 2$ is degenerate with a time shift. This needs to be taken into account when doing conventional parameter estimation.

The framework presented in this thesis has a few areas that we consider expanding. First, the waveform model used in this work was IMRPHENOMPV2. The newer IMRPHENOMXPHM model that includes higher-order modes could be used. We expect that this model should make it easier to distinguish modified dispersive behavior because higher-order modes have different frequency characteristics, and thus a frequency-dependent phase shift due to a modified dispersion will be effected differently for each mode. In this research, the generation of waveforms was performed using RIPPLE [178] due to its speed. Unfortunately, the IMRPHENOMXPHM model

[1]This behavior was previously observed at $\alpha = 2$ using the phase velocity to derive the dispersion relation.

is currently not implemented in RIPPLE. However, preliminary tests using IMRPHENOMXPHM implemented in LALSUITE [33] have shown that this network architecture is trainable on these waveforms and learns the posteriors. Further research is needed to verify that this also produces more accurate posteriors.

Secondly, to improve the posteriors one can use importance sampling [165]. Tests have shown that this is a viable approach, although the current framework has some stability issues. For the use of this method, the posteriors produced need to: encompass the true value, which is the case for the presented framework. The posterior samples also need to have high efficiency, meaning that individual posterior samples describe the signal well. This is not the case for the current framework. longer training to further decrease the loss might solve this, but an additional invention is needed to be able to implement this.

Thirdly, the current framework can do PE on a single gravitational wave data stain. However, testing for a modification of general relativity should apply to all signals equally. Therefore, combining the information of all detected signals, as done in the literature, is what helps constrain these modified theories more strongly. This is also an avenue we would like to explore with this framework. There are machine-learning methods developed to do this combining procedure. Sequential neural score estimation, developed in [191], is such a method that guides inference using the approximation of the posterior, obtained from previous results, at the observation of interest. By sequentially combining signal posterior information, one obtains a total posterior for all signals analyzed. We think this is a promising method for combining the posterior information on the phenomenological parameter A_α and should be explored in future research on this topic.

One challenge that arises when moving to realistic data is noise characterization. The framework presented here works on signals generated with the advanced LIGO-Virgo detector network at their design sensitivity [94]. In reality, a gravitational wave signal could have non-Gaussian in the form of glitches, that one needs to subtract [192] or find other ways to extract the signal from the noise. For our framework, this means to adapt the context network. There are machine learning methods developed for this context, see [193, 194], that one can explore for the adaptation of our framework.

One can also think of extending this work to the next generation of detectors like ET [74] and CE [75]. Due to their higher sensitivity, they will be able to measure the phenomenology of waveforms far more accurately. Also the LISA [76] telescope will probe a different regime of frequencies. Because a modified dispersion relation is frequency-dependent, the LISA will be able to explore different morphologies. Due to the increased sensitivity of these detectors, we expect a greater number of detections. Some challenges that arise are that the signals will be longer in the detector's sensitive band, i.e. detecting signals from a lower frequency [195]. This means that the data strains of the signals are longer, so adaptation of the context network is needed to handle large input data.

To summarize: Due to the expected increase in the number of detections, the current method for doing tests of general relativity on gravitational waves will be too slow. Therefore, the development of faster methods to do these kinds of analyses is needed. In this thesis, we present our proof-of-concept neural posterior estimation framework using normalizing flows to speed up these analyses significantly. The tests conducted on our framework show promising results. Once the challenges mentioned above are addressed, this machine learning approach can be an important stepping stone for doing parameter estimation of gravitational waves modified by a dispersion relation.

Bibliography

[1] A. Einstein, "Die grundlage der allgemeinen relativitätstheorie", Annalen der Physik **354**, 769–822 (1916).

[2] W.-T. Ni, "Solar-system tests of the relativistic gravity", Int. J. Mod. Phys. D **25**, 1630003 (2016).

[3] C. M. Will, "The Confrontation between General Relativity and Experiment", Living Rev. Rel. **17**, 4 (2014).

[4] A. Einstein, "Näherungsweise Integration der Feldgleichungen der Gravitation", Sitzungsberichte der Königlich Preussischen Akademie der Wissenschaften zu Berlin, 688–696 (1916).

[5] R. A. Hulse and J. H. Taylor, "Discovery of a pulsar in a binary system", Astrophys. J., Lett., v. 195, no. 2, pp. L51-L53, 10.1086/181708 (1975).

[6] A. Królak and M. Patil, "The First Detection of Gravitational Waves", Universe **3**, 59 (2017).

[7] G. W. O. S. C. (GWOSC), *Event list* (2024).

[8] B. P. Abbott et al., "GW170817: Observation of Gravitational Waves from a Binary Neutron Star Inspiral", Phys. Rev. Lett. **119**, 161101 (2017).

[9] B. P. Abbott et al., "Multi-messenger Observations of a Binary Neutron Star Merger", Astrophys. J. Lett. **848**, L12 (2017).

[10] R. Abbott et al., "Tests of General Relativity with GWTC-3", (2021).

[11] E. Cuoco, A. Iess, F. Morawski, and M. Razzano, "Machine Learning for the Characterization of Gravitational Wave Data", in (2021).

[12] E. A. Huerta and Z. Zhao, "Advances in Machine and Deep Learning for Modeling and Real-Time Detection of Multi-messenger Sources", in (2021).

[13] G. Papamakarios, E. Nalisnick, D. J. Rezende, S. Mohamed, and B. Lakshminarayanan, *Normalizing flows for probabilistic modeling and inference*, 2021.

[14] S. Mirshekari, N. Yunes, and C. M. Will, "Constraining Generic Lorentz Violation and the Speed of the Graviton with Gravitational Waves", Phys. Rev. D **85**, 024041 (2012).

[15] A. Janiak and I. Newton, "Correspondence with richard bentley [1692–3]", in *Isaac newton: philosophical writings*, edited by A. Janiak, Cambridge Texts in the History of Philosophy (Cambridge University Press, 2004), 94–105.

[16] D. Baumann, *Lecture notes on general relativity*, Master Physics and Astronomy (2023/24).

[17] S. M. Carroll, *Spacetime and Geometry: An Introduction to General Relativity* (Cambridge University Press, July 2019).

[18] H. Genz, *Nothingness: the science of empty space* (Perseus books publishing, 1999).

[19] I. Belahcene, "Searching for gravitational waves produced by cosmic strings in ligo-virgo data", PhD thesis (Laboratoire de l'accélérateur linéaire, Oct. 2019).

[20]C. Van den Broeck, *Lecture notes on gravitational waves theory & observations*, Master Experimental Physics (2023/24).

[21]M. Maggiore, *Gravitational waves : volume 1, theory and experiments* (Oxford : Oxford University Press, 2007).

[22]K. S. Thorne, "Multipole expansions of gravitational radiation", Rev. Mod. Phys. **52**, 299–339 (1980).

[23]L. London, S. Khan, E. Fauchon-Jones, C. García, M. Hannam, S. Husa, X. Jiménez-Forteza, C. Kalaghatgi, F. Ohme, and F. Pannarale, "First higher-multipole model of gravitational waves from spinning and coalescing black-hole binaries", Phys. Rev. Lett. **120**, 161102 (2018).

[24]V. Varma, P. Ajith, S. Husa, J. C. Bustillo, M. Hannam, and M. Pürrer, "Gravitational-wave observations of binary black holes: effect of nonquadrupole modes", Phys. Rev. D **90**, 124004 (2014).

[25]S. M. Carroll, *Lecture notes on general relativity: the schwarzschild solution and black holes* (1997).

[26]S. Isoyama, R. Sturani, and H. Nakano, "Post-Newtonian templates for gravitational waves from compact binary inspirals", 10.1007/978-981-15-4702-7_31-1 (2020).

[27]J. Centrella, J. G. Baker, B. J. Kelly, and J. R. van Meter, "Black-hole binaries, gravitational waves, and numerical relativity", Rev. Mod. Phys. **82**, 3069–3119 (2010).

[28]N. Sago, S. Isoyama, and H. Nakano, "Fundamental tone and overtones of quasinormal modes in ringdown gravitational waves: a detailed study in black hole perturbation", Universe **7**, 10.3390/universe7100357 (2021).

[29]T. W. Baumgarte and S. L. Shapiro, *Numerical Relativity: Solving Einstein's Equations on the Computer* (Cambridge University Press, 2010).

[30]K. Chatziioannou, A. Klein, N. Yunes, and N. Cornish, "Constructing gravitational waves from generic spin-precessing compact binary inspirals", Phys. Rev. D **95**, 104004 (2017).

[31]N. Science, *Chapter 2: reference systems*, https://science.nasa.gov/learn/basics-of-space-flight/chapter2-2/.

[32]LIGO Scientific Collaboration, Virgo Collaboration, and KAGRA Collaboration, *Functions to transform waveform parameters between lalsimulation and lalinference coordinate conventions*, https://lscsoft.docs.ligo.org/lalsuite/lalsimulation/group__lalsimulation__inference.html, 2024.

[33]LIGO Scientific Collaboration, Virgo Collaboration, and KAGRA Collaboration, *LIGO Algorithm Library - LALSuite*, 2018.

[34]LIGO Scientific Collaboration, Virgo Collaboration, and KAGRA Collaboration, *Routines for generating binary inspiral gravitational waveforms*, 2024.

[35]T. Damour, B. R. Iyer, and B. S. Sathyaprakash, "A Comparison of search templates for gravitational waves from binary inspiral", Phys. Rev. D **63**, [Erratum: Phys.Rev.D 72, 029902 (2005)], 044023 (2001).

[36]T. Damour, B. R. Iyer, and B. S. Sathyaprakash, "Frequency domain P approximant filters for time truncated inspiral gravitational wave signals from compact binaries", Phys. Rev. D **62**, 084036 (2000).

[37]L. E. Kidder, C. M. Will, and A. G. Wiseman, "Spin effects in the inspiral of coalescing compact binaries", Phys. Rev. D **47**, R4183–R4187 (1993).

[38]N. T. Bishop, "Introduction to Gravitational Wave Astronomy", in (2021).

[39]A. Buonanno and T. Damour, "Effective one-body approach to general relativistic two-body dynamics", Phys. Rev. D **59**, 084006 (1999).

[40]T. Damour, "The General Relativistic Two Body Problem and the Effective One Body Formalism", Fundam. Theor. Phys. **177**, edited by J. Bicak and T. Ledvinka, 111–145 (2014).

[41]P. Ajith et al., "A Template bank for gravitational waveforms from coalescing binary black holes. I. Non-spinning binaries", Phys. Rev. D **77**, [Erratum: Phys.Rev.D 79, 129901 (2009)], 104017 (2008).

[42]P. Ajith et al., "Inspiral-merger-ringdown waveforms for black-hole binaries with non-precessing spins", Phys. Rev. Lett. **106**, 241101 (2011).

[43]L. Santamaria et al., "Matching post-Newtonian and numerical relativity waveforms: systematic errors and a new phenomenological model for non-precessing black hole binaries", Phys. Rev. D **82**, 064016 (2010).

[44]S. Husa, S. Khan, M. Hannam, M. Pürrer, F. Ohme, X. Jiménez Forteza, and A. Bohé, "Frequency-domain gravitational waves from nonprecessing black-hole binaries. I. New numerical waveforms and anatomy of the signal", Phys. Rev. D **93**, 044006 (2016).

[45]M. Hannam, P. Schmidt, A. Bohé, L. Haegel, S. Husa, F. Ohme, G. Pratten, and M. Pürrer, "Simple Model of Complete Precessing Black-Hole-Binary Gravitational Waveforms", Phys. Rev. Lett. **113**, 151101 (2014).

[46]S. Khan, K. Chatziioannou, M. Hannam, and F. Ohme, "Phenomenological model for the gravitational-wave signal from precessing binary black holes with two-spin effects", Phys. Rev. D **100**, 024059 (2019).

[47]G. Pratten, S. Husa, C. Garcia-Quiros, M. Colleoni, A. Ramos-Buades, H. Estelles, and R. Jaume, "Setting the cornerstone for a family of models for gravitational waves from compact binaries: The dominant harmonic for nonprecessing quasi-circular black holes", Phys. Rev. D **102**, 064001 (2020).

[48]C. Bambi, S. Katsanevas, and K. D. Kokkotas, eds., *Handbook of Gravitational Wave Astronomy* (Springer Singapore, 2021).

[49]L. Blanchet, "Analytic approximations in GR and gravitational waves", Int. J. Mod. Phys. D **28**, 1930011 (2019).

[50]A. G. M. Lewis and H. P. Pfeiffer, "GPU-accelerated simulations of isolated black holes", Class. Quant. Grav. **35**, 095017 (2018).

[51]B. Bruegmann, "Binary black hole mergers in 3-d numerical relativity", Int. J. Mod. Phys. D **8**, 85 (1999).

[52]T. Zhao, Z. Cao, C.-Y. Lin, and H.-J. Yo, "Numerical Relativity for Gravitational Wave Source Modelling", 10.1007/978-981-15-4702-7_34-1 (2021).

[53]A. H. Mroue et al., "Catalog of 174 Binary Black Hole Simulations for Gravitational Wave Astronomy", Phys. Rev. Lett. **111**, 241104 (2013).

[54]M. Boyle et al., "The SXS Collaboration catalog of binary black hole simulations", Class. Quant. Grav. **36**, 195006 (2019).

[55]J. Healy and C. O. Lousto, "Fourth RIT binary black hole simulations catalog: Extension to eccentric orbits", Phys. Rev. D **105**, 124010 (2022).

[56]D. Ferguson et al., "Second MAYA Catalog of Binary Black Hole Numerical Relativity Waveforms", (2023).

[57]L. Blanchet, "Gravitational radiation from postNewtonian sources and inspiraling compact binaries", Living Rev. Rel. **5**, 3 (2002).

[58]P. Jaranowski and G. Schäfer, "Derivation of local-in-time fourth post-Newtonian ADM Hamiltonian for spinless compact binaries", Phys. Rev. D **92**, 124043 (2015).

[59]S. Khan, S. Husa, M. Hannam, F. Ohme, M. Pürrer, X. J. Forteza, and A. Bohé, "Frequency-domain gravitational waves from nonprecessing black-hole binaries. ii. a phenomenological model for the advanced detector era", Phys. Rev. D **93**, 044007 (2016).

[60]P. Schmidt, M. Hannam, S. Husa, and P. Ajith, "Tracking the precession of compact binaries from their gravitational-wave signal", Phys. Rev. D **84**, 024046 (2011).

[61]J. J. Sakurai and J. Napolitano, *Modern Quantum Mechanics*, Quantum physics, quantum information and quantum computation (Cambridge University Press, Oct. 2020).

[62]A. Pound and B. Wardell, "Black hole perturbation theory and gravitational self-force", 10.1007/978-981-15-4702-7_38-1 (2021).

[63]A. Le Tiec and L. Blanchet, "The Close-limit Approximation for Black Hole Binaries with Post-Newtonian Initial Conditions", Class. Quant. Grav. **27**, 045008 (2010).

[64]S. Detweiler and L. H. Brown, "Post-minkowski expansion of general relativity", Phys. Rev. D **56**, 826–841 (1997).

[65]E. Berti, *Ringdown — pages.jh.edu*, https://pages.jh.edu/eberti2/ringdown/, [Accessed 30-05-2024].

[66]M. Ruderman, "Pulsars: structure and dynamics", Ann. Rev. Astron. Astrophys. **10**, 427–476 (1972).

[67]B. P. Abbott et al., "LIGO: The Laser interferometer gravitational-wave observatory", Rept. Prog. Phys. **72**, 076901 (2009).

[68]B. Caron et al., "The VIRGO interferometer for gravitational wave detection", Nucl. Phys. B Proc. Suppl. **54**, edited by M. Bassan, F. Fucito, I. Modena, V. Ferrari, and M. Francaviglia, 167–175 (1997).

[69]L.-V.-K. Colaboration, *Compact binary catalogue*.

[70]T. Akutsu et al., "KAGRA: 2.5 Generation Interferometric Gravitational Wave Detector", Nature Astron. **3**, 35–40 (2019).

[71]J. Aasi et al., "Advanced LIGO", Class. Quant. Grav. **32**, 074001 (2015).

[72]F. Acernese et al., "Advanced Virgo: a second-generation interferometric gravitational wave detector", Class. Quant. Grav. **32**, 024001 (2015).

[73]M Saleem, J. Rana, V Gayathri, A. Vijaykumar, S. Goyal, S. Sachdev, J. Suresh, S Sudhagar, A. Mukherjee, G. Gaur, B. Sathyaprakash, A. Pai, R. X. Adhikari, P Ajith, and S. Bose, "The science case for LIGO-india", Classical and Quantum Gravity **39**, 025004 (2021).

[74]M. Maggiore et al., "Science Case for the Einstein Telescope", JCAP **03**, 050 (2020).

[75]M. Evans et al., "A Horizon Study for Cosmic Explorer: Science, Observatories, and Community", (2021).

[76]P. A. Seoane et al., "Astrophysics with the Laser Interferometer Space Antenna", Living Rev. Rel. **26**, 2 (2023).

[77]K. D. for the LISA Study Team, "Lisa - an esa cornerstone mission for a gravitational wave observatory", Classical and Quantum Gravity **14**, 1399 (1997).

[78]G. Hobbs et al., "The international pulsar timing array project: using pulsars as a gravitational wave detector", Class. Quant. Grav. **27**, edited by Z. Marka and S. Marka, 084013 (2010).

[79]G. Agazie et al., "The NANOGrav 15 yr Data Set: Observations and Timing of 68 Millisecond Pulsars", Astrophys. J. Lett. **951**, L9 (2023).

[80]N. S. Pol et al., "Astrophysics Milestones for Pulsar Timing Array Gravitational-wave Detection", Astrophys. J. Lett. **911**, L34 (2021).

[81]M. Bailes et al., "Gravitational-wave physics and astronomy in the 2020s and 2030s", Nature Rev. Phys. **3**, 344–366 (2021).

[82]LIGO, *Gravitational waves*, `https://www.ligo.caltech.edu/page/gravitational-waves`, 2021.

[83]A. A. Michelson and E. W. Morley, "On the Relative Motion of the Earth and the Luminiferous Ether", Am. J. Sci. **34**, 333–345 (1887).

[84]B. P. Abbott et al., "Sensitivity of the Advanced LIGO detectors at the beginning of gravitational wave astronomy", Phys. Rev. D **93**, [Addendum: Phys.Rev.D 97, 059901 (2018)], 112004 (2016).

[85]J. Casanueva Diaz, "Fabry-perot cavities in advanced virgo", in *Control of the gravitational wave interferometric detector advanced virgo* (Springer International Publishing, Cham, 2018), pp. 37–83.

[86]F. Matichard et al., "Seismic isolation of Advanced LIGO: Review of strategy, instrumentation and performance", Class. Quant. Grav. **32**, 185003 (2015).

[87]A. Buonanno and Y. Chen, "Signal recycled laser interferometer gravitational wave detectors as optical springs", Phys. Rev. D **65**, 042001 (2002).

[88]J. T. Whelan, *The geometry of gravitational wave detection* (2013).

[89]P. Nguyen et al., "Environmental noise in advanced ligo detectors", Class. Quant. Grav. **38**, 145001 (2021).

[90]R. Abbott et al., "GWTC-2: Compact Binary Coalescences Observed by LIGO and Virgo During the First Half of the Third Observing Run", Phys. Rev. X **11**, 021053 (2021).

[91]A. Królak, "Principles of gravitational-wave data analysis", in *Handbook of gravitational wave astronomy*, edited by C. Bambi, S. Katsanevas, and K. D. Kokkotas (Springer Singapore, Singapore, 2020), pp. 1–37.

[92]gwistat, *Gravitational wave detector network*, `https://online.igwn.org`, 2021.

[93]B. P. Abbott et al., "GW170814: A Three-Detector Observation of Gravitational Waves from a Binary Black Hole Coalescence", Phys. Rev. Lett. **119**, 141101 (2017).

[94]D. Davis et al., "LIGO detector characterization in the second and third observing runs", Class. Quant. Grav. **38**, 135014 (2021).

[95]E. Thrane and C. Talbot, "An introduction to Bayesian inference in gravitational-wave astronomy: Parameter estimation, model selection, and hierarchical models", pasa **36**, e010, e010 (2019).

[96]R. N. Lang, "Compact binary systems in scalar-tensor gravity. ii. tensor gravitational waves to second post-newtonian order", Phys. Rev. D **89**, 084014 (2014).

[97]M. Khalil, N. Sennett, J. Steinhoff, J. Vines, and A. Buonanno, "Hairy binary black holes in Einstein-Maxwell-dilaton theory and their effective-one-body description", Phys. Rev. D **98**, 104010 (2018).

[98]L. Bernard, "Dynamics of compact binary systems in scalar-tensor theories: equations of motion to the third post-newtonian order", Phys. Rev. D **98**, 044004 (2018).

[99]B. Shiralilou, T. Hinderer, S. M. Nissanke, N. Ortiz, and H. Witek, "Post-Newtonian gravitational and scalar waves in scalar-Gauss–Bonnet gravity", Class. Quant. Grav. **39**, 035002 (2022).

[100]M. Okounkova, L. C. Stein, J. Moxon, M. A. Scheel, and S. A. Teukolsky, "Numerical relativity simulation of gw150914 beyond general relativity", Phys. Rev. D **101**, 104016 (2020).

[101]E. Barausse, C. Palenzuela, M. Ponce, and L. Lehner, "Neutron-star mergers in scalar-tensor theories of gravity", Phys. Rev. D **87**, 081506 (2013).

[102]W. E. East and J. L. Ripley, "Dynamics of spontaneous black hole scalarization and mergers in einstein-scalar-gauss-bonnet gravity", Phys. Rev. Lett. **127**, 101102 (2021).

[103]R. Cayuso and L. Lehner, "Nonlinear, noniterative treatment of eft-motivated gravity", Phys. Rev. D **102**, 084008 (2020).

[104]N. Yunes and F. Pretorius, "Fundamental theoretical bias in gravitational wave astrophysics and the parametrized post-einsteinian framework", Phys. Rev. D **80**, 122003 (2009).

[105]A. Gupta et al., "Possible Causes of False General Relativity Violations in Gravitational Wave Observations", (2024).

[106]O. Lunin and S. D. Mathur, "Ads/cft duality and the black hole information paradox", Nuclear Physics B **623**, 342–394 (2002).

[107]E. Mottola, "Gravitational Vacuum Condensate Stars", 10.1007/978-981-99-1596-5_8 (2023).

[108]S. L. Liebling and C. Palenzuela, "Dynamical boson stars", Living Rev. Rel. **26**, 1 (2023).

[109]G. F. Giudice, M. McCullough, and A. Urbano, "Hunting for Dark Particles with Gravitational Waves", JCAP **10**, 001 (2016).

[110]N. V. Krishnendu and F. Ohme, "Testing General Relativity with Gravitational Waves: An Overview", Universe **7**, 497 (2021).

[111]F.-L. Julié, "Gravitational radiation from compact binary systems in einstein-maxwell-dilaton theories", Journal of Cosmology and Astroparticle Physics **2018**, 033 (2018).

[112]K. Yagi, L. C. Stein, N. Yunes, and T. Tanaka, "Post-newtonian, quasicircular binary inspirals in quadratic modified gravity", Phys. Rev. D **85**, 064022 (2012).

[113]A. Nishizawa, "Generalized framework for testing gravity with gravitational-wave propagation. i. formulation", Phys. Rev. D **97**, 104037 (2018).

[114]M. Okounkova, W. M. Farr, M. Isi, and L. C. Stein, "Constraining gravitational wave amplitude birefringence and Chern-Simons gravity with GWTC-2", Phys. Rev. D **106**, 044067 (2022).

[115]D. Morin, *Waves (draft)* (2023/24).

[116]L. R. Abramo and T. S. Pereira, "Testing gaussianity, homogeneity and isotropy with the cosmic microwave background", Adv. Astron. **2010**, 378203 (2010).

[117]P. Sarkar, J. Yadav, B. Pandey, and S. Bharadwaj, "The scale of homogeneity of the galaxy distribution in SDSS DR6", mnras **399**, L128–L131 (2009).

[118]J.-P. Hu and F.-Y. Wang, "Hubble Tension: The Evidence of New Physics", Universe **9**, 94 (2023).

[119]B. P. Abbott et al., "A gravitational-wave standard siren measurement of the Hubble constant", Nature **551**, 85–88 (2017).

[120]Planck Collaboration, "Planck 2015 results. XIII. Cosmological parameters", aap **594**, A13, A13 (2016).

[121]J. Beltrán Jiménez, J. M. Ezquiaga, and L. Heisenberg, "Probing cosmological fields with gravitational wave oscillations", JCAP **04**, 027 (2020).

[122]J. M. Ezquiaga, W. Hu, M. Lagos, and M.-X. Lin, "Gravitational wave propagation beyond general relativity: waveform distortions and echoes", JCAP **11**, 048 (2021).

[123]J. M. Ezquiaga, W. Hu, M. Lagos, M.-X. Lin, and F. Xu, "Modified gravitational wave propagation with higher modes and its degeneracies with lensing", JCAP **08**, 016 (2022).

[124]S. Droz, D. J. Knapp, E. Poisson, and B. J. Owen, "Gravitational waves from inspiraling compact binaries: Validity of the stationary phase approximation to the Fourier transform", Phys. Rev. D **59**, 124016 (1999).

[125]C. M. Will, "Bounding the mass of the graviton using gravitational wave observations of inspiralling compact binaries", Phys. Rev. D **57**, 2061–2068 (1998).

[126]S. Mirshekari, N. Yunes, and C. M. Will, "Constraining Generic Lorentz Violation and the Speed of the Graviton with Gravitational Waves", Phys. Rev. D **85**, 024041 (2012).

[127]B. P. Abbott et al., "Multi-messenger Observations of a Binary Neutron Star Merger", Astrophys. J. Lett. **848**, L12 (2017).

[128]A. Goldstein et al., "An Ordinary Short Gamma-Ray Burst with Extraordinary Implications: Fermi-GBM Detection of GRB 170817A", Astrophys. J. Lett. **848**, L14 (2017).

[129]V. Savchenko et al., "INTEGRAL Detection of the First Prompt Gamma-Ray Signal Coincident with the Gravitational-wave Event GW170817", Astrophys. J. Lett. **848**, L15 (2017).

[130]B. P. Abbott et al., "Gravitational Waves and Gamma-rays from a Binary Neutron Star Merger: GW170817 and GRB 170817A", Astrophys. J. Lett. **848**, L13 (2017).

[131]B. P. Abbott et al., "Tests of General Relativity with the Binary Black Hole Signals from the LIGO-Virgo Catalog GWTC-1", Phys. Rev. D **100**, 104036 (2019).

[132]R. Abbott et al., "Tests of general relativity with binary black holes from the second LIGO-Virgo gravitational-wave transient catalog", Phys. Rev. D **103**, 122002 (2021).

[133]C. García-Quirós, M. Colleoni, S. Husa, H. Estellés, G. Pratten, A. Ramos-Buades, M. Mateu-Lucena, and R. Jaume, "Multimode frequency-domain model for the gravitational wave signal from nonprecessing black-hole binaries", Phys. Rev. D **102**, 064002 (2020).

[134]OpenAI, "GPT-4 Technical Report", arXiv e-prints, arXiv:2303.08774, arXiv:2303.08774 (2023).

[135]J. Betker, G. Goh, L. Jing, T. Brooks, J. Wang, L. Li, L. Ouyang, J. Zhuang, J. Lee, Y. Guo, et al., "Improving image generation with better captions", Computer Science. **2**, 8 (2023).

[136]L. Sindayigaya and A. Dey, "Machine learning algorithms: a review", Information Systems Journal **11**, 1127–1133 (2022).

[137]C. M. Bishop, *Pattern recognition and machine learning* (Springer Science+Business Media, LLC, 2006).

[138]K. P. Murphy, *Machine learning: a probabilistic perspective* (The MIT Press, 2012).

[139]I. Goodfellow, Y. Bengio, and A. Courville, *Deep learning*, http://www.deeplearningbook.org (MIT Press, 2016).

[140]A. Zhang, Z. C. Lipton, M. Li, and A. J. Smola, "Dive into Deep Learning", arXiv e-prints, arXiv:2106.11342, arXiv:2106.11342 (2021).

[141]P. Baheti, "The essential guide to neural network architectures", https://www.v7labs.com/blog/neural-network-architectures-guide (2022).

[142]P. Baheti, "Activation functions in neural networks [12 types & use cases]", URL https://www. v7labs. com/blog/neural-networks-activation-functions (2022).

[143]Epoch AI, *Parameter, compute and data trends in machine learning*, Accessed: 2024-06-19, 2024.

[144]J. Terven, D. M. Cordova-Esparza, A. Ramirez-Pedraza, and E. A. Chavez-Urbiola, "Loss Functions and Metrics in Deep Learning", arXiv e-prints, arXiv:2307.02694, arXiv:2307.02694 (2023).

[145]A. Amini, A. Soleimany, S. Karaman, and D. Rus, "Spatial Uncertainty Sampling for End-to-End Control", arXiv e-prints, arXiv:1805.04829, arXiv:1805.04829 (2018).

[146]D. P. Kingma and J. Ba, "Adam: A Method for Stochastic Optimization", arXiv e-prints, arXiv:1412.6980, arXiv:1412.6980 (2014).

[147]I. K. Fodor, *A survey of dimension reduction techniques*, tech. rep. (Lawrence Livermore National Lab.(LLNL), Livermore, CA (United States), 2002).

[148]M. H. ur Rehman, C. S. Liew, A. Abbas, P. P. Jayaraman, T. Y. Wah, and S. U. Khan, "Big data reduction methods: a survey", Data Science and Engineering **1**, 265–284 (2016).

[149]N. Halko, P.-G. Martinsson, and J. A. Tropp, "Finding structure with randomness: Probabilistic algorithms for constructing approximate matrix decompositions", arXiv e-prints, arXiv:0909.4061, arXiv:0909.4061 (2009).

[150]B. Bermeitinger, T. Hrycej, and S. Handschuh, "Singular Value Decomposition and Neural Networks", arXiv e-prints, arXiv:1906.11755, arXiv:1906.11755 (2019).

[151]C. Eckart and G. Young, "The approximation of one matrix by another of lower rank", Psychometrika **1**, 211–218 (1936).

[152]K. Cannon, A. Chapman, C. Hanna, D. Keppel, A. C. Searle, and A. J. Weinstein, "Singular value decomposition applied to compact binary coalescence gravitational-wave signals", Phys. Rev. D **82**, 044025 (2010).

[153]K. He, X. Zhang, S. Ren, and J. Sun, "Deep Residual Learning for Image Recognition", arXiv e-prints, arXiv:1512.03385, arXiv:1512.03385 (2015).

[154]R. K. Srivastava, K. Greff, and J. Schmidhuber, "Highway Networks", arXiv e-prints, arXiv:1505.00387, arXiv:1505.00387 (2015).

[155]K. He, X. Zhang, S. Ren, and J. Sun, "Identity Mappings in Deep Residual Networks", arXiv e-prints, arXiv:1603.05027, arXiv:1603.05027 (2016).

[156]J.-M. Lueckmann, J. Boelts, D. S. Greenberg, P. J. Gonçalves, and J. H. Macke, "Benchmarking Simulation-Based Inference", arXiv e-prints, arXiv:2101.04653, arXiv:2101.04653 (2021).

[157]I. M. George Papamakarios, *Fast ϵ-free inference of simulation models with bayesian conditional density estimation*, Apr. 2018.

[158]M. Dax, S. R. Green, J. Gair, J. H. Macke, A. Buonanno, and B. Scholkopf, *Real-time gravitational-wave science with neural posterior estimation*, June 2021.

[159]M. Dax, S. R. Green, J. Gair, M. Deistler, B. Schölkopf, and J. H. Macke, ""group equivariant posterior estimation"", The Tenth International Conference on Learning Representations (2022).

[160]M Andrés-Carcasona, M Martínez, and L. M. Mir, "Fast Bayesian gravitational wave parameter estimation using convolutional neural networks", Monthly Notices of the Royal Astronomical Society **527**, 2887–2894 (2023).

[161]H. Gabbard, C. Messenger, I. S. Heng, F. Tonolini, and R. Murray-Smith, "Bayesian parameter estimation using conditional variational autoencoders for gravitational-wave astronomy", Nature Phys. **18**, 112–117 (2022).

[162]I. Kobyzev, S. J. Prince, and M. A. Brubaker, "Normalizing flows: an introduction and review of current methods", IEEE Transactions on Pattern Analysis and Machine Intelligence **43**, 3964–3979 (2021).

[163]J. Langendorff, A. Kolmus, J. Janquart, and C. Van Den Broeck, "Normalizing flows as an avenue to studying overlapping gravitational wave signals", Phys. Rev. Lett. **130**, 171402 (2023).

[164]F. De Santi, M. Razzano, F. Fidecaro, L. Muccillo, L. Papalini, and B. Patricelli, "Deep learning to detect gravitational waves from binary close encounters: Fast parameter estimation using normalizing flows", Phys. Rev. D **109**, 102004 (2024).

[165]M. Dax, S. R. Green, J. Gair, M. Pürrer, J. Wildberger, J. H. Macke, A. Buonanno, and B. Schölkopf, "Neural importance sampling for rapid and reliable gravitational-wave inference", Phys. Rev. Lett. **130**, 171403 (2023).

[166]A. Kolmus, J. Janquart, T. Baka, T. van Laarhoven, C. Van Den Broeck, and T. Heskes, "Tuning neural posterior estimation for gravitational wave inference", (2024).

[167]S. Ramasinghe, K. Fernando, S. Khan, and N. Barnes, "Robust normalizing flows using Bernstein-type polynomials", arXiv e-prints, arXiv:2102.03509, arXiv:2102.03509 (2021).

[168]M. Arpogaus, M. Voš, B. Sick, M. Nigge-Uricher, and O. Dürr, "Probabilistic short-term low-voltage load forecasting using bernstein-polynomial normalizing flows", in Icml 2021, workshop tackling climate change with machine learning, june 26, 2021, virtual (2021).

[169]R. Farouki and V. Rajan, "On the numerical condition of polynomials in bernstein form", Computer Aided Geometric Design **4**, 191–216 (1987).

[170]J. M. Peña, "B-splines and optimal stability", Mathematics of Computation **66**, 1555–1560 (1997).

[171]R. T. Farouki and T. N. T. Goodman, "On the optimal stability of the bernstein basis", Mathematics of Computation **65**, 1553–1566 (1996).

[172]M. R. Spencer, *Polynomial real root finding in bernstein form* (Brigham Young University, 1994).

[173]L. Dinh, J. Sohl-Dickstein, and S. Bengio, "Density estimation using Real NVP", arXiv e-prints, arXiv:1605.08803, arXiv:1605.08803 (2016).

[174]C. Winkler, D. E. Worrall, E. Hoogeboom, and M. Welling, "Learning likelihoods with conditional normalizing flows", CoRR **abs/1912.00042** (2019).

[175]R. J. Rossi, *Mathematical statistics: an introduction to likelihood based inference* (John Wiley & Sons, New York, 2018), p. 227.

[176]J. Bradbury, R. Frostig, P. Hawkins, M. J. Johnson, C. Leary, D. Maclaurin, G. Necula, A. Paszke, J. VanderPlas, S. Wanderman-Milne, and Q. Zhang, *JAX: composable transformations of Python+NumPy programs*, version 0.3.13, 2018.

[177]C. Durkan, A. Bekasov, I. Murray, and G. Papamakarios, "Neural Spline Flows", arXiv e-prints, arXiv:1906.04032, arXiv:1906.04032 (2019).

[178]T. D. P. Edwards, K. W. K. Wong, K. K. H. Lam, A. Coogan, D. Foreman-Mackey, M. Isi, and A. Zimmerman, "ripple: Differentiable and Hardware-Accelerated Waveforms for Gravitational Wave Data Analysis", (2023).

[179]G. Ashton, M. Hübner, P. D. Lasky, C. Talbot, K. Ackley, S. Biscoveanu, Q. Chu, A. Divakarla, P. J. Easter, B. Goncharov, F. H. Vivanco, J. Harms, M. E. Lower, G. D. Meadors, D. Melchor, E. Payne, M. D. Pitkin, J. Powell, N. Sarin, R. J. E. Smith, and E. Thrane, "Bilby: a user-friendly bayesian inference library for gravitational-wave astronomy", The Astrophysical Journal Supplement Series **241**, 27 (2019).

[180]B. P. Abbott et al., "Prospects for observing and localizing gravitational-wave transients with Advanced LIGO, Advanced Virgo and KAGRA", Living Rev. Rel. **19**, 1 (2016).

[181]*Ligo-t2000012-v2: noise curves used for simulations in the update of the observing scenarios paper*.

[182]P. Kidger and C. Garcia, "Equinox: neural networks in JAX via callable PyTrees and filtered transformations", arXiv e-prints, arXiv:2111.00254, arXiv:2111.00254 (2021).

[183]D. Ward, *Flowjax: distributions and normalizing flows in jax*, version [v12.2.0], [2024].

[184]J. Lei Ba, J. R. Kiros, and G. E. Hinton, "Layer Normalization", arXiv e-prints, arXiv:1607.06450, arXiv:1607.06450 (2016).

[185]DeepMind, *The DeepMind JAX Ecosystem*, 2020.

[186]S. J. Miller, Z. Ko, T. Callister, and K. Chatziioannou, "Gravitational waves carry information beyond effective spin parameters but it is hard to extract", Phys. Rev. D **109**, 104036 (2024).

[187]F. J. Massey, "The kolmogorov-smirnov test for goodness of fit", Journal of the American Statistical Association **46**, 68–78 (1951).

[188]R. Smith, S. E. Field, K. Blackburn, C.-J. Haster, M. Pürrer, V. Raymond, and P. Schmidt, "Fast and accurate inference on gravitational waves from precessing compact binaries", Phys. Rev. D **94**, 044031 (2016).

[189]J. Lange, R. O'Shaughnessy, and M. Rizzo, "Rapid and accurate parameter inference for coalescing, precessing compact binaries", (2018).

[190]R. J. E. Smith, G. Ashton, A. Vajpeyi, and C. Talbot, "Massively parallel Bayesian inference for transient gravitational-wave astronomy", Monthly Notices of the Royal Astronomical Society **498**, 4492–4502 (2020).

[191] L. Sharrock, J. Simons, S. Liu, and M. Beaumont, "Sequential Neural Score Estimation: Likelihood-Free Inference with Conditional Score Based Diffusion Models", arXiv e-prints, arXiv:2210.04872, arXiv:2210.04872 (2022).

[192] M. A. T. Chowdhury, "Advancements in Glitch Subtraction Systems for Enhancing Gravitational Wave Data Analysis: A Brief Review", (2024).

[193] P. Laguarta et al., "Detection of anomalies amongst LIGO's glitch populations with autoencoders", Class. Quant. Grav. **41**, 055004 (2024).

[194] T. Dooney, L. Curier, D. Tan, M. Lopez, C. Van Den Broeck, and S. Bromuri, "cDVGAN: One Flexible Model for Multi-class Gravitational Wave Signal and Glitch Generation", (2024).

[195] B. Sathyaprakash et al., "Scientific Objectives of Einstein Telescope", Class. Quant. Grav. **29**, edited by M. Hannam, P. Sutton, S. Hild, and C. van den Broeck, [Erratum: Class.Quant.Grav. 30, 079501 (2013)], 124013 (2012).

Appendix A

Additional figures

An illustration of the used beta distribution for SNR scaling is given in figure A.1.

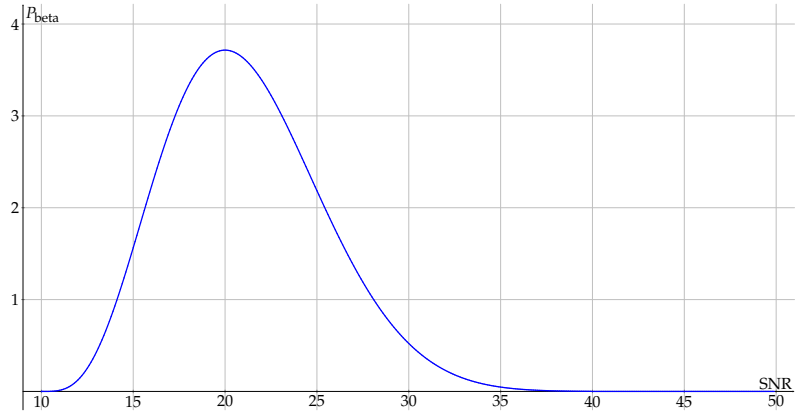

FIGURE A.1: Beta distribution with $T_{\text{SNR}} = 15$, $P_{\text{SNR}} = 20$, $\text{Min}_{\text{SNR}} = 10$, and $\text{Min}_{\text{SNR}} = 50$.

The SVD of a dataset of 10000 GW signals with the MDR correction of $\alpha = 0$ is represented in A.2. From this is inverted that the SVD basis of 700 kernels is sufficient to represent data **d** well. Note that the SVD is done in frequency space and thus here the absolute value of the eigenvalues is plotted.

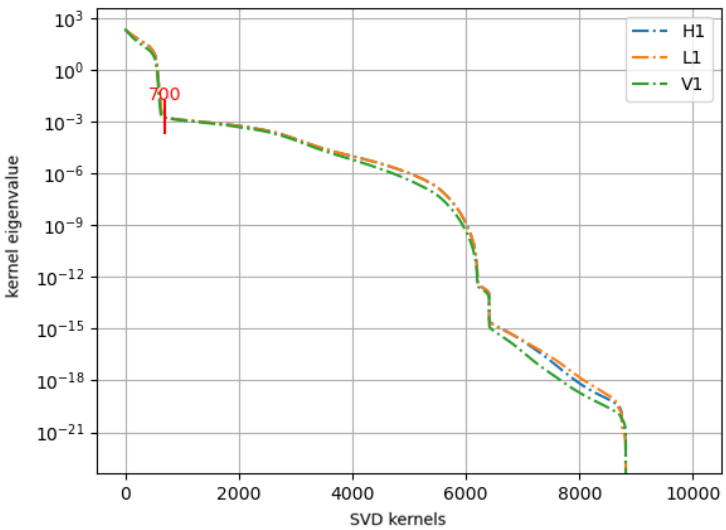

FIGURE A.2: SVD kernels and eigenvalues on $\alpha = 0$ signals for the three different detectors.

Appendix B

Additional Results

Here we present example corner plots as described in section 8.1. Figures B.1 to B.9 are corner plots obtained with increasing values of α. Due to the size of the plots, they start on the next page.

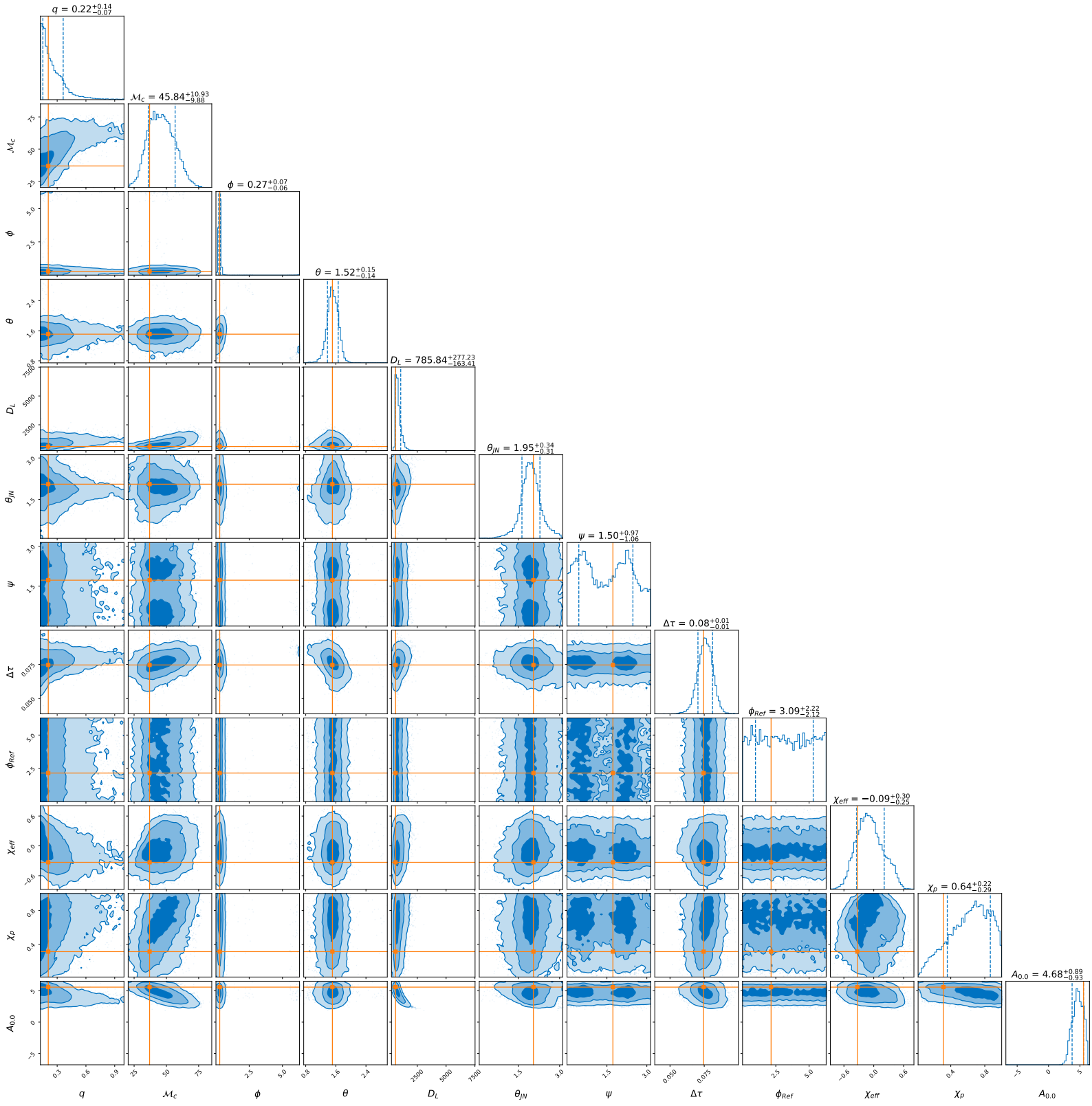

FIGURE B.1: Corner plot for phenomenological parameter $\alpha = 0$. With $A_\alpha$in$[10^{-19}$ peV$^{\alpha-2}]$.

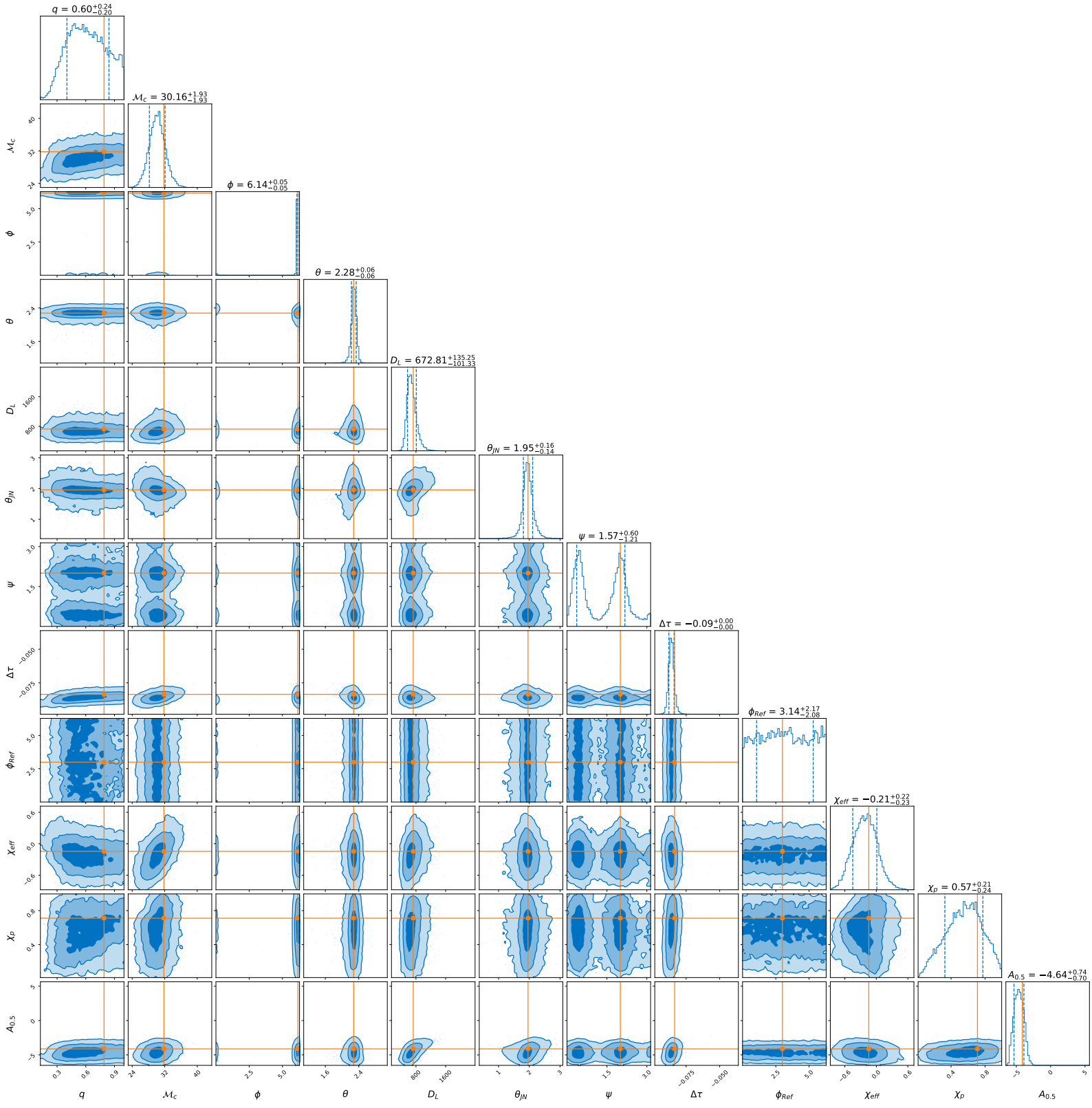

FIGURE B.2: Corner plot for phenomenological parameter $\alpha = \frac{1}{2}$.
With $A_\alpha \text{in}[10^{-19}\ \text{peV}^{\alpha-2}]$.

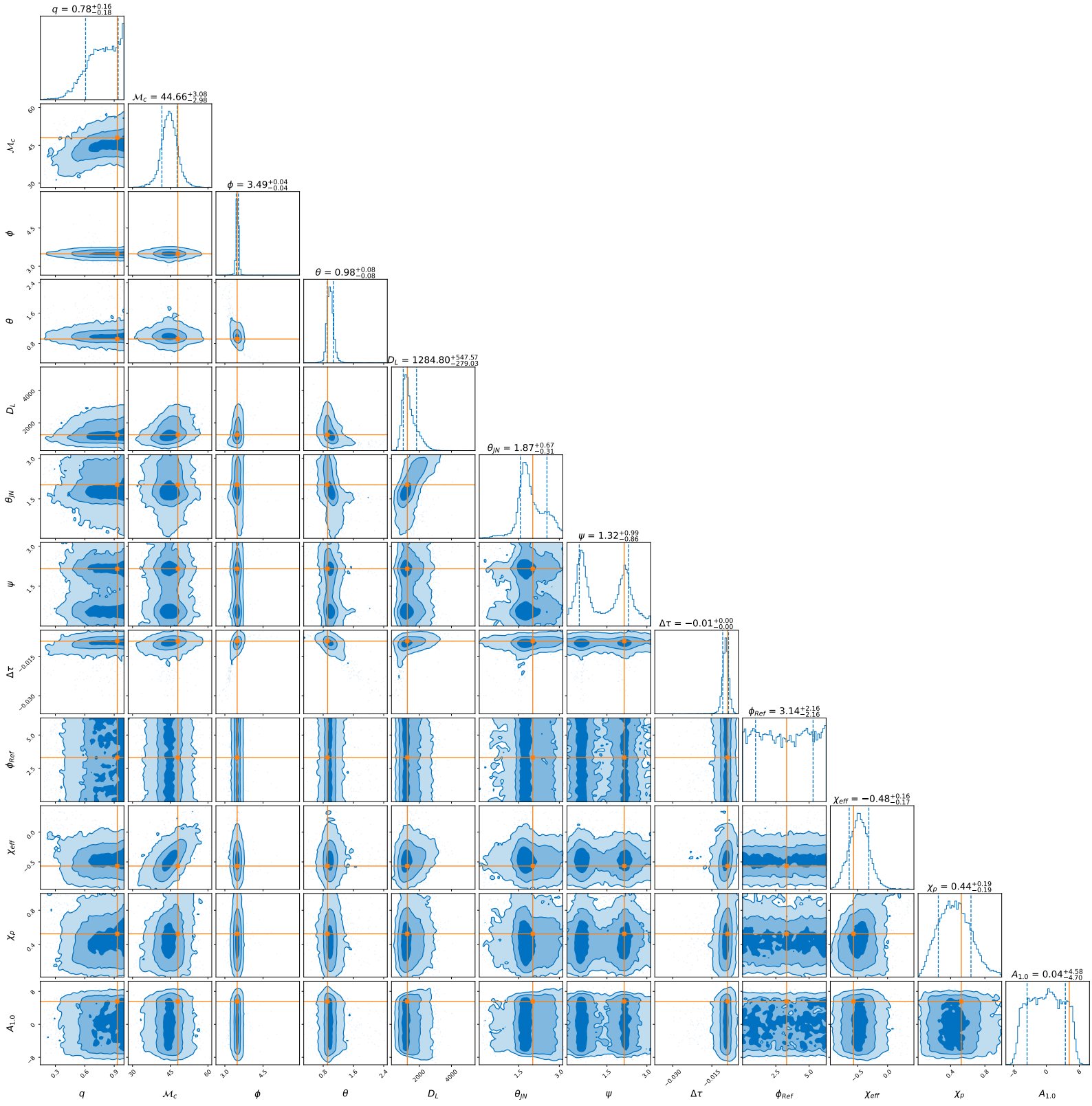

FIGURE B.3: Corner plot for phenomenological parameter $\alpha = 1$.
With $A_\alpha$in$[10^{-19}$ peV$^{\alpha-2}]$.

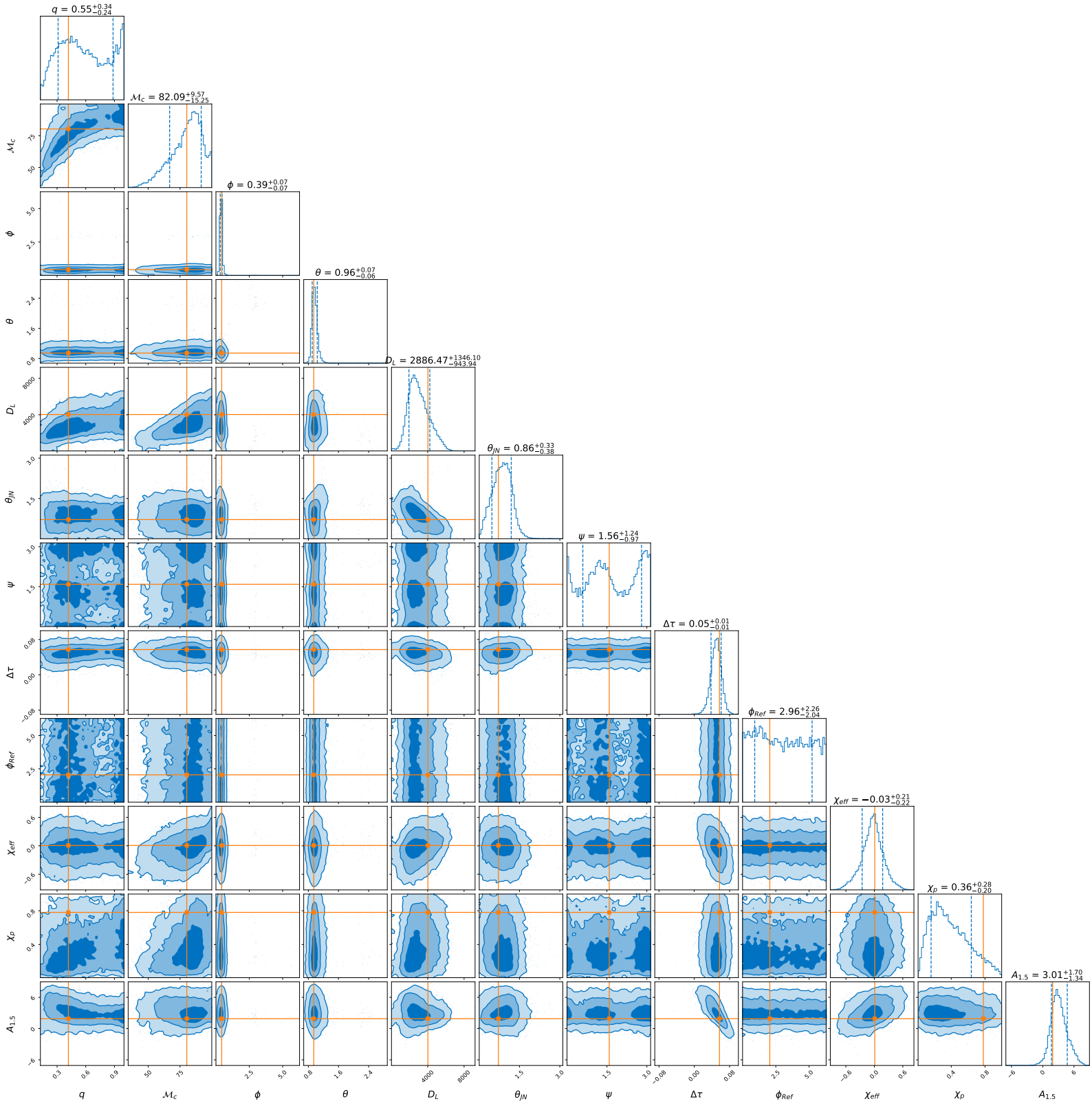

FIGURE B.4: Corner plot for phenomenological parameter $\alpha = \frac{3}{2}$.
With A_α in $[10^{-19}\ \mathrm{peV}^{\alpha-2}]$.

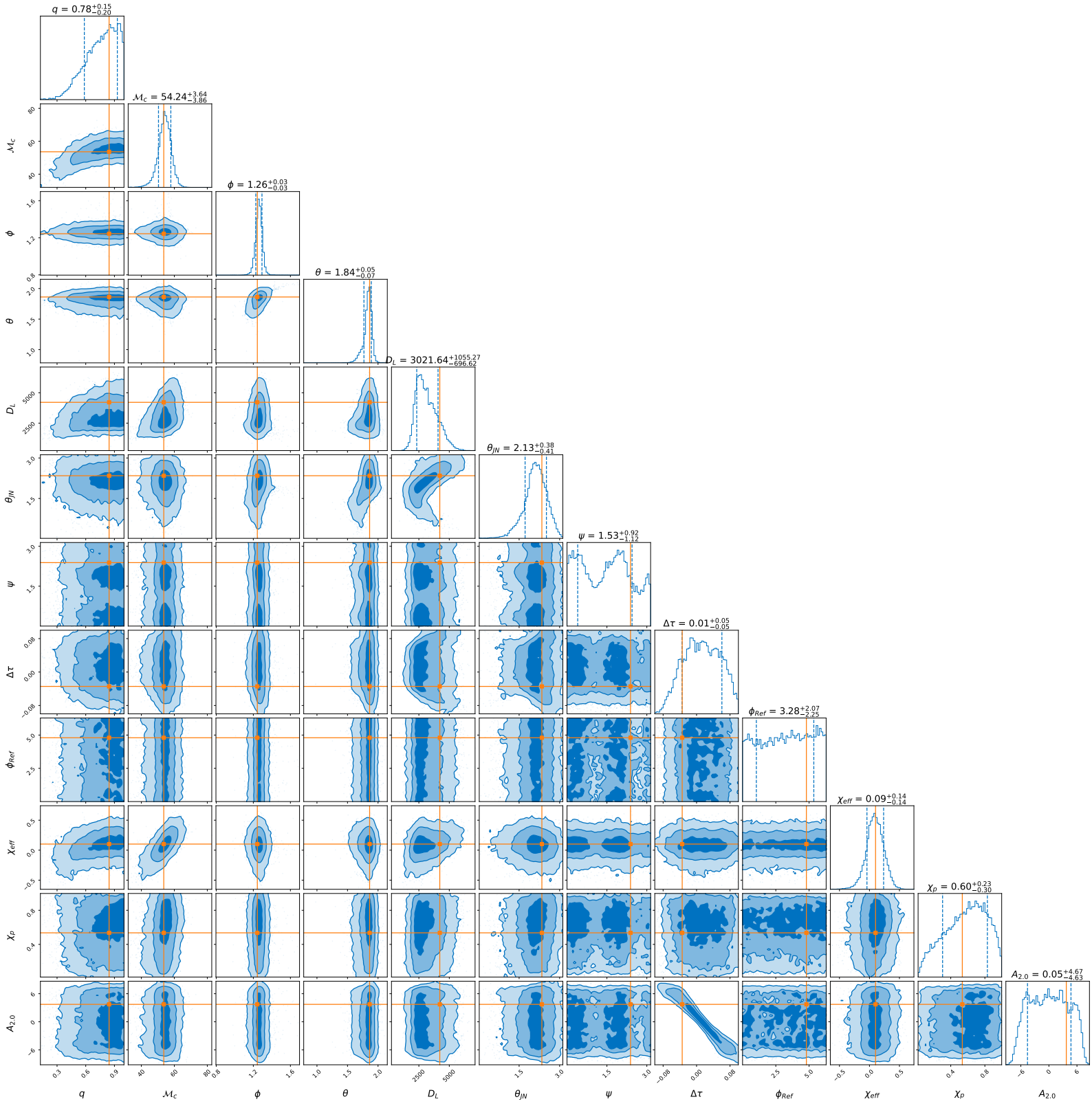

FIGURE B.5: Corner plot for phenomenological parameter $\alpha = 2$.
With $A_\alpha$in$[10^{-19}$ peV$^{\alpha-2}]$.

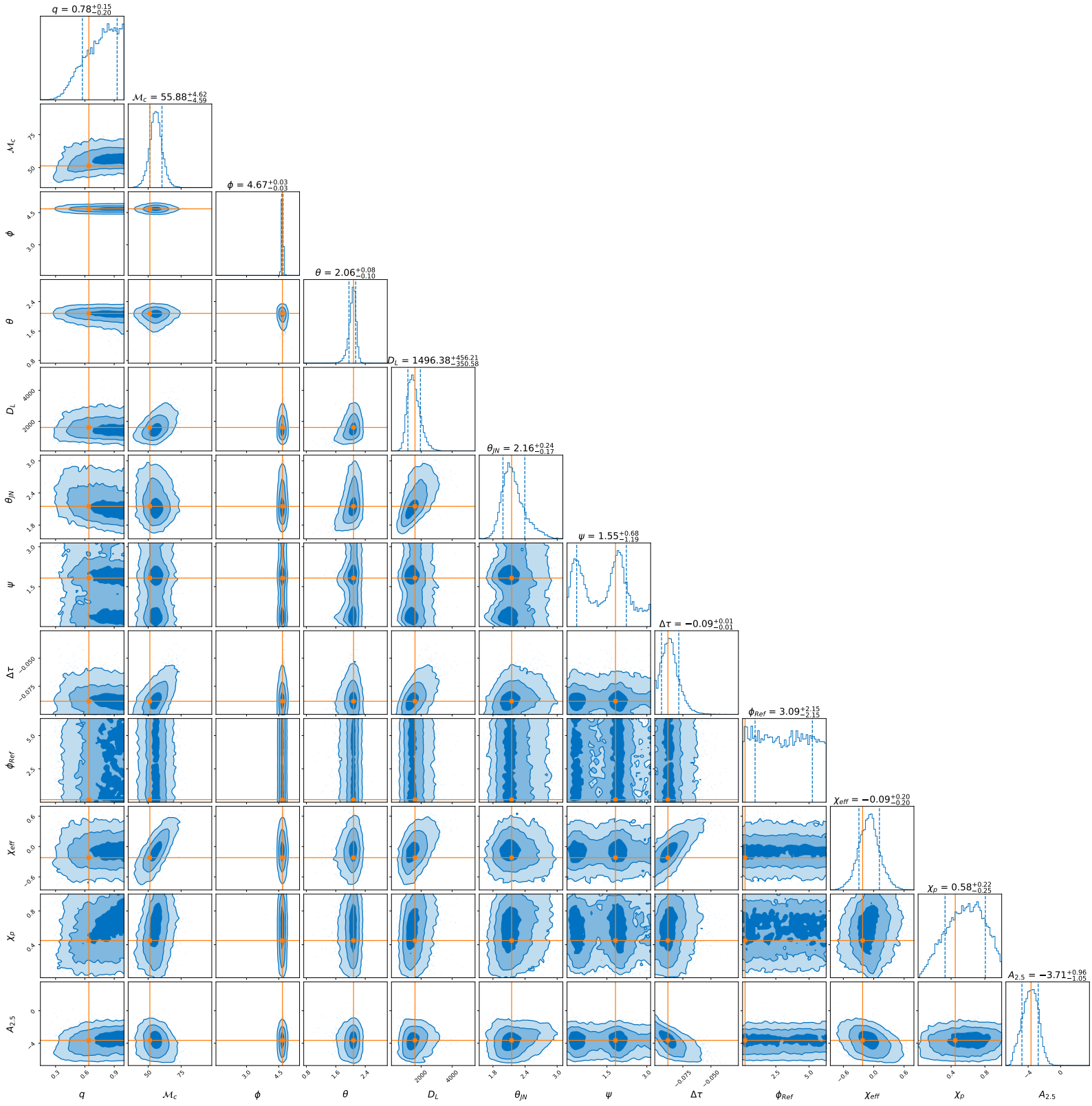

FIGURE B.6: Corner plot for phenomenological parameter $\alpha = \frac{5}{2}$.
With $A_\alpha \text{in}[10^{-19}\ \text{peV}^{\alpha-2}]$.

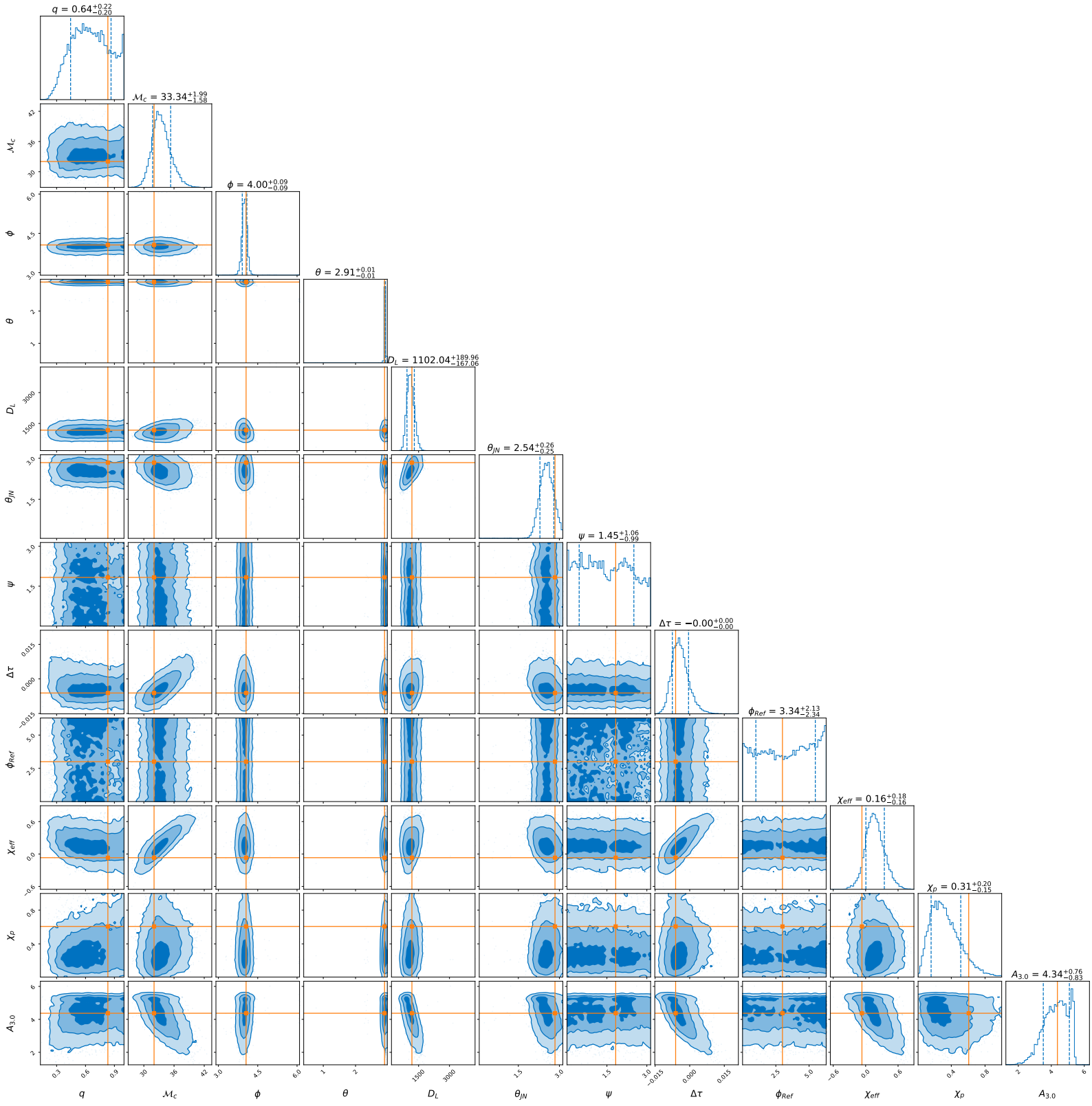

FIGURE B.7: Corner plot for phenomenological parameter $\alpha = 3$. With $A_\alpha$in$[10^{-19}$ peV$^{\alpha-2}]$.

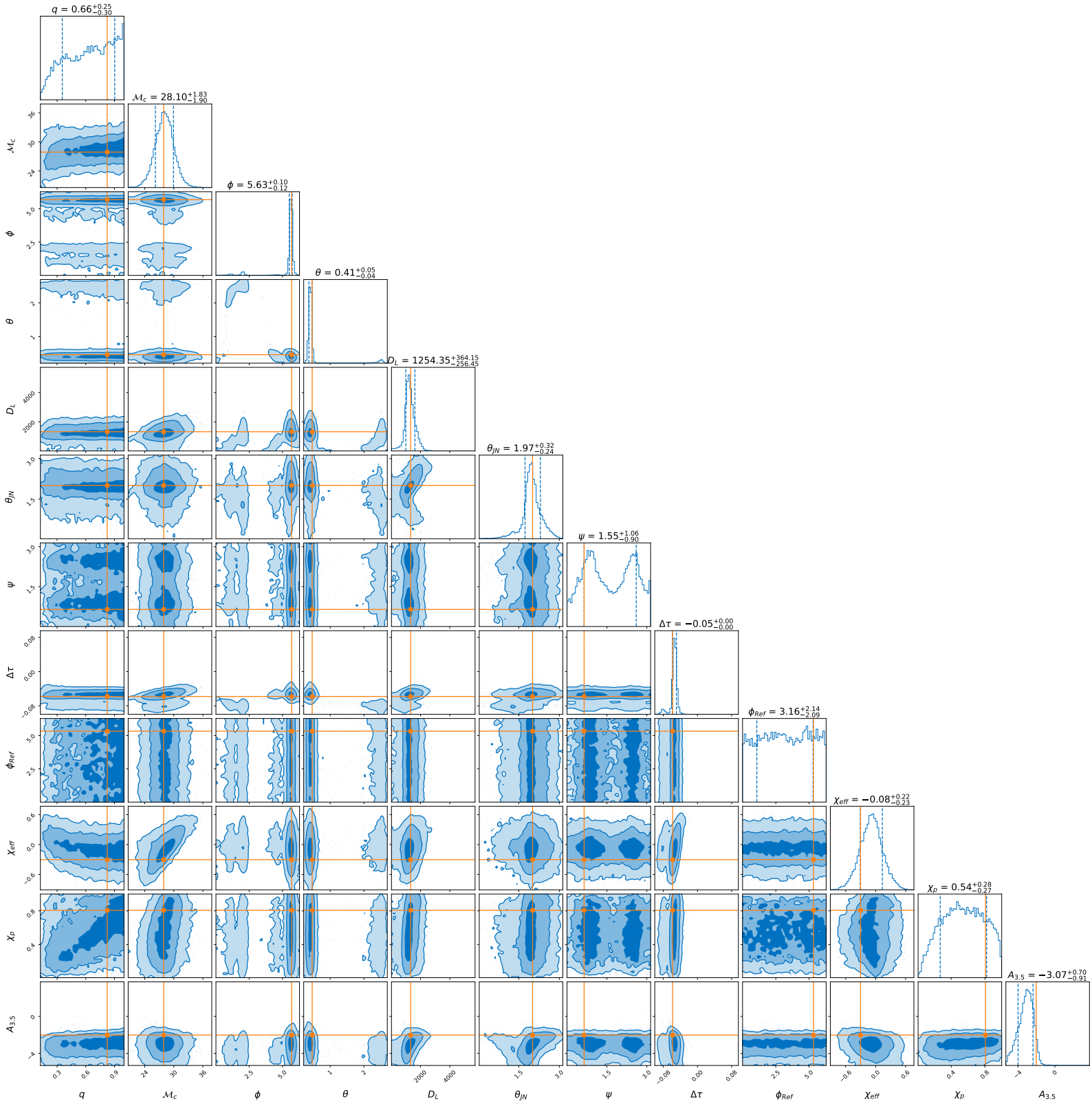

FIGURE B.8: Corner plot for phenomenological parameter $\alpha = \frac{7}{2}$.
With $A_\alpha \text{in}[10^{-19}\ \text{peV}^{\alpha-2}]$.

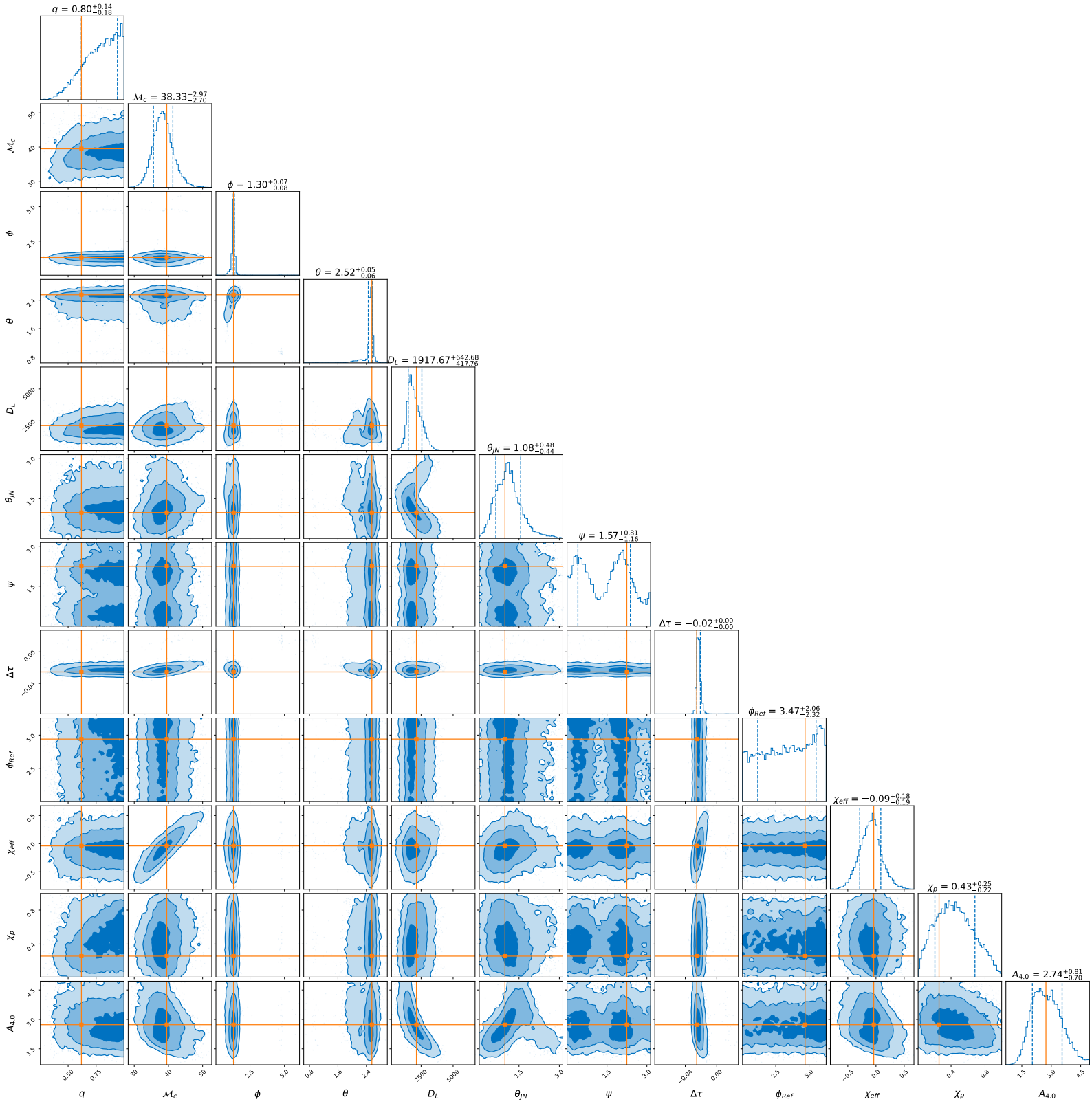

FIGURE B.9: Corner plot for phenomenological parameter $\alpha = 4$. With $A_\alpha$in$[10^{-19}$ peV$^{\alpha-2}]$.